Optical resonances in TiO_2 Mie scatterers on SiN and a-Si thin films for solar cells

Georgios Giannakoudakis

Supervisor:
Dr. Marcel Di Vece

Research project for the master's degree in

Nanomaterials: Chemistry and Physics

Soft Condensed Matter, Nanophotonics—Physics of Devices

Debye Institute for Nanomaterials Science

Utrecht University

the Netherlands

Abstract

Thin film solar cells are an efficient alternative to conventional thick, SI wafer based, solar cells. The small thickness however leads to substantially lower light absorption. Ongoing research for efficiency optimization investigates concepts such as plasmonics and elongated structures. A novel approach involves the use of nanoparticles that can efficiently couple light into the solar cell via Mie scattering. A Mie scatterer, usually a high refractive index material, favors forward scattering of light i.e. in the direction of propagation by causing light to resonate inside it. Light is then redirected to the layers below in a way that its optical path length can be increased and therefore have a higher probability of being absorbed. Such a process can facilitate the effective and wavelength selective harvesting of photons with energies close to the band gap of the solar cell. Current research involving nanoparticles acting as Mie scatterers for light trapping in solar cells is based on nanolithography techniques. These processes are very cost inefficient therefore it is necessary to seek alternative fabrication methods. In this thesis we present the fabrication of a light trapping layer consisting of TiO_2 Mie scatterers deposited on amorphous Silicon and Silicon Nitride thin films. The TiO_2 nanoparticles are fabricated using a gas-phase aggregation nanocluster source. The nanoparticles are cubic in shape and are able to support Mie resonances that can couple light into the solar cell. The nanoparticles range in size from less than 10 nm to greater than 160 nm, of which the latter is comparable to the wavelength. Optical measurements of refection and transmission show peaks and valleys in the wavelength range between 350 nm and 900 nm creating asymmetrical line shapes, which strongly correspond to the so called Fano-type resonance, which is caused by the interference of a continuous back ground and single transition. Therefore, this work opens a new highly promising research path that will involve the use of nanocluster sources for increased efficiency of thin film solar cells.

Acknowledgements

First and foremost, I would like to thank Marcel Di Vece for supervising this work. Thank you for your trust and faith in me, for guiding me through this research and for inspiring me. Thank you for your encouragement, feedback patience, understanding and flexibility.

I would also like to thank Dr. Marijn Van Huis to be my first examiner.

I would like to thank Klaas Bakker for his assistance and guidance during the UV-Vis measurements in Eindhoven. Joost Van der Lit for instructing and helping with the AFM microscope. Thomas van der Vliet for instructing me through FDTD simulations as well as additional help and support. Wingjohn Tang for collaborating during the early stages of the thesis as well as providing SEM images for some of my samples. I would also like to thank Da Wang for providing the nice TEM images of the nanoparticles.

Contents

Chapter 1

Introduction

Throughout the ages, human civilization has carried out numerous achievements, driven by both the desire of new knowledge and the need of technological development. By the mid-19th century, industrial revolution and technological breakthrough on early 20th century, drove global energy demand to rise and since then it is constantly increasing over the years. Global energy consumption has increased by more than 50% from 1971 to 2015[1]. The 2013 estimate for world energy usage was 18 TW[2] and an increase of 45% is expected by 2035. Fossil fuels are the current dominant energy resources, with heavy emissions of CO_2 being the major drawback of their use. The annual release of CO_2 only from the power industry was 10.9 Giga tons of carbon dioxide equivalent for 2005. Future predictions show a further increase, reaching up to 18.7 $GtCO_2e$ in 2030[3]. This makes fossil fuel a completely non-viable solution to our energy demands, therefore a turn to renewable, clean energy producing methods is crucial. The amount of power that earth receives by solar radiation is $1.4 \times 10^5\ TW$[4] from which $3.6 \times 10^4\ TW$ can be effectively used. Only a fraction of this tremendous quantity of power is enough to cover modern world's energy demand.

In order to convert solar radiation into useful electrical power, we need photovoltaic (PV) devices. A PV solar cell generates power through the "photovoltaic effect". There are two main types of commercial PV technologies. Wafer based crystalline Si (c-Si), and thin-film solar cells. The global market

is currently dominated by the c-Si solar cell, with efficiencies reaching 22%[5]. The energy consumption of the manufacturing process of c-Si wafers however, further increases the cost of the module. Monocrystalline Si is produced via the Czochralski process which silicon is molten through electrical heating in order for the monocrystal to be formed[6] . The high temperatures reached during the process makes it very energy demanding and therefore expensive. This greatly limits the possibilities of widespread use of PV technology.

Thin-film solar cells, are made by bottom-up deposition of thin layer of semiconductor material, ranging in thickness from few 100 nm to several μm. Current types of thin film technologies include copper indium gallium diselenide (CIGS), cadmium telluride (CdTe) and amorpous Si (a-Si). The small thickness of the film is a major advantage since far less material is used for its manufacture, which makes thin-film solar cells a very promising solution to greatly reduce the production costs. However, the small thickness poses a limit to the amount of light that is absorbed, leading to very low conversion efficiencies. This results from the fact that the absorption depth and the minority carrier diffusion length are very incompatible, especially near the bandgap[7]. In order to increase light absorption, we need to manipulate the incident light in such a way that it is redirected in the active layer and therefore its path through the layer is increased, a technique known as light trapping. The concept was first realized for conventional thick cells, where total internal reflection is utilized. The simplest form of light trapping is by applying a random texture on a substrate, on top of which the solar cell is assembled, giving it the ability to redirect light in the semiconductor material[8]. These features can be created by an inexpensive procedure such as etching[9]. In such designs the absorption enhancement limit is governed by the factor $4n^2$[10] , for a solar cell with an isotropic angular emission, where n is the refractive index of the semiconductor material. However, the conventional ray optics approach fails to apply when nanoscale photonic structures are introduced therefore a wave optics approach must be followed. As shown by Yu et al.[10] this limit can be greatly surpassed when appropriate designs are realized.

In order to achieve light trapping in thin film solar cells, nanostructures must be implemented to scatter incident light and redirect it in the absorbing region of the cell and therefore enhance absorption by increasing the path length of the optical wave. An important property of the solar cell is the ability to support a number of different optical modes[7]. When nanostructures are placed on top of the solar cell they can act as scatterers and when placed at the bottom they function as back-scatterers. Various design strategies have been developed for that reason such as making use of metallic nanoparticles to exploit plasmon resonances[11]. However parasitic absorption, by Ohmic resistance in the metal, poses a constraint

to the performance of the cell[12] . Alternatively, high-refractive index dielectric and semiconductor nanostructures can be used since they do not suffer from parasitic absorption losses[6]. A previous study using numerical simulations for light trapping using high index nanospheres, suggested an increase in efficiency of up to 50%0[13] . In figure 1 a schematic diagram of a light trapping scheme is shown[7]. The dielectric nanostructures are placed on top of a 1 μm thick c-Si film and a perfect back mirror placed below the film. Four of the most common optical modes are shown. When these modes are excited light absorption is enhanced, increasing the optical thickness of the film.

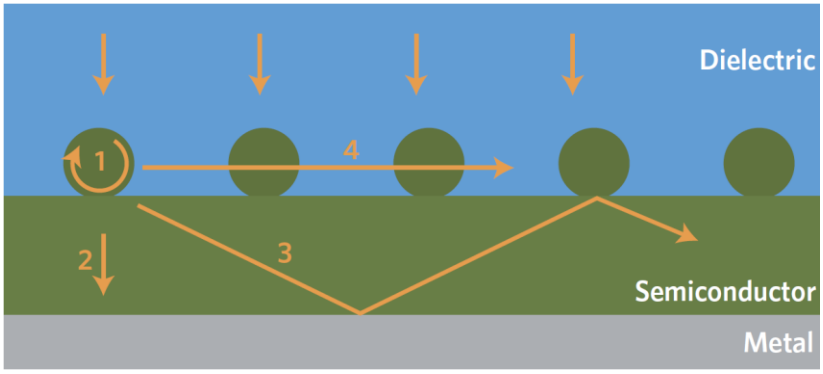

Figure 1: Schematic illustration depicting the different ways an optical resonance supported by a prototype solar cell can be excited to achieve absorption enhancement of light in the semiconductor regionΣφάλμα! Δεν έχει οριστεί σελιδοδείκτης.**. The coupling mechanisms are noted by numbers 1-4.[7]**

Sunlight can be resonantly coupled to distinct modes that are supported by a solar cell, giving them the term resonances. The field distribution depends on the type of resonance which in turn shows distinct angular dependency of the resonance wavelength. Figure 2 a-d shows the electric field intensity distribution for four different illumination types shown in figure 1.

Figure 2a is of particular interest since a clear Mie resonance can be observed inside the Si nanostructure (outlined by the dashed line). Mie scattering of light by a nanoparticle is the main focus of this thesis.

Nanoparticles comparable to the size of the wavelength can function as Mie scatterers. The Mie theory was formulated by Gustav Mie in 1908 while trying to understand the variation of colors in absorption and scattering demonstrated by colloidal nanoparticles of gold. Mie provided a solution to Maxwell's equations in the form of infinite series of spherical waves. A particle that measures a tenth of the wavelength in size or greater, can support a number of resonances which lead to strong forward scattering, i.e. in the direction of incident light. Nanostructures such as Si nanopillars[14], nanocylinders[15] and other geometries arranged in periodic arrays have been reported to support Mie resonances and

effectively enhance the coupling of light into a solar cell. Nanopatterned AZO Mie scatterers embedded between the semiconductor and the back contact proved to be able to trap light at the red-infrared region of spectrum[16].

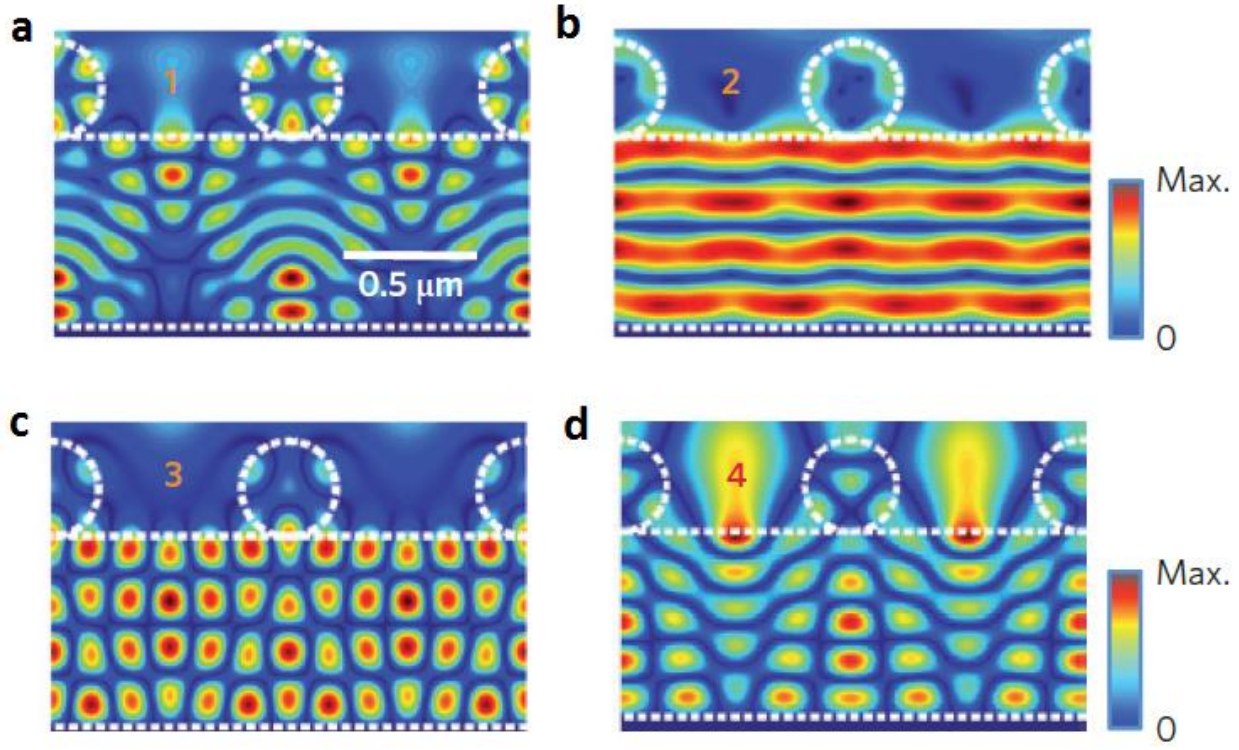

Figure 2: a) Excitation of a combination of Mie resonance with a guided resonance at λ = 880 nm, normal incidence. b) Fabry-Perot resonance at 28⁰ angle of incidence, λ=1031 nm. c) Excitation of a guided resonance at λ = 946 nm, normal incidence. d) Diffracted resonance at normal incidence with λ=1011 nm. [7]

Silica nanoparticles ranging in size from 25 nm to 100 nm have shown enhanced absorption in organic solar cells[17] owing to strong forward Mie scattering. Simulations of Si nanocylinders on μm thick c-Si cell predicted peaks in absorption at 910, 960 and 1100 nm[18]. Further research[19-22] indicates the importance of nanostructures able to act as Mie scatterers. Titanium dioxide (TiO_2) nanoparticles have been reportedly use as scatterers[23-25] for the fabrication of both light trapping layers and anti-reflection coatings. Known as white pigment, titanium dioxide, in its bulk form, has been used for numerous applications which led to its exploitation in the nanoscale[26]. In our approach, TiO_2 Mie scatterers were fabricated by using a gas phase aggregation nanocluster source. In contrast to the very expensive nanolithography manufacturing methods used in most of the current research, the usage of a cluster

source provides an alternative, economically more viable solution. The nanoparticles were deposited on amorphous Si (a-Si) and silicon nitride (SiN) thin-films of various thicknesses, which are also comparable to the wavelength. The strategy behind the concept is to take advantage of the strong forward scattering of the TiO_2 nanoparticles and further redirect light into the thin film. Once inside the film, light may undergo multiple internal reflections making the film act as a Fabry-Perot interferometer, where two counter propagating waves interfere, creating standing wave resonances that enhance optical transmission. The particles range in size from 10 nm to >160nm. Optical measurements of reflection and transmission showed clear prominent peaks which were accompanied by less intense dips. This feature was present in the closely agreeing finite difference time domain (FDTD) simulations that were performed. The asymmetric line shape is a result of two scattering processes that interfere, constructively and destructively creating a Fano resonance.

Chapter 2

Theory

2.1: Mie scattering

The goal of this project makes use of the scattering of light by small particles. The small particles here considered have a dimension which is smaller than or comparable to the wavelength of the incident electromagnetic wave. The TiO_2 nanoclusters used in the experiments measure in general $\frac{1}{10}\lambda$ in height or greater. Light scattering by this type of scattering is described by Mie theory. Gustav Mie solved Maxwell's equations to derive the incident, scattered and internal electromagnetic fields of a plane wave incident on a homogeneous sphere. The complete and detailed derivation of the solutions is beyond the scope of this thesis. Instead a summary of the important points of the derivation will be given as a way to understand the resulting equations, followed by a discussion. The notation used is taken by Bohren and Huffman[27].

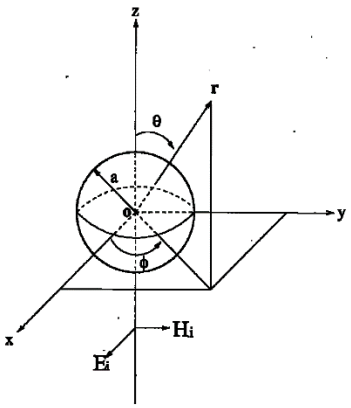

Figure 1: Schematic diagram of the small spherical particle of radius α on which a polarized electromagnetic plane wave is incident. The coordinate system originates at the center of the particle. The plane wave propagates in the positive z direction and is polarized in the direction of x axis. The polar angles θ and ϕ define the direction of the scattered light.[36]

A spherical particle of radius α, embedded in a non-absorbing medium is considered. A linearly polarized plane wave incident on the particle undergoes scattering. A schematic diagram is shown in Fig. 1. Spherical coordinates need to be implemented since we are considering a sphere.

The first step is to express the scalar wave equation in spherical coordinates:

$$\frac{1}{r^2}\frac{\partial}{\partial r}\left(r^2\frac{\partial\psi}{\partial r}\right)+\frac{1}{r^2 sin\theta}\frac{\partial}{\partial\theta}\left(sin\theta\frac{\partial\psi}{\partial\theta}\right)+\frac{1}{r^2 sin\theta}\frac{\partial^2\psi}{\partial\phi^2}+k\psi^2=0 \quad (2.1)$$

To which we seek particular solutions of the form:

$$\psi(r,\theta,\phi)=R(r)\Theta(\theta)\Phi(\phi)$$

By substitution to (2.1) and separation of variable we get three equations:

$$\frac{d^2\Phi}{d\phi^2}+m^2\Phi=0 \quad (2.2)$$

$$\frac{1}{sin\theta}\frac{d}{d\theta}\left(sin\theta\frac{d\Theta}{\mathrm{d}\theta}\right)+\left[n(n+1)-\frac{m^2}{\sin^2\theta}\right]\Theta=0 \quad (2.3)$$

$$\frac{d}{dr}\left(r^2\frac{dR}{dr}\right)+[k^2r^2-n(n+1)]R=0 \quad (2.4)$$

The linearly independent solutions of the ϕ part are

$$\Phi_e=\cos m\phi\ ,\ \Phi_o=\sin m\phi$$

The solutions of the θ part are associated Legendre functions of the first kind:

$$P_n^m(cos\theta)$$

of degree n and order m.

The radial part (2.4) can be rewritten with the use of the dimensionless variable $\rho=kr$ and definition of the function $Z=R\sqrt{\rho}$ as:

$$\rho\frac{d}{d\rho}\left(\rho\frac{dZ}{d\rho}\right)+\left[\rho^2-\left(n+\frac{1}{2}\right)^2\right]z=0 \quad (2.5)$$

The linearly independent solutions of (2.5) are the spherical Bessel functions

$$j_n(\rho) = \sqrt{\frac{\pi}{2\rho}} J_{n+1/2}(\rho) \quad (2.6)$$

$$y_n(\rho) = \sqrt{\frac{\pi}{2\rho}} Y_{n+1/2}(\rho) \quad (2.7)$$

Now the functions that satisfy the scalar wave equation in spherical polar coordinates can be obtained:

$$\Psi_{emn} = cosm P_n^m(cos\theta) z_n(kr) \quad (2.5)$$

$$\Psi_{omn} = \sin P_n^m(cos\theta)\, z_n(kr) \quad (2.6)$$

The subscripts e and o denote even and odd respectively and z_n denotes any of the spherical Bessel functions j_n, y_n, $h_n^{(1)}$, or $h_n^{(2)}$. Any function that satisfies the wave equation can be expanded in an infinite series.

The equation of the incident plane wave impinging on the particle will be expressed in spherical coordinates since the boundary conditions need to be imposed on the surface of the sphere. The electric field of the incident plane wave expressed in spherical harmonics will be:

$$E_i = E_0 \sum_{n=1}^{\infty} i^n \frac{2n+1}{n(n+1)} (M_{oln}^{(1)} - iN_{eln}^{(1)}) \quad (2.7)$$

By taking the curl of (2.9) the corresponding magnetic field can be obtained

$$H_i = -\frac{k}{\omega} E_0 \sum_{n=1}^{\infty} i^n \frac{2n+1}{n(n+1)} \left(M_{eln}^{(1)} - iN_{oln}^{(1)}\right) \quad (2.8)$$

Now the boundary conditions must be imposed between the surrounding medium and the sphere,

$$(E_i + E_s - E_l) \times \hat{e}_r = (H_i + H_s - H_l) \times \hat{e}_r = 0$$

Where the subscripts i, s, l denotes the incident, scattered and internal field respectively.

The expansion of the internal fields will be

$$E_l = \sum_{n=1}^{\infty} E_n \left(c_n M_{oln}^{(1)} - i d_n N_{eln}^{(1)} \right)$$

$$H_l = -\frac{k_l}{\omega \mu_l} \sum_{n=1}^{\infty} E_n \left(d_n M_{eln}^{(1)} + i c_n N_{oln}^{(1)} \right) \quad (2.9)$$

The scattered fields will be:

$$E_s = \sum_{n=1}^{\infty} E_n \left(i a_n N_{eln}^{(3)} - b_n M_{oln}^{(3)} \right)$$

$$H_s = \frac{k}{\omega \mu} \sum_{n=1}^{\infty} E_n \left(i b_n N_{oln}^{(3)} + a_n M_{eln}^{(3)} \right) \quad (2.10)$$

Where M and N denote the vector spherical harmonics. The final important point is to write the vector spherical harmonics for the internal and the scattered field.

$$M_{oln} = cos\phi \pi_n(cos\theta) z_n(\rho) \hat{e}_\theta - sin\phi \tau_n(cos\theta) z_n(\rho) \hat{e}_\phi$$

$$M_{eln} = -sin\phi \pi_n(cos\theta) z_n(\rho) \hat{e}_\theta - cos\phi \tau_n(cos\theta) z_n(\rho) \hat{e}_\phi$$

$$N_{oln} = sin\phi n(n+1) sin\theta \pi_n(cos\theta) \frac{z_n(\rho)}{\rho} \hat{e}_r + sin\phi \tau_n(cos\theta) \frac{[\rho z_n(\rho)]'}{\rho} \hat{e}_\phi$$

$$N_{eln} = cos\phi \; n(n+1) sin\theta \; \pi_n(cos\theta) \frac{z_n(\rho)}{\rho} \hat{e}_r$$

$$+cos\phi \; \tau_n(cos\theta) \frac{[\rho z_n(\rho)]'}{\rho} \hat{e}_\theta - sin\phi \; \pi_n(cos\theta) \; \frac{[\rho z_n(\rho)]'}{\rho} \hat{e}_\phi \quad (2.11)$$

The functions π_n and τ_n define the dependence of the fields on the angle θ and is important to examine their behavior.

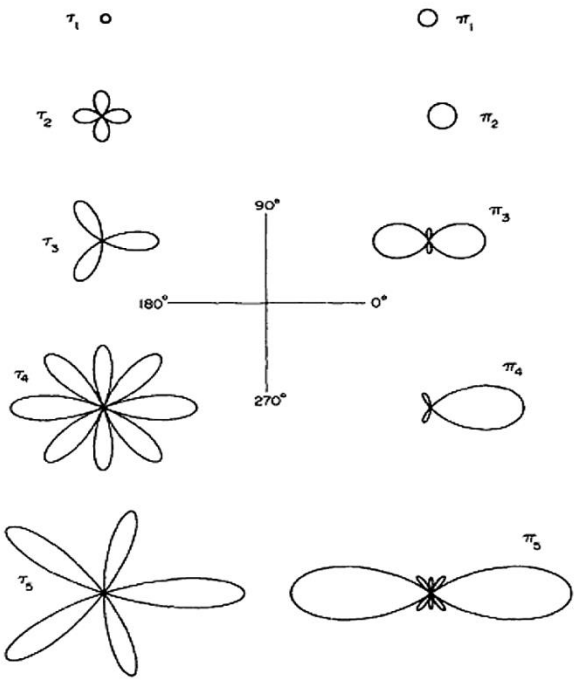

Figure 2: Polar plots of the angle dependent functions π_n and τ_n for n=1-5

Figure 2 shows polar plots of the functions for n=1-5. The angle θ ranges from $0°$ to $360°$. Their values can be both negative and positive with the exception of π_1 which is constant. The number of lobes increases as n goes up, resulting in a narrower frontal lobe. When a polar plot does not exhibit a back-directed lobe means that π_n and τ_n are negative for backward directions. Forward directed lobes are present in all functions, however for alternate values of n the backward lobes vanish. As the size of the particle increases, the number of higher order π_n and τ_n functions included in the scattering diagram also increases. It is important therefore to notice that, according to the behavior of these functions, the larger the particle is, the more intense forward scattering occurs compared to the backscattering resulting in a narrower forward scattered peak. The vector spherical harmonics M_n and N_n are the electromagnetic normal modes of the particle. Two types of modes are possible: transverse electric and transverse magnetic. Transverse electric modes do not have a radial electric field component and transverse magnetic modes do not have a radial magnetic field component.

Figure 2.2[28] shows the normalized radar cross section of a metallic sphere as a function of particle circumference over wavelength (2πr/λ). The picture depicts the dependence of the way light is scattered on the size of the particle. Mie scattering occurs in the region were the particle diameter is between less than 1 and 10 (logarithmic scale).

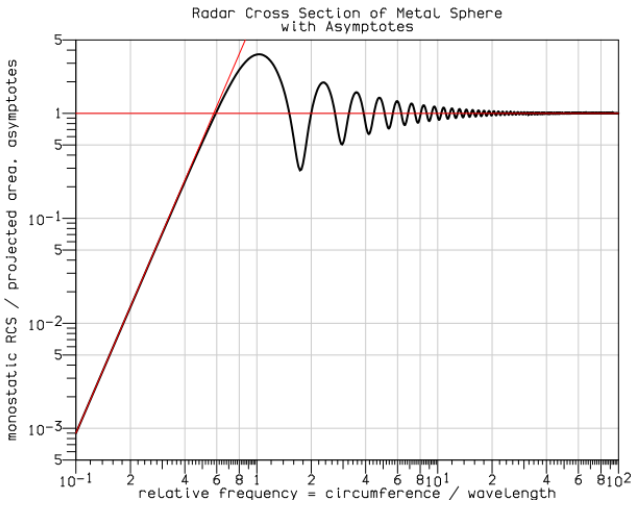

Figure 2: Mie theory calculated radar cross section of a metallic (perfect conductor) as a function of particle circumference over wavelength in logarithmic scale.

2.2: Thin film interference

Following the scattering by the TiO_2 particles, the next step is to examine theoretically how light behaves inside and on the outside surfaces of the thin film. The simple case of a thin film in air will be considered to describe the phenomenon, following the notation of Serway[29] and then the specifications of the experiments will be applied.

The wavelength of light inside the thin film will be λ_n, where n is the refractive index of the film. The film is of even thickness t. The incident light rays are assumed to be almost normal on both surfaces of the film. As shown in the schematic representation of figure 3, incident light is partially reflected and partially transmitted. Ray 1 originated from the reflection of incident wave on the upper surface (A) of the film. Upon reflection, the phase changes by $180°$ in relation to the incident wave. Ray 2 originates from the reflection of the transmitted wave on the bottom surface (B), and experiences no change in phase, because the medium (air) that is reflected on has lower index of refraction. Thus waves 1 and 2 are out of phase by $180°$ if the path length difference is $\lambda_n/2$ which makes them interfere destructively. This consequently reduces the reflection of the thin film.

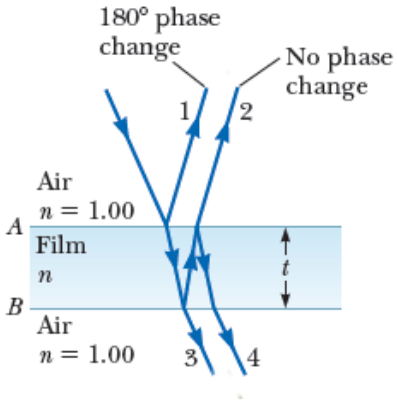

Figure 3: Schematic representation of interference of light in a thin film. The incident wave is partially reflected and partially transmitted. The transmitted part is reflected at the bottom surface and transmitted at the top interference with the reflected part.[29]

In the case that $2t = \lambda_n/2$, waves 1 and 2 are out of phase so they interfere destructively. This gives rise to the general condition for destructive interference which is:

$$2nt = \left(m + \frac{1}{2}\right)\lambda \quad m = 0,1,2,\ldots \quad (2.13)$$

The general condition for constructive interference:

$$2nt = m\lambda \;\; m = 0,1,2,\ldots \quad (2.14)$$

These conditions apply for the case of where the medium above and below the thin film has lower refractive index than the thin film. This is the case in our experiments where the thin film lies on top of glass substrate.

The procedure is however more complex, as it does not involve only a simple transmission and reflection of the incident beam. The part of the incident wave that is transmitted in the film can undergo multiple internal reflections, each leading to a transmitted part of the wave in the upper and lower surface of the film. As described by Grunwald[30], a light wave propagating through a thin film is undergoing multiple internal reflections governed by Fresnel reflection. This gives rise to Fabry-Perot etalon resonances which are spectral bandwidth, angular distribution, absorption, dispersion and scattering dependent. Figure 4 displays a dielectric thin film of uniform thickness h and refractive index n_L on top of a substrate of n_S. The top and bottom surface of the film act as Fabry-Perot etalons creating multiple beam interference.

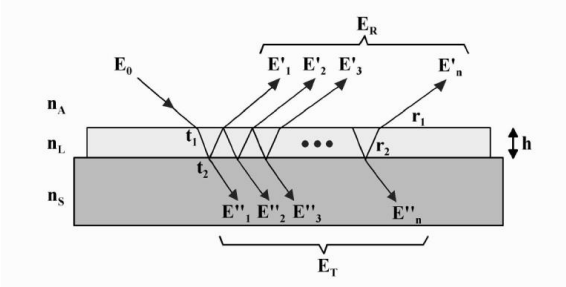

Figure 4: Thin film of uniform thickness h and refractive index n_L placed on top of substrate of refractive index n_S. E_i' and E_i'' denote the partially reflected and transmitted field amplitudes respectively, from which the total reflected and transmitted field can be calculated.[30]

The phase of the wave depends on the thickness of the film. The Fabry-Perot resonator is able to sustain a constructive resonance when $t = \lambda_n/2$. Silicon and silicon nitride have larger refractive index than both glass and air. The thickness of the glass substrate is considered to be infinite, since it is much larger than the thickness of the film.

2.3 Fano resonance

The final step is to describe theoretically the Fano resonance. In general, a Fano resonance occurs when a scattering mechanism originating from a continuum of states, interferes with a scattering mechanism rising from excitation of discrete states. The description of the phenomenon will be first done classically, then the quantum particle approach by Fano will be described and in the end they will proceed to light scattering.

First the classical description will be used, following the explanation through the example of two oscillators with a driving force[31]. A typical example where resonances occur is the periodic force driven harmonic oscillator. The amplitude of the oscillator is maximized, when the driving force reaches a frequency that is close to the Eigen frequency of the oscillator causing a resonance. The opposite effect can occur, when the response of the system is cut off by a resonant mechanism. An example is when a damped periodically driven harmonic oscillator, is coupled weakly to another damped oscillator as depicted in figure 5 (a). The oscillators have Eigen frequencies ω_1 and ω_2 for which there are two

resonances close to their values. One resonance is caused by the common increase in amplitude when ω_1 is reached. The amplitude of the other resonance however is displaying an intensely sharp decrease when it is close to ω_2. As shown in the graph of fig. 5 (b), the first resonance exhibits a symmetric Lorentzian profile while the profile of the second resonance is asymmetric. This asymmetric line shape of the resonance was first described by Fano, explaining the inelastic electron scattering and auto ionization. An atom can be excited by a photon in a range of different ways. The simplest is through

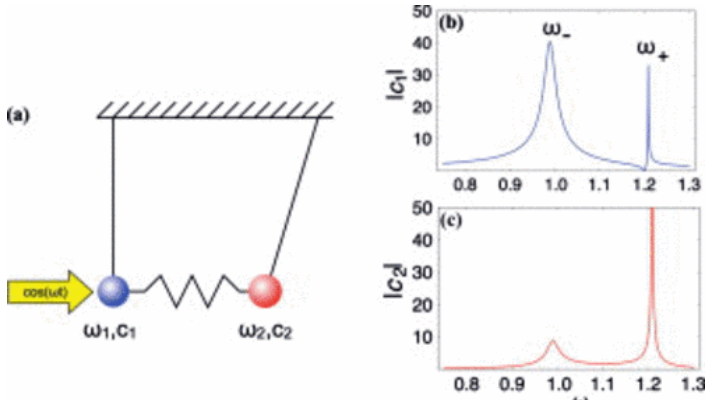

Figure 5: a) Schematic diagram of the weakly coupled damped oscillators. One is driven by a periodic force. The graph b) corresponds to the amplitude of the driven oscillator and c) to the coupled one. The driven oscillator shows symmetric and asymmetric resonances while the coupled exhibits only symmetric ones.[31]

excitation of the inner-shell electron beyond the ionization energy. The atom can also be excited into a quasi-discrete level, which can be ionized spontaneously through injection of an electron in the continuum, called an auto ionizing level. Two electrons can be excited simultaneously by the same photon, if the electrons have their excitation energies at the same order of magnitude and combined surpass the atom ionization threshold. The electrons interact with each other, eventually resulting in one falling to a lower state and transferring its energy to the other one that is discharged in the continuum, which causes the auto ionized state to decay. Atomization acts as a coupling mechanism of bound states to a continuum of states. Interference takes place when two states couple. The scattering cross section is given by the relation:

$$\sigma = \frac{(\epsilon + q)^2}{\epsilon^2 + 1} \qquad (2.17)$$

Where q is the asymmetry parameter and $\epsilon = 2(E - E_F)/\Gamma$ a reduced energy, E_F the resonant energy and Γ the width of the auto ionized state. The above formula implies that the Fano profile exhibits exactly one minimum and one maximum

$$\sigma_{min} = 0, \text{ for } \epsilon = -q$$

$$\sigma_{max} = 1 + q^2, \text{for } \epsilon = 1/q \tag{2.18}$$

The q parameter determines the ratio of the probabilities of transition to the mixed state and to the set of continuous states. When |q| approaches infinity there is only a weak transition to the continuum and the transition to the discrete state dominates, giving a Lorentzian line shape to the profile. When q is close to one, the continuum and discrete transition are comparable creating the typical asymmetrical line shape. For the case when q=0 the profile exhibits a symmetrical dip referred as anti-resonance. The characteristic asymmetrical line shape of Fano resonance is caused by destructive interference.

Transmission and reflection spectra of light scattering in optical systems such as semiconductor nanostructures can also exhibit Fano resonances[32]. When light that is scattered by a resonant process interferes with light scattered by a non-resonant one, a Fano line shape can be obtained. This is due to the fast varying amplitude and phase of the resonant process, compared to the non-resonant. If the scattering mechanisms are of comparable magnitude the Fano line shape becomes more prominent. The total scattering cross section (2.17) can be rewritten as:

$$\sigma_{TS}(\omega) \propto \frac{\left(q\frac{\Gamma}{2} + \omega - \omega_0\right)^2}{\left(\frac{\Gamma}{2}\right)^2 + (\omega - \omega_0)^2} \tag{2.19}$$

Where ω_0 is the resonant frequency and Γ is the full-width at half-maximum of the resonance? Here the parameter q expresses the ratio of the resonant scattering amplitude to the non-resonant scattering amplitude and the same rules apply as in the atom light interaction case. The analogy of the Fano resonance originating from scattering of a quantum particle to light being scattered by a nanoparticle is further proven by Tribeslky et al. [33], where the exact Mie solution to the diffraction problem and a 1-D model were implemented. As described in the first section of the theory, the process of the scattering of light can be described by separating the fields to incident, internal and scattered. The incident light once inside, gives rise to resonant modes inside the particle. Light can alternatively bypass the nanoparticle,

and non-resonantly cause excitation of localized modes that have their Eigen frequencies way off the close vicinity of ω.

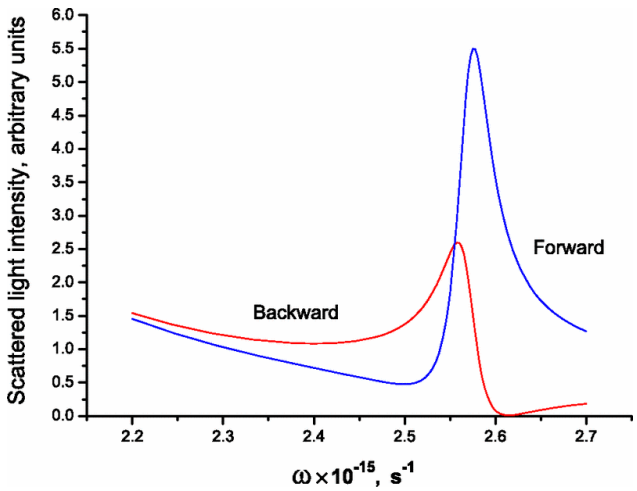

Figure 6: Characteristic Fano resonance profiles originating from elastic scattering. Blue line represents forward scattering and red line backward scattering by a nanoparticle. The graphs were obtained by calculating the exact Mie solution in the region near the quadrupole resonance.[33]

The incident and re-emitted light interfere creating a complicated near-field structure that can either powerfully enhance or suppress the electromagnetic field. In other words, constructive or destructive interference may occur. These two possible pathways of the incident light are the corresponding resonant and direct scattering, which makes the analogy of the Fano resonances of a quantum particle that is scattered by a quasi-discrete level potential evident. Figure 6 displays typical Fano resonances from elastic light scattering. Figure 7 shows Fano resonances in scattering cross sections as a function of asymmetry parameter q.

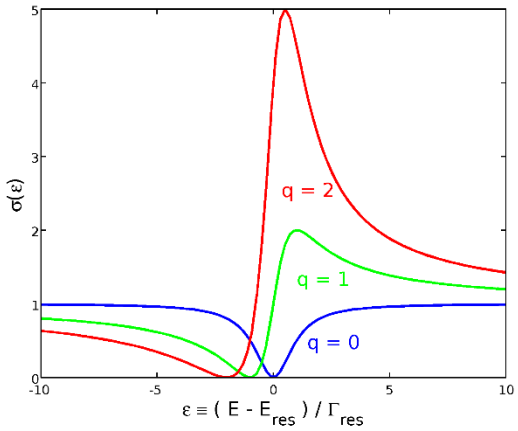

Figure 7: Scattering cross section as a function of asymmetry parameter q [35]

Chapter 3

Experiments: Method and setup

The experimental part can be divided in three sections. First section is the fabrication of the samples using the cluster source. Second is the characterization of the samples with mainly AFM and additionally transmission electron microscopy (TEM) and scanning electron microscopy (SEM) microscopy. Third and final part is the optical experiments with the UV-Vis-NIR spectrophotometer. In each part a brief description of the procedure and setup will be given, as well as some technical aspects of the equipment.

3.1. Fabrication of samples

The sample itself consist of two parts: The deposition of the thin film on a glass substrate using the sputter source and the deposition of nanoparticles using the cluster source. First the sample is transferred in the sputter chamber where the thin film of Si or Si_3N_4 is deposited. For each film type three thicknesses were selected. Silicon thin films of 30 nm 70 nm and 160 nm were fabricated by performing sputter depositions of 500 s, 1000 s and 1500 s respectively. The Si_3N_4 films were 37 nm, 86 nm and 136 nm thick corresponding to 1100 s, 1380 s and 1680 s long depositions.

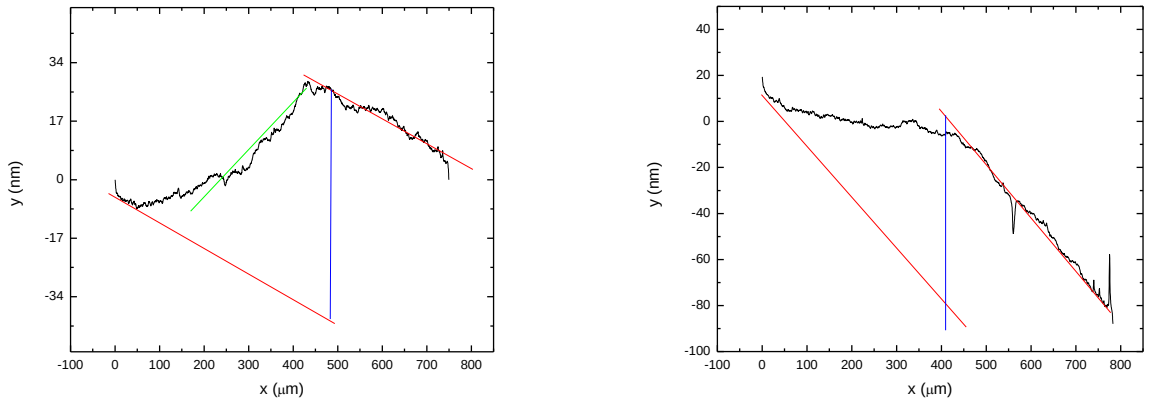

Figure 3.1: DEKTAK measurements for the 70 nm Si film (a), and for the 86 nm SiN film (b) The step in the graph indicates the transition from glass to the film. The blue line indicates the probable thickness

The thicknesses of the Si and Si_3N_4 samples were selected by calculating standing wave conditions for wavelengths of 300 nm, 500 nm and 700 nm, which is the measurement range. The deposition time gives us an estimate of the thickness of the film. In order to have more accurate information for the thickness DEKTAK was performed on the reference samples. In figure 3.1 the results of the 30 and 70 nm thick Si film are shown.

For the DEKTAK measurements of 30 nm thick Si film the estimated thickness with a deviation of $+3\ nm$. Is very close to the aimed value. The estimated 70 nm film appears to be consistent as well. The best measurements are chosen since not all of them are successful. The slope of the glass should be taken into account and the roughness of the glass, which in some cases reduces considerably the accuracy of the measurements.

The measurements for the silicon nitride were less successful making the determination of the thickness slightly more difficult, however it was found that the 37 nm film has the expected thickness. The 86 nm film has half the expected thickness and the 136 nm film has more than half compared to the expected one. The above estimates are in perfect agreement with the deposition times of Si_3N_4if we assume a linear relation.

The next step is the deposition of the TiO_2 nanoparticles using the cluster source. After the deposition of the thin film the sample is transferred to the central chamber in vacuum and placed in front of the cluster source. After a study of the TiO_2 particle deposition conditions with respect to particle size and density the deposition parameters were selected and varied to obtain different type of samples. The power source was set to DC and the Ar gas flow to 20 sccm for the Si samples and 10 sccm for the Si_3N_4 samples. For an incidental sample with Si_3N_4 were additional oxygen was used, the Ar gas flow was lower. The key parameter is the aggregation distance. For the Si samples, aggregation distances of 40 mm and 60 mm were selected, while for Si_3N_4 20mm and 40 mm. In the initial phase of the research an extensive amount of cluster source depositions on glass samples was performed for various aggregation distances. It was found that the previously mentioned distances are the optimal. To understand the importance of the parameters a brief description of the cluster source will be given.

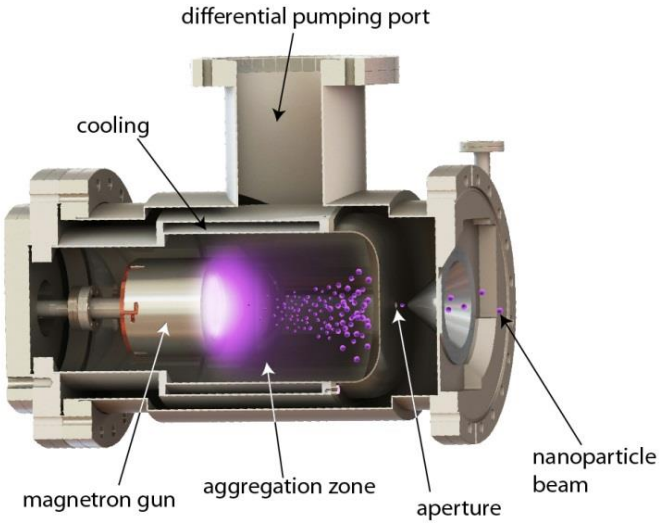

Figure 3.1: Schematic illustration of the cluster source during operation. The magnetron creates a discharge, emitting nanoclusters. The argon gas drives them towards the aperture. The aggregation zone can vary in length affecting the size of the clusters

The nanocluster source is an ultra-high vacuum operating device. The clusters are generated through a DC or RF magnetron discharge. DC is used for conductive targets while RF for insulators. The discharge creates a cloud of atoms. Argon gas flows inside the water-cooled aggregation tube where the atoms aggregate into particles by cooling. The gas drives the particles to collide with each other forming larger groups called nanoclusters. The nanoclusters then exit the aggregation tube through a nozzle and they are deposited on the sample. To change the nanocluster size, the parameters of electrical power, gas flow and aggregation distance and type of gases can be tuned. The aggregation distance is the distance between the magnetron and the aperture and by adjusting it is possible to vary the duration of clusters' presence in the aggregation region and thus their size.

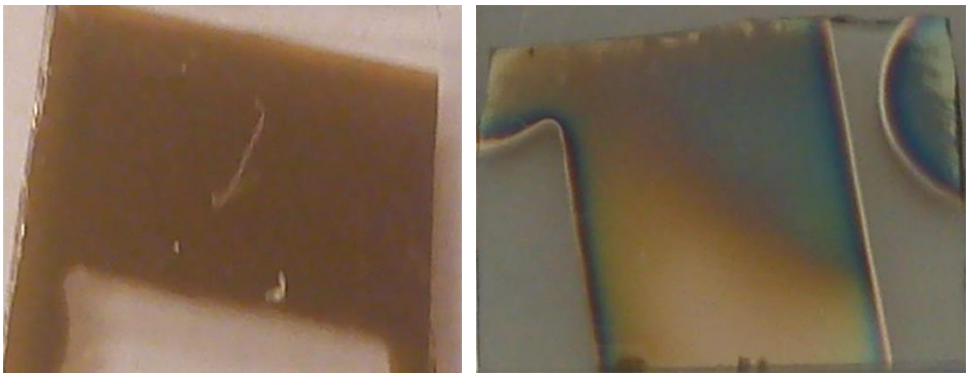

Figure 3.2: Photographs of the 160 nm thickness reference (a) and cs 886 also 160 nm thickness.

In figure 2 photographs of a reference and a sample belonging to the series of 160 nm thick Si film. The TiO_2 particles are forming a visible dark layer covering almost half of the sample surface.

3.2. Characterization

After the nanoparticles were deposited it was necessary to characterize them, in order to acquire information about their height (which corresponds to their size) and the density of the deposition. AFM (Atomic Force Microscope) microscopy was used extensively throughout the experiments for that reason with additional TEM and SEM. The AFM is able to measure the roughness of the surface of the sample. This is achieved by using a cantilever, made of silicon or silicon nitride, with a very sharp peak to scan the surface of the sample. When the tip is very close to the sample interaction forces set in. Tapping mode was used for the scanning of samples. During tapping mode operation, the tip of the cantilever does not make contact with the surface of the sample, instead it oscillates above the surface. In that way any dragging of particles by the tip is avoided. Typically, the scan area is 10x10 μm and a few times 20x20 μm. In fig. 3.3 the AFM used is shown together with a schematic diagram of the operation.

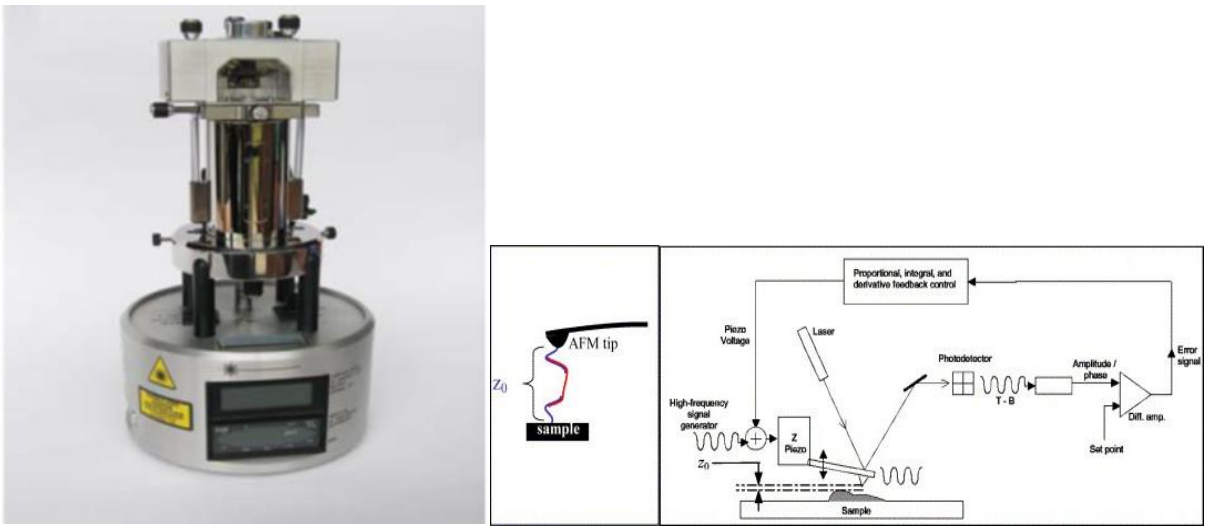

Figure 3.3: a) AFM microscope. The photo shows the model that was used during experiments b) Schematic representation of the taping mode of operation.

After the image was acquired, analysis on the image was performed using AFM image processing software namely WSXM and Gwyddion. The analysis involved measuring of the height of the nanoparticle by taking its profile. This was done for several parts of the sample and depended on the cluster density.

Although AFM provided valuable information, additional information such as the shape of the clusters was needed, therefore TEM and SEM was performed. For the TEM two depositions on TEM grids were performed one for 40 mm and on for 60 mm aggregation distance. The power was set to 0.163 A, the gas flow to 20 sccm and the deposition time was 10 min for both.

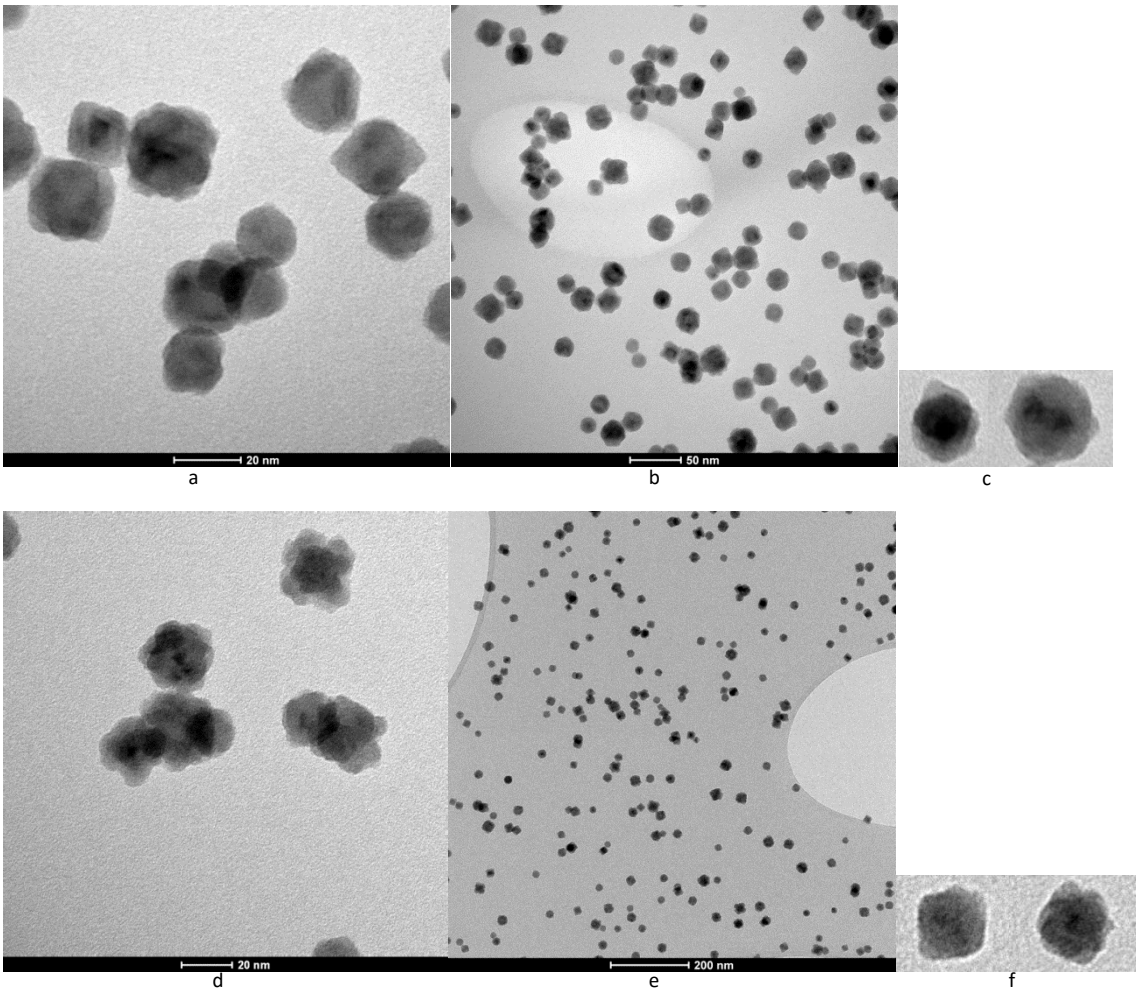

Figure 3.4: TEM images for samples cs 869 (a, b, c) and cs 870 (d, e, f). For cs 869 the aggregation distance was 40 mm and for cs 870 60 mm. The shape of the particles resembles strongly a square. Comparing b) and e) we can see that aggregation length of 40 mm provides a denser population of particles. C) and f) depict individual clusters where the stacked arrangement can be observed.

Figure 3.4 depicts TEM images of samples cs 869 and 870. The characteristic square-like shape of the clusters is evident in all pictures. Looking at fig. 3.4 a) and d) one can observe that some parts in the clusters are darker. Since the particles are partially transparent this trait indicates that the particles are stacked on top of each other during deposition. B) and e) provide a zoomed out view, showing denser distribution on 869 (40 mm aggregation length) compared to 870 (60 mm aggregation length).

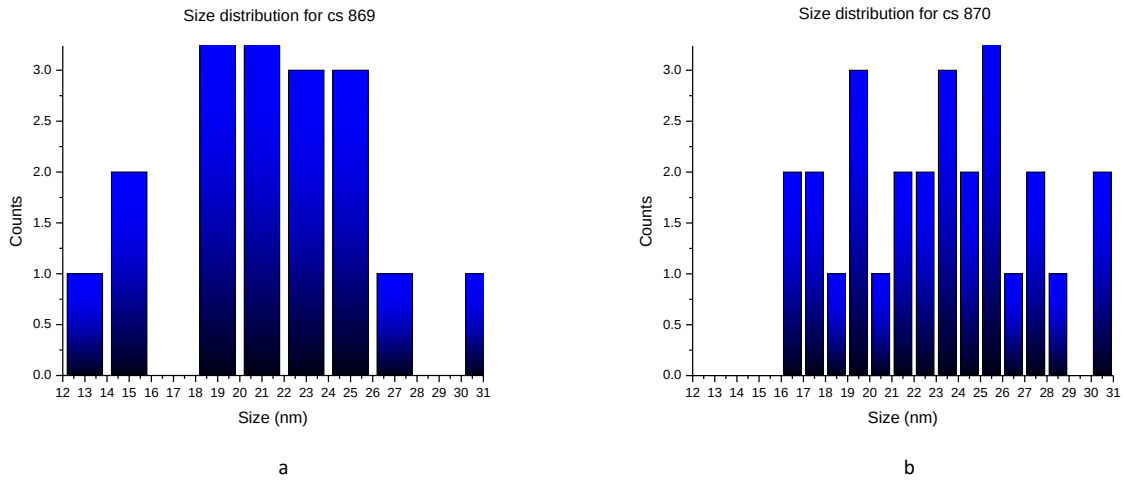

a b

Figure 3.5: Particle size distribution histograms for cs 869 (a) and cs 870 (b). The clusters are in the same size range in both samples with maximum size 31 nm. The histogram for cs 869 exhibits four columns that reach or surpass three counts. For cs 870 three columns are equal or surpass three counts. The columns are broader for cs 869.

In fig. 4 the size distribution histograms for the TEM samples are shown. The histograms have similar size range reaching a maximum of 31 nm. For cs 869 the distribution exhibits peak in a size range between 18 nm and 25.5 nm. In (b) the three observed peaks are distinct.

The square-like shape of the particles is also visible in the SEM images of trial samples cs 694, 701 and 708 as shown in fig. 3.6. Trial samples are the ones that contain only TiO_2 clusters without a thin film. The stacked arrangement of the clusters can be observed as well

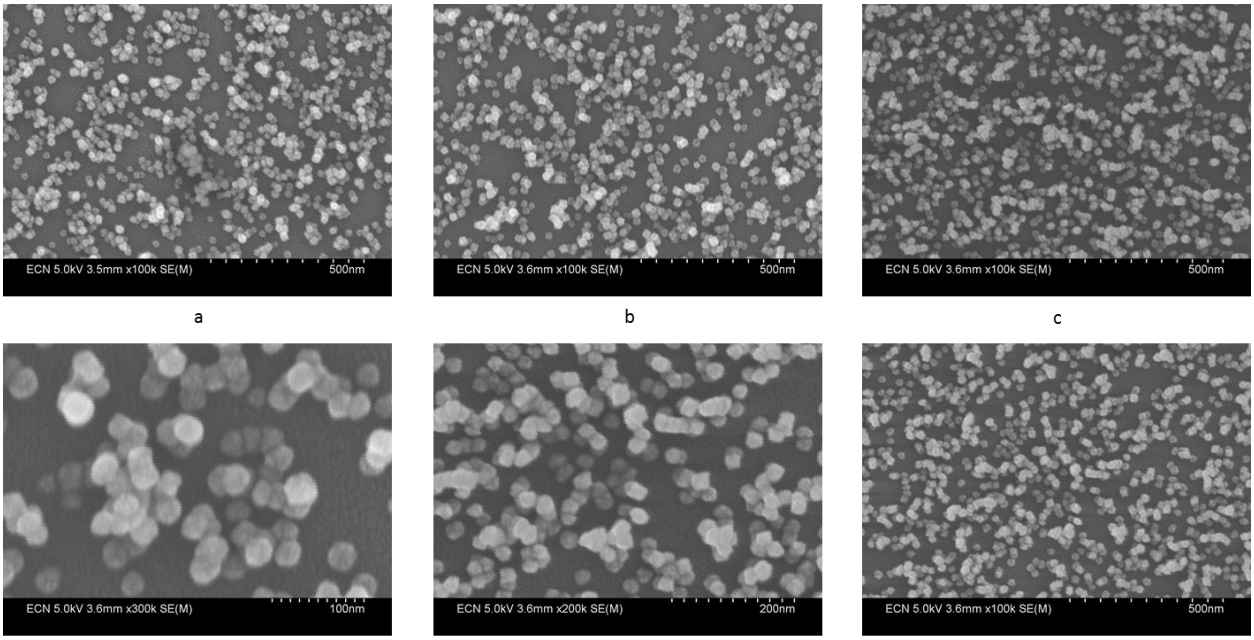

Figure 3.6: SEM images of trial samples cs 694 (a), cs 701 (b) and cs 708 (c). In (d) and (e) a zoom in in samples cs 701 and 708 respectively is performed were it can be seen clearly that the particles have a cubic shape. The picture in (f) belongs to cs 708 and is similar to (c).

3.3 Optical experiments

The final and main stage of the experiments was to perform optical measurements on the sample using the UV-Vis spectrophotometer. The goal was to obtain the reflection and transmission spectrum of the samples and from that calculate the optical absorption. For each sample the Total reflection, diffuse reflection and transmission were measured. Each measurement was repeated thrice for every sample. Every time the position of the sample with respect to the beam was changed by rotating it slightly and moving it up and down. The wavelength range selected was from 250 nm to 1200 nm. In figure 3.7 a schematic diagram of the spectrophotometer is shown.

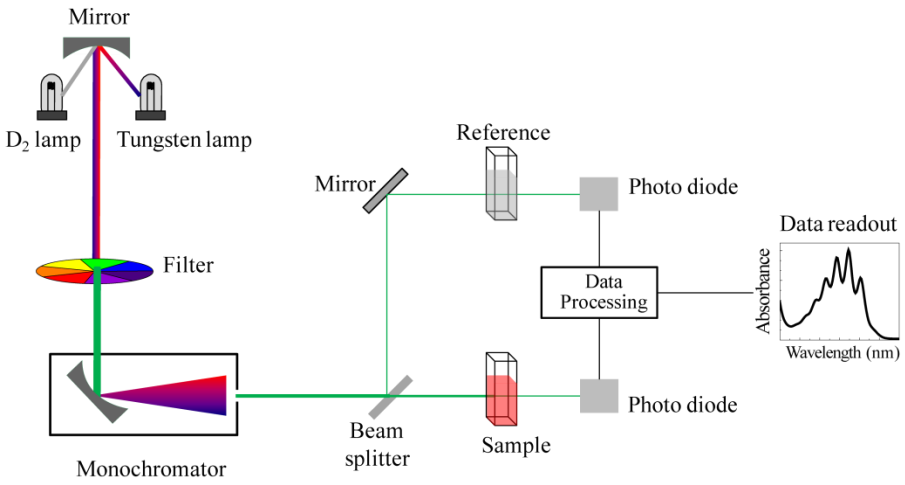

Figure 3.7: Schematic diagram of the UV-Vis spectrophotometer.

3.4 Simulations

In order to compare the experimental results with the theory, finite difference time domain (FDTD) simulations were performed using Lumerical FDTD solutions. The setup consists of a cubic TiO_2nanoparticle placed at the center of a-Si thin film on top of glass substrate. The reference was simulated as well. The parameters varied were the particle size and the thickness of the film. The thickness for a-Si was set to 30 nm, 70 nm and 160 nm, and for Si_3N_4 to 37nm, 86 nm and 136 nm, corresponding to the experimental settings. For each thickness a total of four simulations was performed one for each particle size plus one for the reference. Three particle sizes were chosen: 20 nm, 40 nm and 70 nm. The glass thickness was set to 100 nm in all cases. A polarized plane wave type light source was chosen set in the same wavelength range as the optical experiments. Two monitors were used to obtain reflection and transmission measurements, and three for the cross sections of the electric and magnetic field inside and around the particle and the thin film. In figure 3.8 the setup is shown as exported from the FDTD solver software.

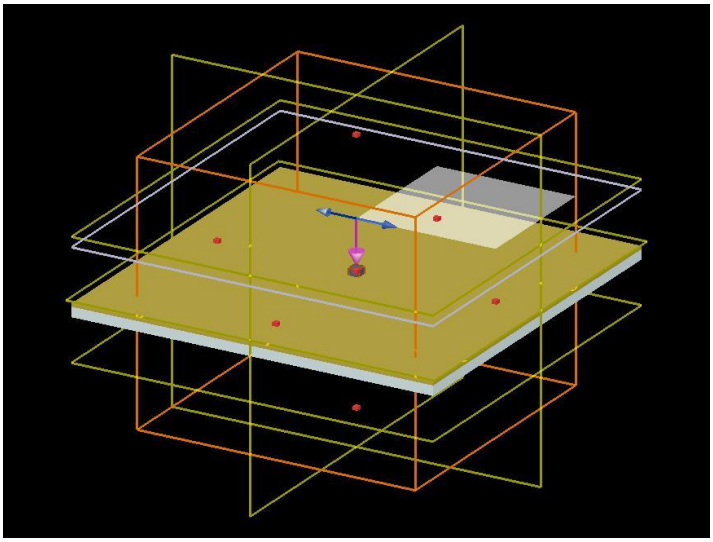

Figure 3.8: Perspective view of the typical simulation setup. The orange box is the simulation region which is 2x2x2 μm. The yellow squares are the monitors. The two parallel monitors above and below are for reflection and transmission respectively. The rest are for the cross sections of electric and magnetic field.

The orange box is the simulation region the size of which is 2x2x2 μm. A fine mesh region is used for the particle with a size of 1.42 nm. The boundary conditions were chosen to be periodic. The gray square above the surface is the light source. A purple arrow indicates the direction of propagation and the blue arrows the direction of polarization. Two monitors parallel to the surface located well above and below it is implemented to measure reflection and transmission respectively. Another three monitors were implemented to obtain the cross sections of the electric and magnetic field, each one normal to an axis.

Chapter 4

Results

4.1 Analysis method of optical measurements

As was mentioned in the experimental section, the total reflection, diffusive reflection and transmission were measured. Two systems were used, TiO_2 on a-Si and on SiN thin films, with three different thicknesses for each. For the first two thicknesses of a-Si, six samples were created and for the thickest film eight samples. For SiN a total of six samples were created, two for each thickness. We first take measurements for the reference and afterwards for the samples. For each sample, three measurements are taken, rotating and moving the sample each time to account for position dependent effects. For the analysis the average of each set of three measurements was taken. If a measurement is significantly different from the rest of the set, we discard it because the sample was likely not positioned well. To calculate the difference of the sample from the reference (bare glass with thin film) by subtracting the average of the three measurements for the reference, from the average of the three measurements of the sample.

The next step is to calculate the absorption. We use the formula:

$$A = 1 - R - T \quad (1)$$

Where A is the absorption, R the total reflection and T the transmission. Again we use the averaged values of the measurements of all the samples and the references. We obtain the difference of the sample from the references the same way as with the reflection and transmission.

Although here we present the measured data, it is possible to calculate how much light is reflected, transmitted and absorbed by an individual particle. This can be obtained by taking a correction factor of the average free area around a particle divided by the particle size.

We may now proceed with the presentation and discussion of the results, separately for each Si thickness.

4.2 Optical results

4.2.1 Si thickness: 30 nm

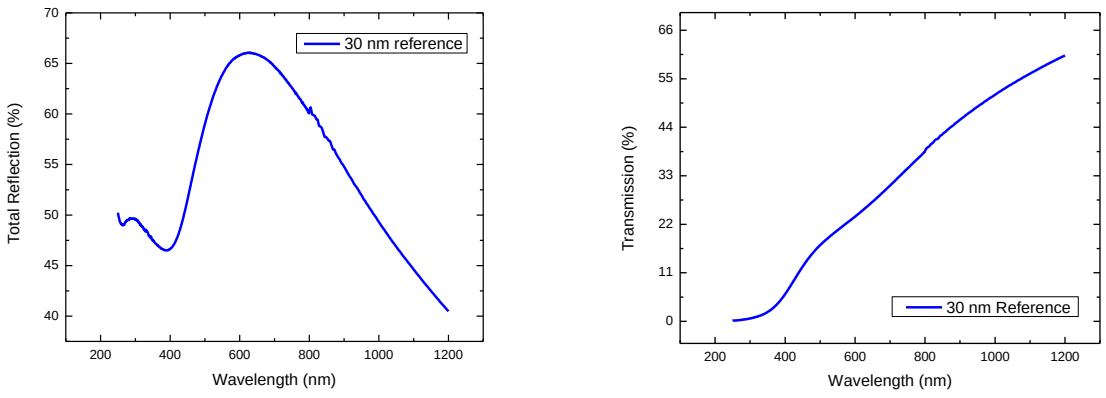

Figure 4.1.1: Raw optical data of total reflection (a) and transmission (b) for the 30 nm thick Si reference sample ss 182. The UV-Vis measurements were performed in the range of 250 nm to 1200 nm.

Figure 4.1.1 shows the unprocessed optical measurements of the optical reflection and transmission for the reference sample. Total reflection (a) shows a maximum at 622 nm while transmission shows no peak.

We first present the results of the thinnest film of 30 nm. We produced six samples of 30 nm thick Si, using aggregation lengths of 40 and 60 mm. The particle densities are high in all samples reaching up to $76\ particles/\mu m^2$. The results are shown separately for selected samples.

the very first sample (cs 864) was made with a cluster source deposition of 3 minutes with 40 mm aggregation length. The gas flow was 20 sccm and the power was 0.163 W. As we can see in figures 4.1.1a and 4.1.1b, there is a clear peak in reflection around 450 nm and a clear broad peak in transmission around 820 nm.

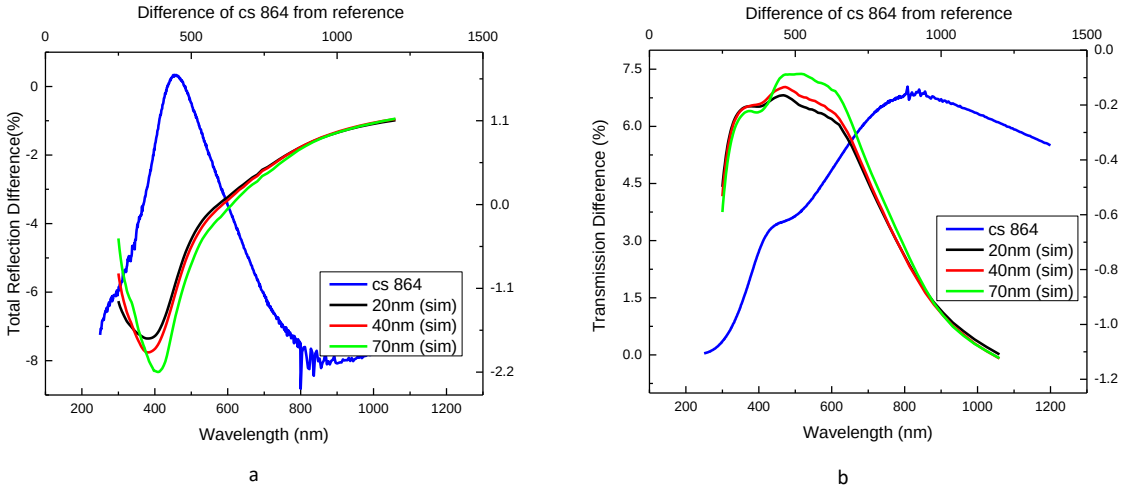

Figure 4.1.2: a) Total reflection difference as a function of wavelength for sample cs 864. The peak is at 820 nm. The peak is very broad with a FWHM at 796 nm. b) Transmission difference as a function of wavelength for sample cs 864. Simulations for different particle sizes are included represented by the green red and black lines.

The maximum difference in reflection is 0.44 %. This value lies in a very short interval where the graph is positive, from 431 nm to 481 nm were the peak is located. The rest of the graph is negative which tells us that the sample with particles reflects less light. The graph of transmission on the other hand is entirely positive, indicating more transmission in particle containing sample. The maximum value of the transmission difference is 6.99 %. Comparing with the raw optical data of the reference (fig.4.1.1) one can see the clearly different behavior. The graph of total reflection shows a peak at 700 nm indicating a shift of 250 nm towards UV for the particle sample. The transmission measurements for the reference show no peak at all. The above facts indicate that there is a clear effect of the TiO_2 nanoparticles. The simulations are predicting different results. In reflection no peak is observed, instead there is a minimum at around 400 nm moving slightly towards infrared as the particle size increases. In fig 4.1.1.b the transmission agreement between simulation and experiment requires a shift of the curves. The peaks are between 462 nm and 497 nm again slightly shifting towards infrared. These positions are far away from the experimental peaks. The sign of the graph is different showing negative results for the entire spectrum. The difference in sign between experiments and simulations is probably due to the deviations between film thickness and the lower particle density in the simulation setup. Diffusive reflection is not shown separately since it does not provide a strong signal.

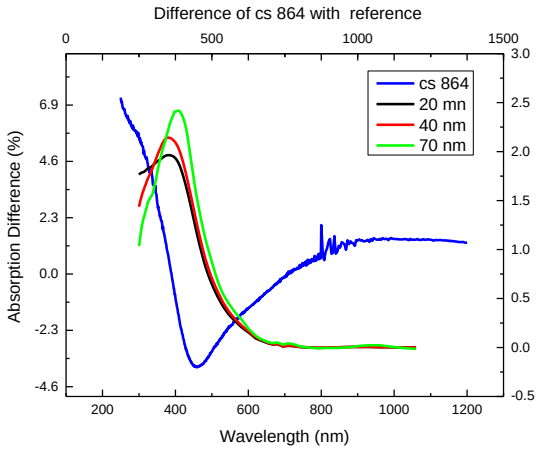

Figure 4.1.3: Absorption difference for cs 864. The graph is negative from 388 to 702 and minimizes at 460 nm taking a value of -3.87 %.

By using equation (1) we calculated the absorption and then the absorption difference between sample with particles and the reference without particles. The results are presented in figure 4.1.2. The results are plotted in figure 4.1.2. The difference is positive everywhere except around the minimum seen at 460 nm where it has the value -3.87 %. In the UV range starts with the highest value and drops quick.

We need to obtain more information about the characteristics of the particle, and more specifically the particle height. With this information we would be able to calculate the particle optical cross section.

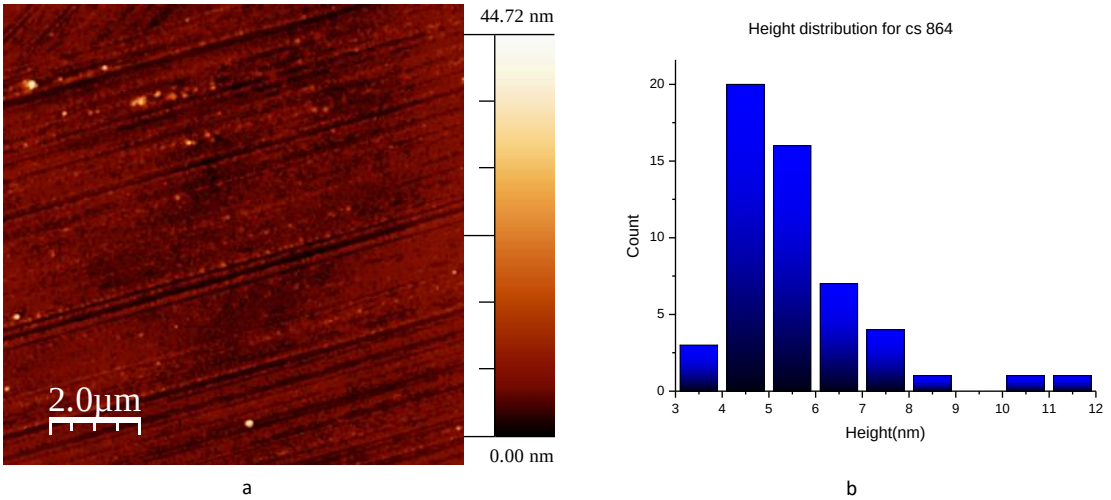

Figure 4.1.4: AFM scan image a) and height distribution b) for cs 864. The main particle height is 4-6 nm. The bin size is 1 nm. The histogram was created by counting the particles in a 1x1 µm selected area of the AFM image. The particle density is $53\ particles/\mu m^2$. The scan area is 10x10 µm.

shows the histogram obtained for sample cs 864. As we can see the main particle size is between 4 and 6 nm. There are few smaller clusters and the maximum height is 12 nm.

The area used for the counting of the clusters and measuring of their height was 1x1 μm. Figure 4.1.3a depicts the AFM scan image of the sample. The deposited clusters are deposited on stripes which were in the glass before deposition, likely caused by the manufacturing. The majority of the clusters is very small with some higher sparse clusters. According to the z scale attached next to the image, the maximum height is 44 nm. This is due to single isolated particles that are present in the scan but are not included in the counting. The stripes are an exception since as we will see in the next samples the clusters do not form lines. Instead they are deposited in a random arrangement. Only sample cs 868 features a similar effect. We can see that the surface density is high measuring 53 particles/μm^2.

The sample cs 868 was created with a longer nanoparticle deposition time of 30 minutes. The rest of the parameters are the same as in the previous samples. The UV-Vis optical measurements of total reflection and transmission are presented in the following graphs with simulations included.

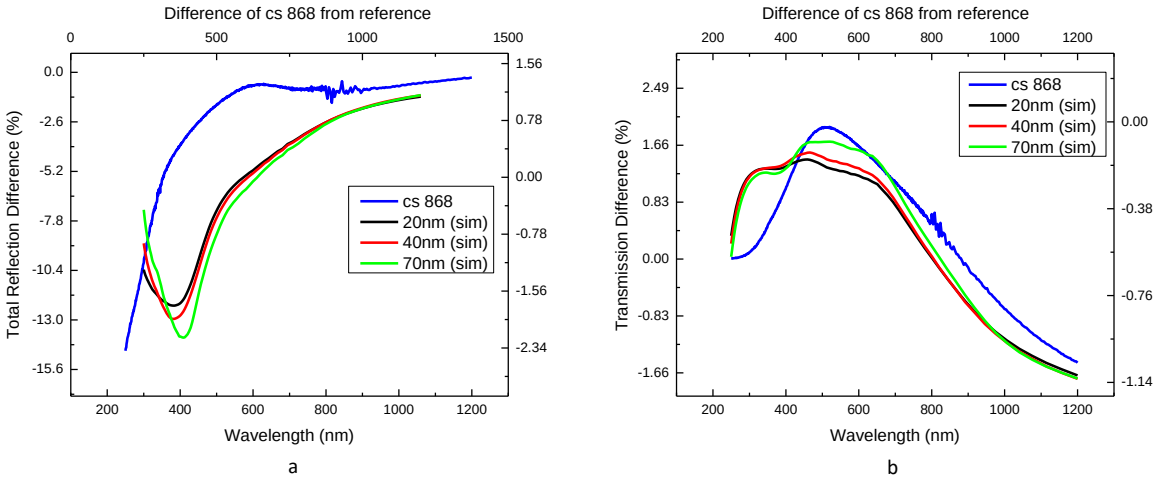

Figure 4.1.5: Total reflection a) and transmission b) difference for cs 868.The light green, red and black lines are the results of the simulations. The peak of transmission is at 519 nm giving better agreement with the simulations.

As we can see in figure 4.1.9a, no clear peak is present. There is only a very small bump in the reflection, that can be identified as a peak at 628 nm, for the difference of the sample from the reference, with a maximum value of -0.54 %. The experimental results partially agree with the simulations; a wavelength shift is likely required due to a difference in particle size or film thickness. The reflection tends to decrease at 500 nm in both cases as with the previous sample. In the simulations however, we have a

minimum at 400 nm and the reflection increases, while in the sample continues to decrease. Interestingly the transmission appears to be in a very good agreement with the simulations. The transmission peaks at 519 nm with a maximum of 1.95 %. The simulated results for the 70 nm cluster peak at 517 nm, perfectly matching the experimental ones. The above results are as with the previous sample very different in comparison with the raw optical data of the reference sample. While there is no peak in total reflection for the particle sample, there is an intense peak in transmission showing the effect of the particles. This peak is also more well defined compared to sample cs 864 as well as in a different position in the spectrum.

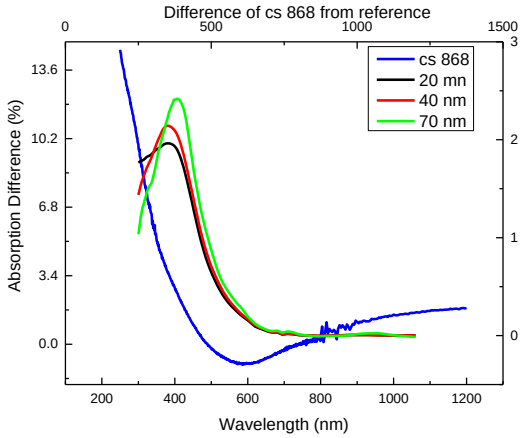

Figure 4.1.6: Absorption difference as a function of wavelength for cs 868 with simulations. The graph reaches a minimum at 588 nm giving -1 %. The peaks of the simulations are located at 359 nm for the 20 and 40 nm particles and at 383 for the 70 nm particle.

The resonances are again very broad, with FWHM of 518 nm for the blue line, and 536 nm for the green line. The sign conflict now is less intense since in the experiments the difference is positive from 461 nm to 575 nm.

Figure 4.1.10 depicts the absorption difference, which has its highest value at 250 nm in the UV range for the experiment and decreases rapidly, reaching a minimum at 588 nm. The minimum point of difference has a negative value of -1% in contrast to the simulations that show maximums at 383 and 359 nm. The graph is as usual starting from its highest point at 250 nm and decreases fast, turning negative between 486 nm and 643 nm and becoming positive for the rest of the spectrum. The graphs of the simulations behave fairly similar regarding the decrease after 400 nm although there is no minimum point near 600 nm. For the 20 and 40 nm particle a peak is shown at 359 nm and for the 70 nm particle the peak appears at 383 nm.

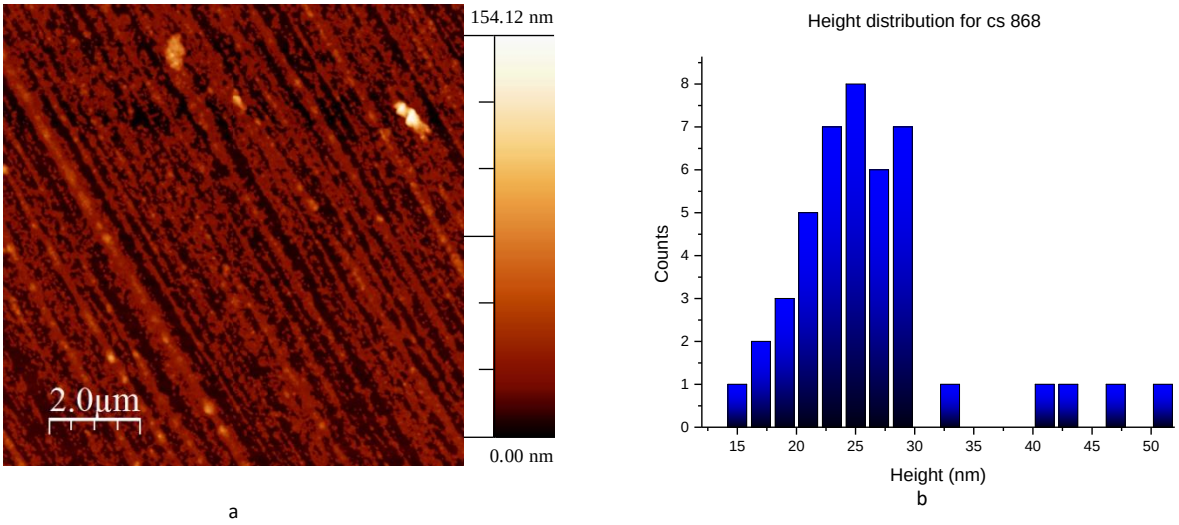

a b

Figure 4.1.7: AFM image and height distribution histogram of cs 868. The scan area of the AFM is 10 μm^2.The z color scale is attached next to it. The selected area of the AFM image for the counting of the particles was 1 μm^2. The particle density is $44\ particles/\mu m^2$.

Figure 4.1.7 a) shows the AFM scan image of the sample. It is densely populated with particles ranging from 15 nm to >50 nm, with a dominant height in the interval of 20-30 nm. The clusters surpassing 30 nm are much sparser. The deposited particles again followed straight lines due to preformed lines in the glass substrate. The particles were smaller sized (20< nm), with interleaving larger ones. The picture is similar to cs 864 in terms of particle arrangement; however, since there is not a clear peak in reflection the interpretation will be slightly different.

4.2.2 Comparison with estimated standing waves

The resonance peaks were calculated according to the conditions for destructive and constructive interference in thin films using the relations shown in theory for different integers m (1,2, 3...). Here shown are the results obtained for the values of m (1,2, 3…) that are closer to the experiments. The results are presented in the tables 4.1. (a). and (b) for reflection and 4.2 (a), (b) for transmission.

Sample	λ exp (nm)	Si n	λ (nm) m=1
cs 865	-	-	-
cs 864	-	-	-
cs 867	843	3.86	231.6
cs 868	519	4.46	267.6
cs 871	505	4.46	267.6
cs 872	516	4.46	267.6

a

Sample	λ exp (nm)	Si n	λ (nm) m=0
cs 865	-	-	-
cs 864	-	-	-
cs 867	843	3.86	463.2
cs 868	519	4.46	535.2
cs 871	505	4.46	535.2
cs 872	516	4.46	535.2

b

Table 4.1: Tables containing the experimental and calculated peaks for reflection for destructive (a) and constructive (b) interference for the samples with thickness 30 nm. Exp stands for experimental. The empty cells are due to the absence of visible peaks in the graphs of reflection for the corresponding sample. The results are shown for the integers m that give the closest value to the experiments.

Sample	λ exp (nm)	Si n	λ (nm) m =1
cs 865	1000	3.61	216.6
cs 864	1000	3.61	216.6
cs 867	565	4.36	261.6
cs 868	628	4.23	253.8
cs 871	616	4.23	253.8
cs 872	-	-	-

a

Sample	λ exp (nm)	Si n	λ (nm) m=0
cs 865	1000	3.61	433.2
cs 864	1000	3.61	433.2
cs 867	565	4.36	523.2
cs 868	628	4.23	507.6
cs 871	616	4.23	507.6
cs 872	-	-	-

b

Table 4.2: Calculated peaks for reflection for destructive a) and constructive b) interference for the samples with thickness 30 nm. Exp stands for experimental. The refractive index of Si is denoted with n. Only a few samples agree with the calculated results.

The calculated peaks for destructive interference in reflection as can be seen in table 4.1 (a) are not in good agreement and therefore cannot be assigned as such. The results for constructive interference on the other hand agree very well, particularly for samples cs 868 871 and 872 (in appendix). In transmission there is very good agreement for the condition of constructive interference for sample cs 867 and it's the best agreement in the entire series. Higher m (1,2, 3…) number provides wavelengths that are further away from the experimental results.

The simulation setup included three monitors to record the behavior of the electric and magnetic fields inside and outside the thin film and the particle, and therefore make their visualization possible. Each monitor is normal to an axis. The following images present the results. Not all the images are

presented since they are very similar and therefore do not contribute to further understanding, instead the most interesting are presented. The z monitor (in xy plane) is placed just above the film and in the middle of the particle.

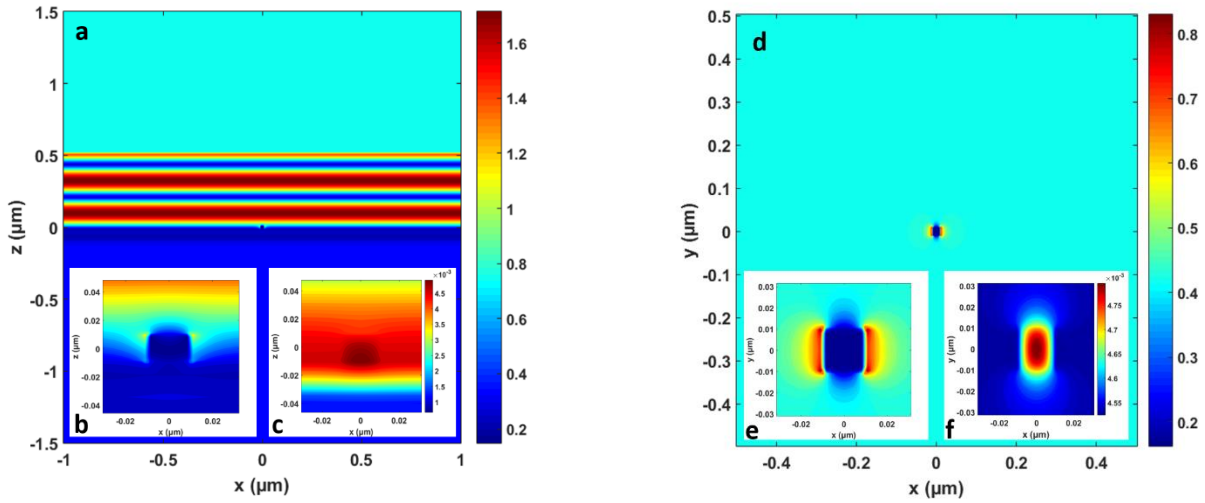

Figure 4.1.8: a) Cross section of the electric field at 450 nm (on the peak) for the 20 nm particle. The monitor is normal to the y axis. The color scale indicates the intensity of the electric field. b) Zoom in to provide more detailed view inside and around the particle. c) Zoom in on the magnetic field for the same wavelength showing maximum intensity inside the particle. d) Cross section of the electric field of the monitor normal to the z axis for the same wavelength. e) Zoom in on the same image showing the lateral scattering at the sides of the particle. f) Zoom in of the magnetic field showing the resonance inside the particle.

Figure 4.1.8a) shows the cross section of the electric field provided from the y-axis normal monitor for 450 nm (on the transmission peak). Initially the image gives the impression that there is nothing

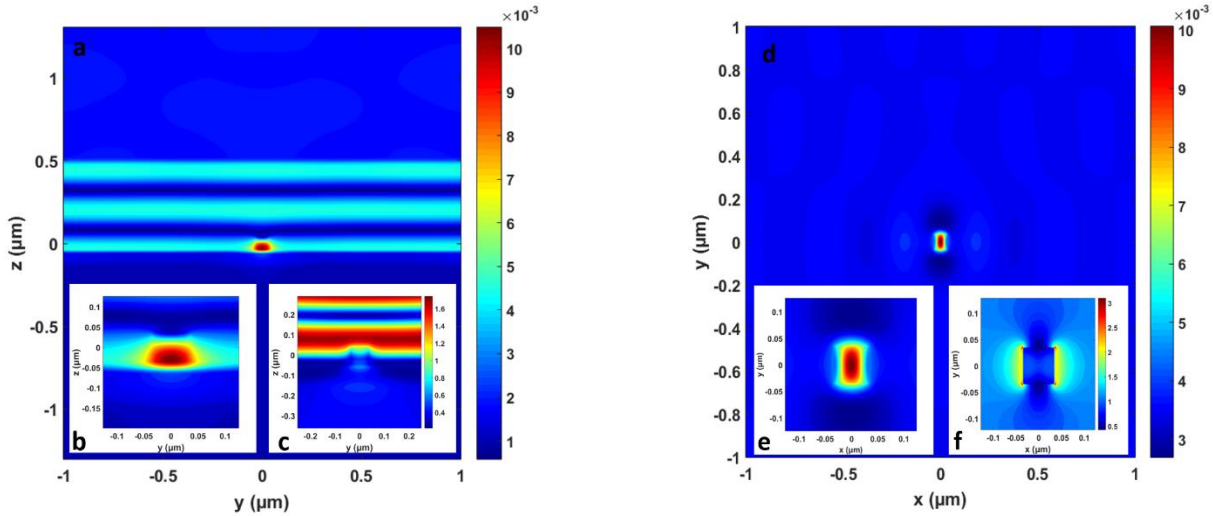

Figure 4.1.9: a) Cross section of the magnetic field at 478 nm (on the peak) for the 70 nm particle. The monitor is normal to the x axis. The color scale indicates the intensity of the field. b) cross section of the magnetic field for the same wavelength, Interference patterns above and below the film can be seen. c) Electric field cross section obtained from the same monitor. d) Magnetic field cross section at 385 nm (on the valley) normal to the z-axis clear interference inside the film and resonance in the particle. e) Zoom in of the precious image. f) Zoom in of the electric field for the same wavelength showing lateral

pareticular happening inside the particle. However looking at the cross section provided by the z monitor in figure 4.1.8d) and e) one can clearly see the lateral scattering of light from the sides of the particle in line with to polarization of the incident light pulse. 4.1.8f) shows the corresponding magnetic field cross section zoomed in. A dipolar resonance inside the particle is visible here. The magnetic field is created by the displacement currents caused by retardation in the electric field. Since those currents are on the surface they are less visible. The magnetic field is more distributed over space and therefore more visible[34] in the cross sections. Figure 4.1.9a) shows the magnetic field of the 70 nm particle at 478 nm (on the transmission peak) where a resonance is present and a zoom in on the particle is provided to show it more clearly (fig. 4.1.9b) The inset c) shows the electric field for the same wavelength with some faint interference patterns above and below the film visible. The interference patterns are very intense at 385 nm (valley in reflection) shown in fig. 4.1.9d) where the magnetic field is shown with a zoom in on the electric field shown in the inset e). The inset 4.1.9 f) shows the electric field obtained from the same monitor and wavelength showing interesting patterns of lateral scattering. Finally, figure 4.1.10 shows cross sections for the 70 nm particle at 867 and 269 nm (off the peak). These wavelengths are far away from the ones for which a peak or valley is observed. The electric field as shown in 4.1.10a) is almost zero inside the particle. On the sides of the particle the intensity is higher due to lateral scattering. (see the zoom in of inset fig.4.1.10b)

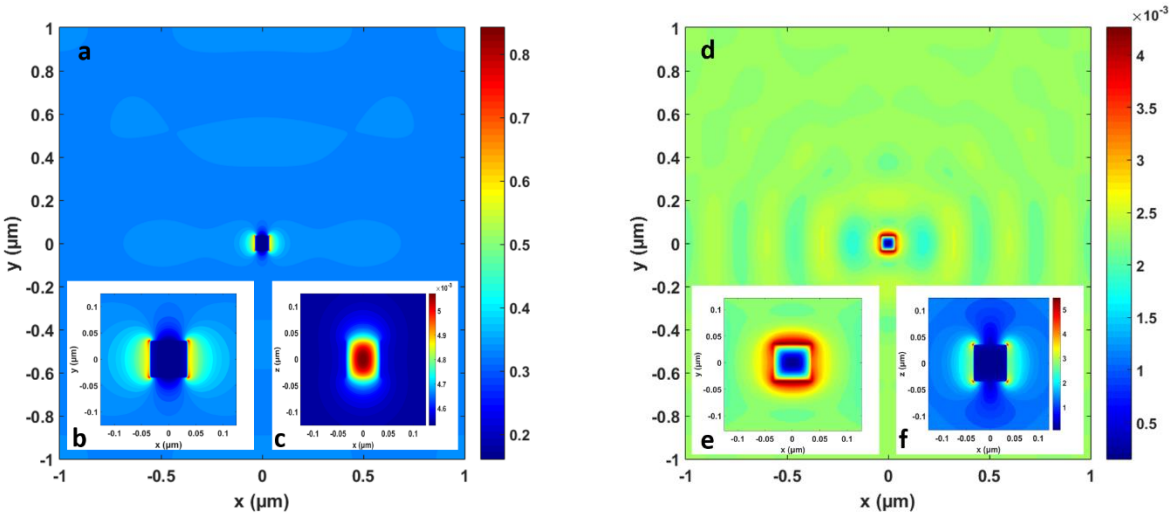

Figure 4.1.10: a) Cross section of the electric field at 867 nm (off peak) for the 70 nm particle. The monitor is normal to the z-axis. The color scale indicates the intensity of the field. b) zoom in for the same wavelength. c) Zoom in for the magnetic field. d)Magnetic field cross section at 269 nm (off peak) normal to the z-axis. e) Zoom-in of the same image. f) Zoom in under the same parameters for the electric field The wavelengths are far from the ones for which peaks or valleys are observed

The zoom in in fig. 4.1.10e) the magnetic field intensity is low inside the particle and very high outside on all sides surrounding it. The magnetic dipole is perpendicular to the electric dipole. The circular patterns appearing on the surface of the film are due to the periodicity of the simulated structure. The inset of figure 4.1.10f) shows the zoom in on the particle for the same wavelength for the electric field. Compared to fig 4.1.10b) where the electric field is high on the entire sides of the particle, here it is only strong at the corners.

General observations for the 30 nm thick film.

It appears that small particles ($\sim 20\ nm$) combined with the thickness of 30 nm Si show a moderate effect for samples 871, 872. This is the case also for cs 867 although the particle size distribution is higher around 50 nm. Cs 865 with its uniform distribution of small and large particles, interestingly shows intense valley in reflection and 864 while very small particles is able to show a very prominent valley in reflection similar to the one observed in cs 865.

The minimum values for samples 865 and 864 appear to be relatively close, especially in transmission. However, the main particle size for cs 864 is quite small (4-8 nm) as compared to the larger ones (30-40 nm) present in cs 865. Cs 864 has fewer particles around ~30 nm. They may be optically more active, as is the case of cs 865. Particles around ~30 nm, sparsely placed and combined with surrounding smaller particles, which are optically less active, might be the reason of the effect. The FWHM here is quite broad ranging from 400 to 800 nm for the transmission measurements

4.2.3 Si thickness: 70 nm

We now proceed to our next series of samples that were made with a thicker film of 70 nm. Six samples were produced, with aggregation lengths of 40 mm and 60 mm with an Ar gas flow of 20 sccm. First the graph showing the dektak measurements for the film thickness is shown followed by the unprocessed optical data of total reflection and transmission for the reference sample. Then we continue with the presentation of the results for each sample separately. Total reflection is shown in fig. 4.2.1 and exhibits a valley at 600 nm (destructive interference) and a maximum at 950 nm (constructive interference). Transmission, shown in fig. 4.2.1. b) starts at zero then it is increasing and maximizes with a clear peak at 650 nm (due to reduced reflection).

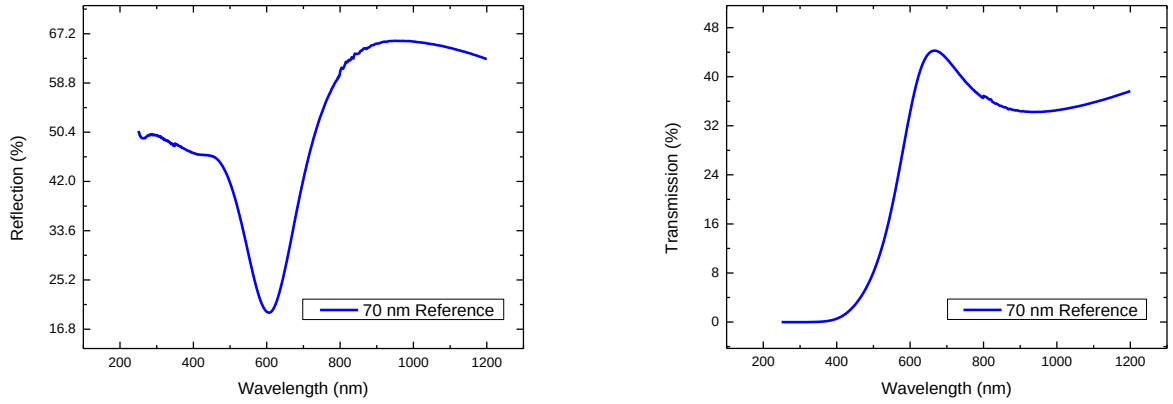

Figure 4.1.1: Raw optical data of total reflection (a) and transmission (b) for the 70 nm thick Si reference sample ss 196. The UV-Vis measurements were performed in the range of 250 nm to 1200 nm.

The first sample in the series is cs 873. The aggregation length was 60 mm, the deposition time 15 minutes and the current was 0.163 A. The optical measurements of total reflection and transmission difference, together with the simulations for different particle sizes can be seen in figure 4.2.1.

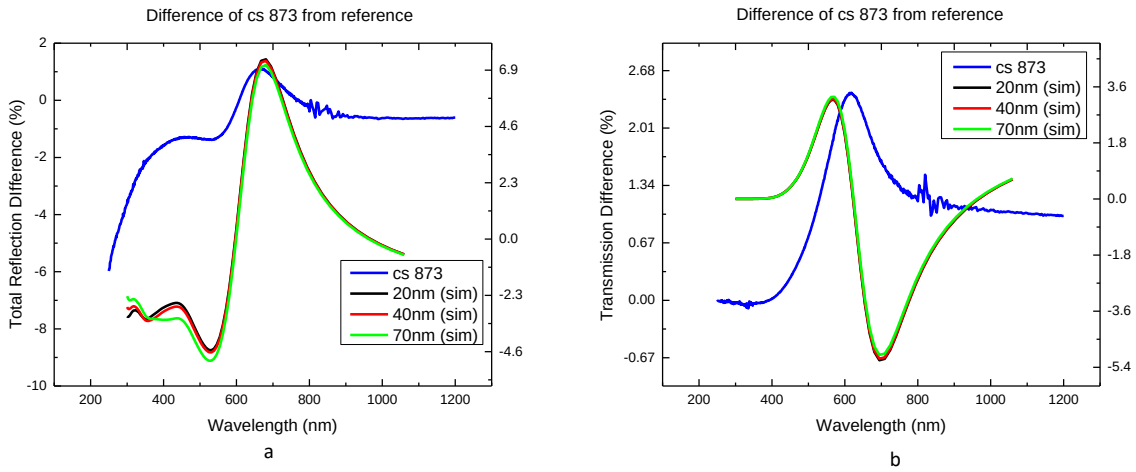

Figure 4.2.2: Total reflection a) and transmission b) difference as a function of wavelength for cs 873. The results of the simulations are represented with the light green, red and black lines. The peak in reflection is at 669 nm and in the transmission is located at 617 nm.

We can observe a peak in total reflection (fig. 4.2.2a), at 669 nm, with corresponding FWHM of 491 nm. The graph has a maximum value of 1.29 %. The simulations predict peaks at 674 nm for all the different sizes, which shows very little size dependence, compared to the thinner film. The behavior of the simulated reflection is somewhat different, showing a far steeper decrease after the peak reaching a minimum at 532 nm followed by a smaller peak at 424 nm. In the experiment, the decrease is slowing down shortly after at 500 nm forming a step at 474 nm, which can be related to the small peak of the simulations. Nevertheless, since the wavelength of the peaks are close we have a relatively good agreement of simulations and experiment.

In the transmission (fig. 4.2.2b), the peak of the experiment is positioned at 617 and has a FWHM of 271 nm. It has maximum value of 2.41 %. The experiments are in good agreement with the simulations, since we can observe peaks at 586 nm for all the sizes, which is very close to the experimental values. There is a slight difference in the overall shape of the graph but this is due to deviations of the Si thickness in the real sample and the simulated. Additionally, the arrangement of the particles in the samples has greater size and distribution variation compared to the perfect symmetry of the simulations.

The difference between processed results of particle samples and raw results of reference sample is clear. There is no valley in total reflection for the particle sample. The peak is located near the position where the valley appears in the reference. The transmission graph, although more similar, still differs considerably regarding the intensity and the position of the peak. In the particle sample the peak is sharper and more distinct and is positioned approximately 40 nm closer to UV.

Figure 4.2.3 shows the graph of the calculated absorption difference including the simulations. We can see the typical high difference in the UV range, here however the decrease is somewhat slower in comparison with the samples of the thinner film (30 nm), perhaps due to the increased thickness of the film.

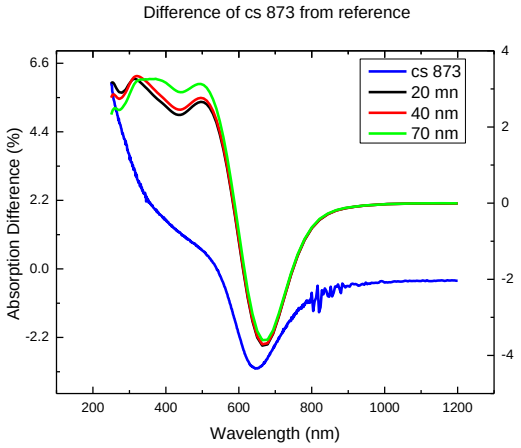

Figure 4.2.3: Absorption difference per particle for cs 873 with simulations. The absorption reaches a minimum negative value of $-3.21\ \%$ at 620 nm. The peaks from the simulations are located at 668 nm.

The absorption becomes negative at 550 nm, reaching a minimum of -3.21 % at 620 nm. In the remaining part of the spectrum it stays close to zero. The simulations behave in a similar manner showing a steeper decrease that reaches the minimum point at 668 nm, which is very close to the experimental values making a good agreement.

The AFM with the histogram of height distribution of particles of the sample are presented in the following picture.

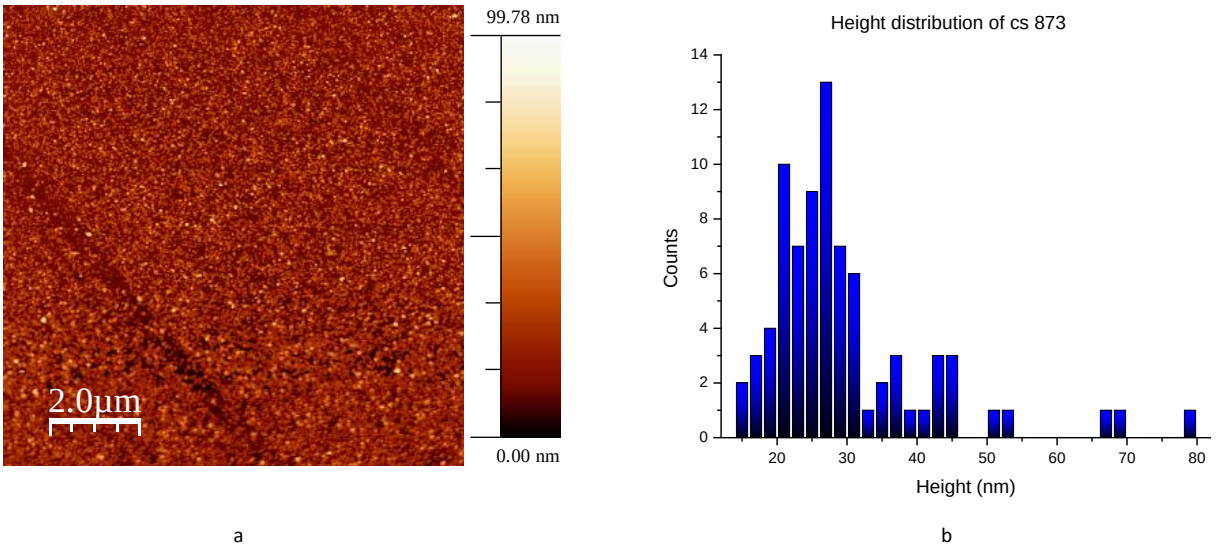

a b

Figure 4.2.4: AFM image a) and a particle height histogram b) for cs 873. Next to the image, the z scale is attached. The scan area is 10x10 µm. The histogram was created by counting particles in a selected square of 1x1 µm. The main particle size is in between 20 nm and 30 nm.

In the AFM image shown in figure 4.2.4 a, we see that the sample is densely populated with particles of dominant sizes that are in the range of 20 nm to 30 nm, creating a uniform distribution. There are also lots of larger clusters in sizes of 40 nm, 50 nm, 70 nm and 80 nm. To create the histogram, we selected a square of 1x1 µm, counted the particles one by one and measured their height. The sample contains a lot the sizes used in the simulations since it includes the three sizes selected (20 nm, 40 nm and 70 nm). This resemblance is further enhanced by the overall good agreement of the experimental results with the simulated ones.

The cluster deposition of cs 874 was performed using a 40 mm aggregation length. The deposition time was 30 min and the power was 54.53 W. The results of the optical measurements are shown in the following figures.

The total reflection (blue line) is plotted in figure 4.2.4a and contains two peaks. The first peak is at 660 nm where the difference is maximized, and the second less sharp peak at 451 nm. Their corresponding values are 2.68 % and-6.69 %. The peaks are relatively narrow with FWHM of 289 nm for the highest and 260 nm for the smaller. Most of the experimental graph lies below zero, with only a narrow set of wavelengths between 618 and 718 nm where the high peak is located, giving positive values. Transmission (blue line) exhibits a sharp peak positioned at 574 nm where the maximum transmission difference is 5.2 %.

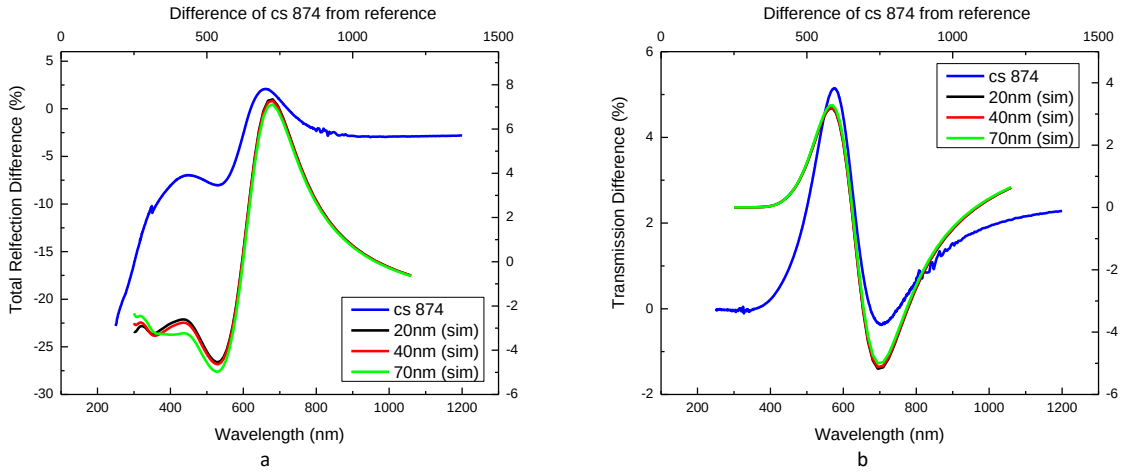

Figure 4.2.6: Total reflection a) and transmission b) difference as a function of wavelength for cs 874. The results of the simulations are represented with the light green, red and black lines. The simulations are in excellent agreement with the experiments. The peaks are located at 660 nm for reflection and at 574 nm for transmission.

The graph starts from zero and is positive for the bigger part of the spectrum, except around the minimum at the region 669 nm to 748 nm where it turns negative.

The simulations show in both reflection and transmission excellent agreement with the experiments. In the results of the total reflection for the simulations, the high peak is at 722 nm, which is slightly shifted from the experimental value. The small peak is even closer at 424 nm. In the transmission the agreement is very good. The simulations predicted a peak at 582 nm and the overall shape of the graph is nearly identical to the experiment. It starts also from zero being constant for a brief period before forming the peak, which is followed by a minimum. The only difference is in the part of the graph (negative), which in this case is for a longer wavelength range from 655 nm to 1079 nm.

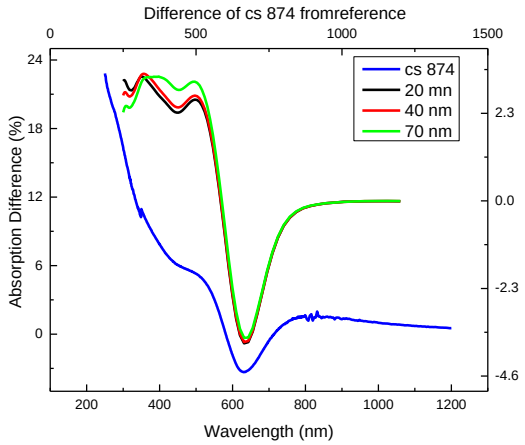

Figure 4.2.7: Absorption difference for cs 874. The blue line corresponds to the difference from the first reference and the green to the difference from the second. The absorption shows a deep at 631 nm reaching a minimum of -3.49 %. The peaks from the simulations are located at 668 nm.

The graph of total reflection for the particle sample, as was the case in sample cs 873 behaves very differently compared to the graph of the raw optical data for the reference since there are now two peaks. In transmission the peak is even more clear and sharp and its even closer to UV about 80 nm.

The absorption difference is plotted in figure 4.24 and is similar to the previous sample showing the same good agreement with simulations for the position of the minimum. It is very high in the UV range starting from its highest value of 22.7 % decreasing gradually until 631 nm where it reaches minimum absorption slightly below zero with a value of -3.49 %. Then for the rest of the spectrum it remains above zero and at 788 nm forms a small hill barely identifiable as a local peak, which gives a difference of 1.6 %. Looking at the histogram in fig. 4.2.6b, we can see that the main particle height is in the range between 22 nm and 50 nm, with maximum counts at 25 nm, 30nm and 45 nm. The image is similar to the previous sample but containing more particles, as the calculated density is 80 particles/μm^2.

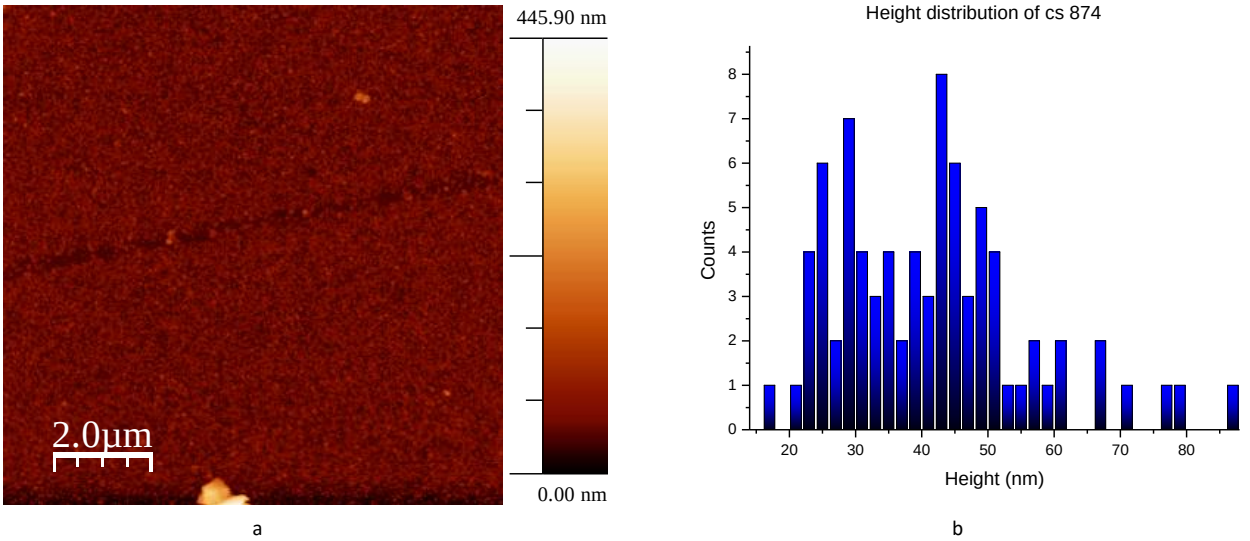

a b

Figure 4.2.8: AFM picture a) and particle height distribution, b) histogram of cs 874. The selected square for counting and measuring the particles was 1x1 µm. The bin size is 2 nm. The particle density of the sample is 80 particles/µm2.

The maximum height encountered is 80 nm. A 1x1 µm square was selected to count the clusters and measure their height. The z scale of the AFM image indicates a maximum height of 445 nm due to a big particle, probably dust that had to be excluded.

Comparison with estimated standing waves

The interference wavelengths corresponding to the peaks observed in the experiments were calculated using the theoretical relation for various integers m. The results are shown together with the experimental peaks for comparison in tables 4.3 and 4.4.

Sample	λ ex (nm)	Si n	λ (nm) m=1
cs 873	669	4.17	583.8
cs 874	660	4.17	583.8
cs 874 2nd	451	4.47	625.8
cs 875	521	4.17	583.8
cs 876	662	4.17	583.8
cs 876 2nd	410	4.38	613.2
cs 877	537	4.17	583.8
cs 878	668	4.17	583.8

a

Sample	λ ex (nm)	Si n	λ (nm) m=1
cs 873	669	4.17	389.2
cs 874	660	4.17	389.2
cs 874 2nd	451	4.47	389.2
cs 875	521	4.17	389.2
cs 876	662	4.17	389.2
cs 876 2nd	410	4.38	408.8
cs 877	537	4.17	389.2
cs 878	668	4.17	389.2

b

Table 4.3: Calculated wavelengths of the peaks of reflection using the condition for destructive a) and constructive b) interference. Ex denotes the experimental peaks, n the refractive index of silicon and 2nd the lower peak in the graph. Only the integer m that gives the closest values to the experiments are chosen.

Sample	λ exp (nm)	Si n	λ (nm) m=1
cs 873	617	4.23	592.2
cs 874	574	4.36	610.4
cs 875	619	4.23	592.2
cs 876	576	4.36	610.4
cs 877	682	4.36	610.4
cs 878	619	4.23	592.2

a

Sample	λ exp (nm)	Si n	λ (nm) m=1
cs 873	617	4.23	394.8
cs 874	574	4.36	406.9
cs 875	619	4.23	394.8
cs 876	576	4.36	406.9
cs 877	682	4.36	406.9
cs 878	619	4.23	394.8

b

Table 4.3: Calculated wavelengths of the peaks of transmission using the condition for destructive a) and constructive b) interference. Exp denotes the experimental peaks and n the refractive index of silicon. Only the integer m that gives the closest values to the experiments is chosen.

Looking through the numbers we can observe that for total reflection the agreement between experimental and calculated peaks is better for the condition of destructive interference. The best agreement in this case is observed for sample cs 875 with 50 nm difference between calculation and experiment. This the case also for transmission peaks. The agreement is better here compared to total reflection were the difference between calculation and experiment is smaller for most samples, with sample cs 873 showing the smallest one.

The cross sections of the simulated electric and magnetic fields are presented in the following figures. Only the results of 40 and 70 nm particle are presented since the 20 nm particle does not provide more information. In figure 4.2.9 a) the electric field at λ = 586 nm (on transmission peak) is shown. The intensity of the electric field is high above the particle and on the upper corners but very low inside it as can be seen in the zoom in (fig 4.2.9b) However the magnetic field shown in the inset fig. 4.2.9c) is very intense inside the particle and the thin film.

Figure 4.2.9d) shows the cross section of magnetic field obtained from the monitor normal to the z axis for the same particle for λ = 723 (on the reflection peak) nm where the peak in reflection occurs. The interference fringes are due to the periodic boundary conditions. In the inset fig. 4.2.9e) the zoom in shows clear resonance inside the particle. The electric field cross section for the same parameters is also provided with zoom in on the particle in fig. 4.2.9f) for comparison.

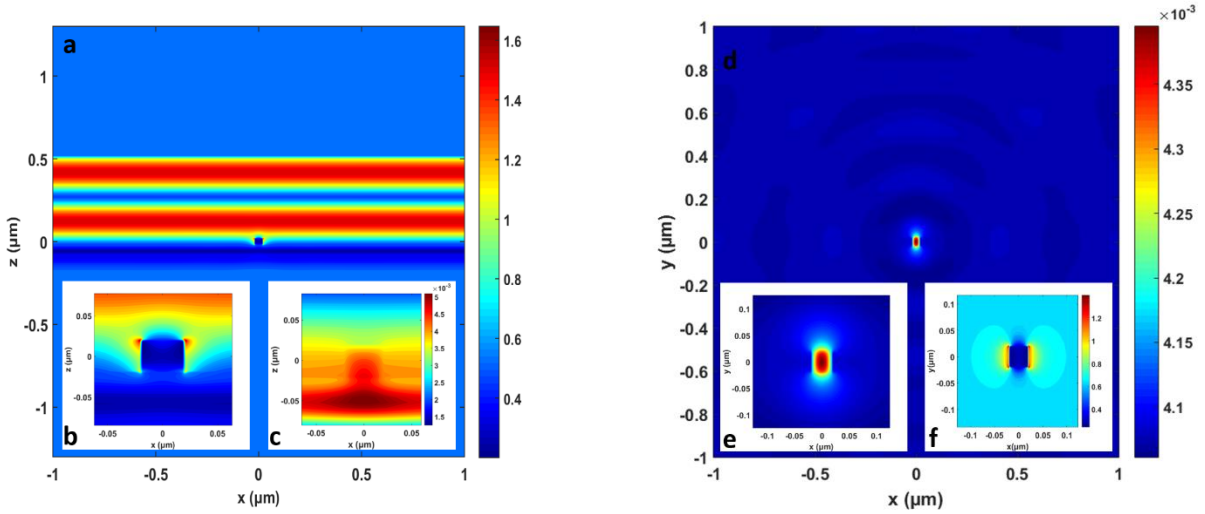

Figure 4.2.9: a) Cross section of the electric field for the 40 nm particle at 586 nm (on the peak). The monitor is normal to the y-axis. The high intensity (red) inside the film indicates constructive interference. b) Zoom in on the same mage showing low filed intensity inside the particle and increased on the upper corners c) Magnetic field Zoom in were the increased field intensity inside the particle is more clear. d) z-axis normal cross section of the magnetic field at 723 nm (on the peak). The ring shaped features indicate constructive and destructive interference similar to a Fabry-Perot etalon. e) zoom in indicating the resonance inside the particle. f) Zoom-in of the electric field where the increased intensity on the left and right side of the particle indicates lateral scattering.

Figure 4.2.10a shows the magnetic field cross section for the 70 nm particle at λ = 586 nm (on the transmission peak) from a monitor normal to the y-axis. The magnetic field in general shows more intense and spatially larger effects than the electric field, hence is chosen for demonstration in most of the cross section pictures.

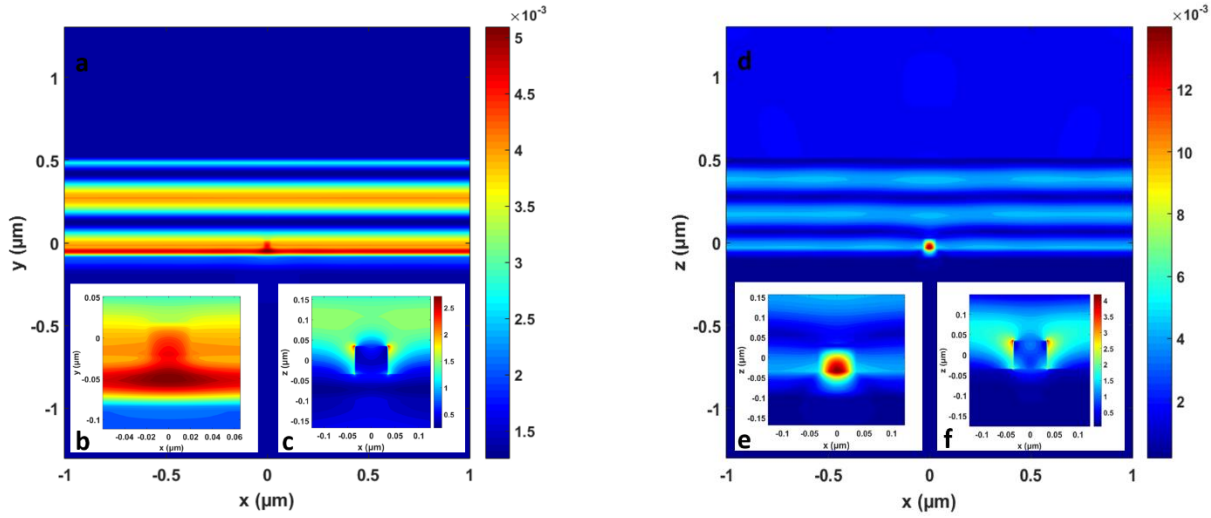

Figure 4.2.10: a) Electric field cross section at 586 nm (on the peak) for the 70 nm particle showing lateral scattering at the upper corners of the particle. c) Magnetic field zoom-in for the same wavelength showing resonance inside the particle and standing way resonances inside the thin film. The monitor is normal to the y-axis. d) Magnetic field cross section for the 70 nm particle at 422 nm (on the peak) obtained from the y-axis normal monitor showing intense resonance in the particle. e) Zoom in on the same image. f) Zoom in on the electric field, lateral scattering at the upper corners is visible.

The field is less intense in the film than in the particle. Inset c) shows the results of the magnetic field obtained from the same monitor. The low peak in reflection at λ = 423 nm (fig. 4.2.20d) is showing high intensity inside the particle and the film. The monitor is normal to the y-axis. The magnetic field here shows the most intense effect in the corresponding wavelengths, therefore it was the main choice for the depiction of the cross sections.

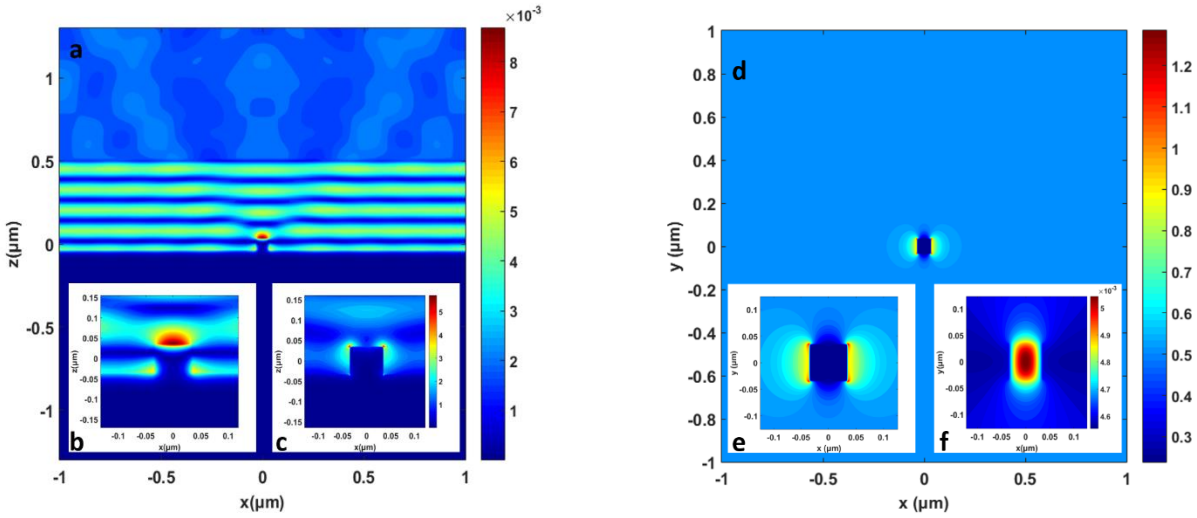

Figure 4.2.11: a) Magnetic field cross section at 250 nm (off peak) for the 70 nm particle obtained from the y axis normal monitor. b) Zoom in showing intensity close to zero inside the particle and high at the top surface and on the sides. c) zoom in from the same monitor on the electric field. d) Electric field at 975 nm (off peak) signs of lateral scattering can be seen on the sides of the particle. The monitor is normal to the z-axis. e) Zoom in on the same image. f) Zoom in on the same monitor for

The inset Figure 4.2.11 a) shows magnetic field cross section at λ=250 nm (off the peak) provided by the monitor that is normal to the y axis. The zoom-in in b) shows high field intensity on top of the particle lower but still intense on the sides and almost zero inside. The second inset c) shows the cross section of the electric field under the same parameters zoomed in on the particle. 4.2.11 d) depicts the clear electric dipole field cross section obtained from the z-axis monitor for the 70 nm particle at λ=975 nm (off the peak). The field intensity is zero inside the particle and higher on the sides due to the dielectric response. The inset figure 4.2.11.f) shows the magnetic field from the same monitor and parameters zoom in on the particle. The two wavelengths selected for the above cross sections are far away from the peaks which are observed in the spectra.

General observations for the 70 nm thick film.

Judging by the two different types of results observed in the AFM images of the samples, they could be separated in two types. First there are samples cs 873, 874, 876 and 878 that are densely populated with clusters that overall range from 20< nm to >80 nm and the second type are cs 875 and cs 877 that have low concentration of particles, which are also lower than 20 nm in height. All samples however are in excellent agreement with the simulations. The wavelength position difference of the experimental results as compared to the simulated peaks, is as low as 7 nm for transmission in the case of cs 876.

4.3 Si thickness: 100 nm

The last series of samples were produced with the thickest Si film of 100 nm. A total of 9 samples were produced. The initial plan was 6 samples as with the previous two thicknesses, however some samples were repeated since they were not of good quality. The cluster source depositions were performed using aggregation lengths of 40 mm and 60 mm with an argon gas flow of 20 sccm. Due to an error in the initial estimation of the film thickness the simulations were performed with 160 nm thick film.

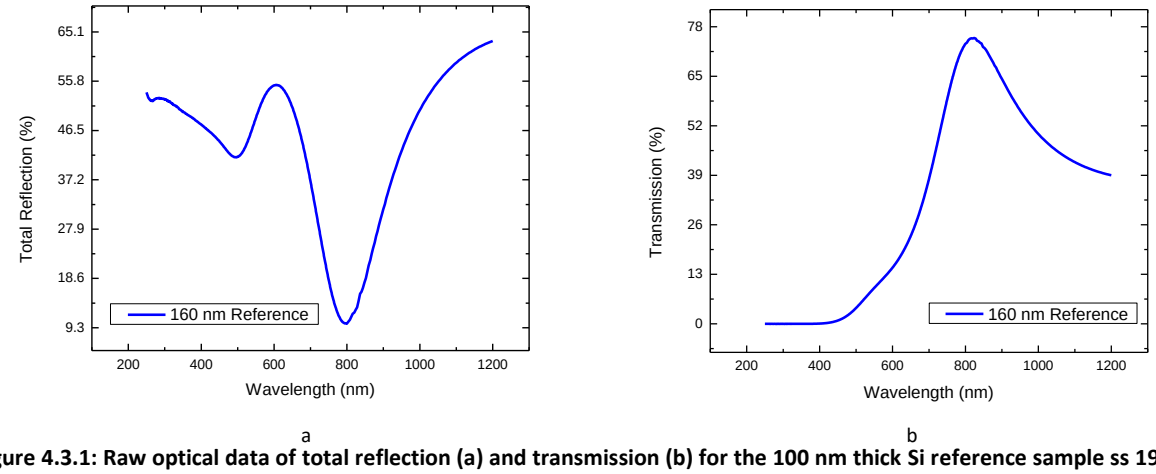

Figure 4.3.1: Raw optical data of total reflection (a) and transmission (b) for the 100 nm thick Si reference sample ss 194. The UV-Vis measurements were performed in the range of 250 nm to 1200 nm.

We start with the presentation of the raw data of total reflection and transmission for the reference sample shown in figure 4.3.1. Total reflection is very different from the previous film thicknesses. As shown in fig. 4.3.1.a, it exhibits a peak at 630 nm and a valley at 790 nm. Transmission is more similar to the 70 nm thick film shows a peak at 820 nm which is 170 nm away towards IR. We proceed with the results for the first sample which is cs 879. We used 40 mm aggregation length and 58.32 W power. The deposition was 30 minutes long. As usual we first show the graphs obtained from the UV-Vis measurements for total reflection and transmission difference

We see in figure 4.3.2a that the total reflection difference exhibits two peaks. The highest peak is located at 877 nm and the lower at 538 nm. If we look at the graph of the reference (fig. 4.3.1a) we can see that after the valley it is increasing and is about to form a peak. The high peak that appears in the difference graph could be interpreted as the completion of the unfinished peak in the reference graph.

The peaks are also present in the simulations where the lower peak is at 543 nm while the higher peak at 735 nm. The lower experimental peak is less prominent in the simulations. The maximum difference in the experimental results is 2.02 %, having corresponding FWHM of 341 nm. The lower peak gives a local maximum value of 0.4 % and a FWHM of 170 nm. Compared to the simulations, the behavior of the experimental graph is very similar having two peaks in both cases and the lower one is positioned at the same point in the spectrum. The agreement is slightly less strong by the shifting of the experimental peak by 142 nm towards the infrared. This is probably caused by a difference in thin film thickness between experiment and simulation.

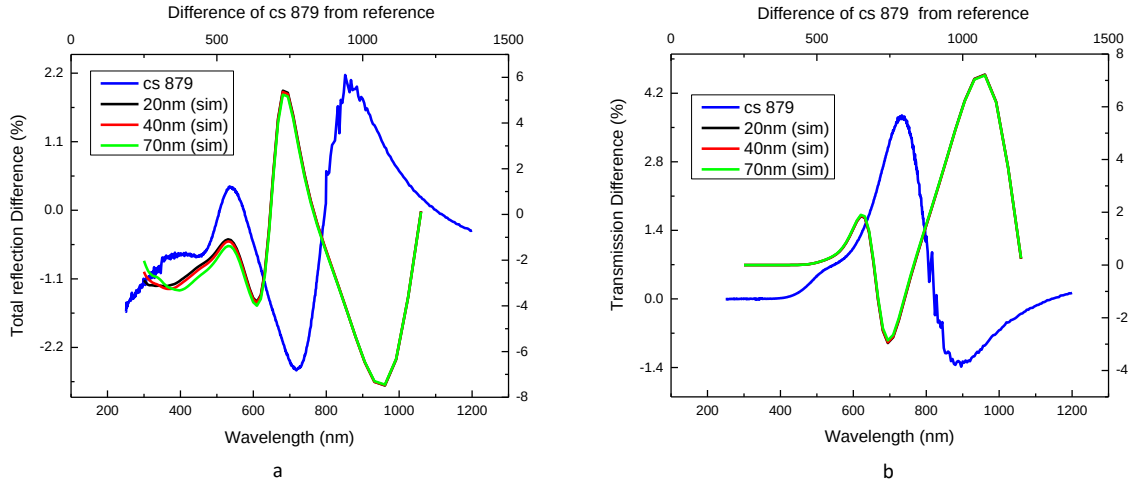

Figure 4.3.2: Total reflection a) and transmission b) difference per particle with simulations. The experimental results are represented by the blue line. The lower peaks of total reflection match the simulations while the higher peaks are shifted 140 nm towards infrared. Transmission shows only one peak positioned at 717 nm 259 nm away compared to the one predicted from simulations. The sign of the experimental results was reversed.

In the transmission a peak appears at 717 nm. The maximum value is 3.82 %, with corresponding FWHM of 175 nm. The simulated peaks are positioned at 1071 nm (high) and 654 nm (low) for all three particle sizes. The lower peak is not present in the experimental results, however If we observe the graph of the transmission more carefully, we will notice a small step at approximately 530 nm. This step is less than 100 nm away from the simulated lower peak at 654 nm, which could be interpreted as a merging of the two predicted peaks in a single one.

Figure 4.3.3 shows the absorption difference starting from high values in the UV range and increases slightly but remains low until 368 nm where it forms a step. The step is followed by the first

valley where the graph is reaching a local minimum value of –0.67 % at 537 nm. The difference is locally maximized showing a peak at 662 nm where it gives a value of 0.42 %.

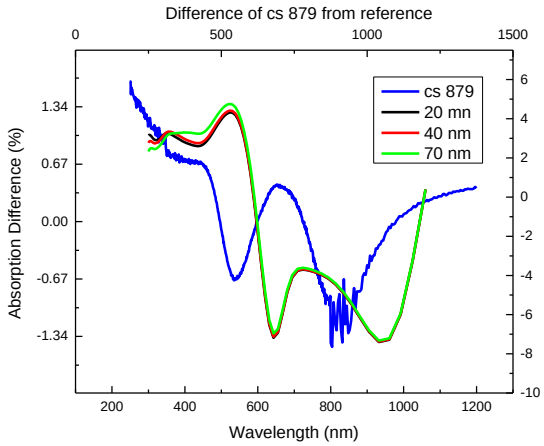

Figure 4.3.3: Absorption difference as a function of wavelength of cs 879. The peak is at 662 nm. The valleys are located at 531 nm (shallower) and 833 nm (deeper) were the difference is -0.67 % and -0.99 %, respectively. The peaks of the simulations are detected at 539 (greater) nm and 807 (smaller).

A second valley follows where the graph is minimized giving a value of -0.99 %. In general, the graph is positive, except around the valleys and more precisely in the intervals 495 nm to 595 nm and 723 nm to 973 nm.

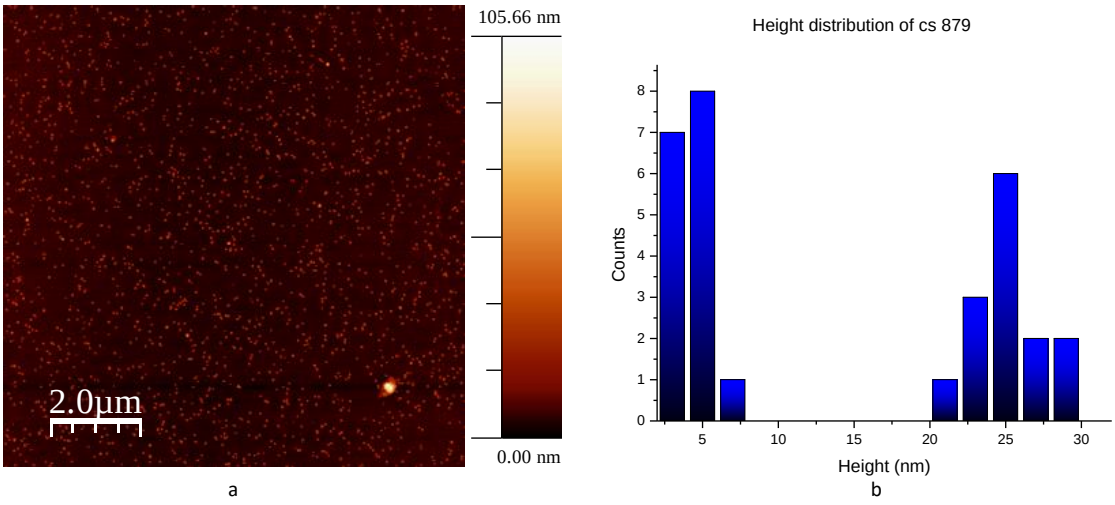

Figure 4.3.4: AFM image a) and particle height distribution histogram b) of cs 879. The distribution is quite uneven showing big amounts of particles between 3 and 5 nm and a smaller population that ranges from 20 to 30 nm. The selected square for the counting of the particles was 1x1 µm. The particles are relatively dense.

Figure 4.3.4a shows the image taken with the AFM microscope taken in a 10x10μm scan area. The z color scale goes up to 105 nm due to one very large particle appearing in the lower right part of the image. The rest of the particles as we can see in the histogram are in separated in two ranges. One

between 3 nm and 7 nm, and one between 20 nm and 30 nm. The dominant particle heights are 3 nm 5 nm and 25 nm. The density is 30 particles/μm^2.

The next sample is cs 883 produced with a 60 mm aggregation length, using a power of 58.82 W. The cluster deposition was 30 minutes long. The result was a sample that contains particles in a height range of 20 nm to 30 nm. In figure 4.3.7a we see the experimental measurements for the total reflection difference. The graph now is very different from what we have seen so far for this series of samples. The graph has mostly negative values except for the point where it forms a small peak at 723 nm, in a maximum of 0.94 %.

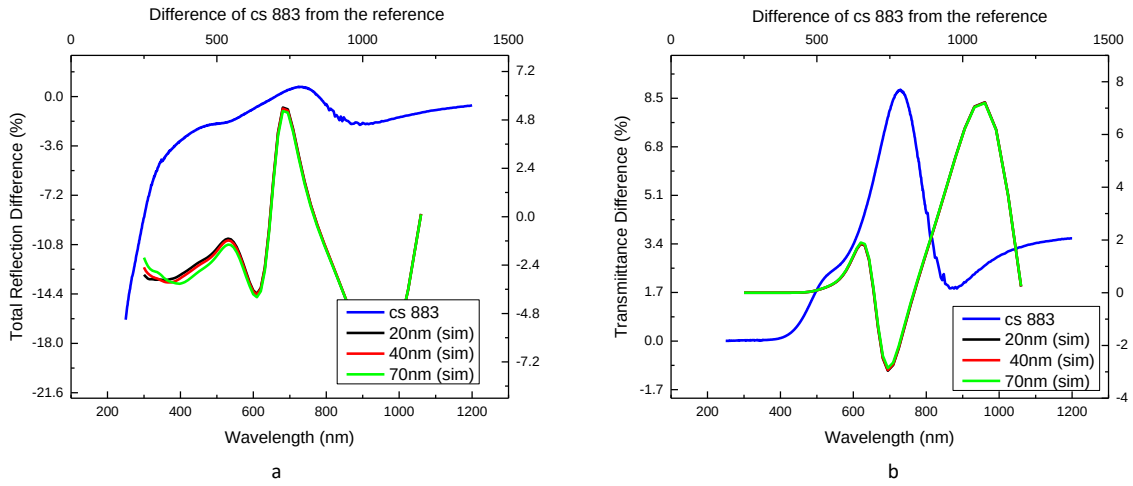

Figure 4.3.5: Total reflection (a) and transmission (b) difference as a function of wavelength. The blue line corresponds to the experiments while the green, red and black to the simulations for each particle size.

This means that the reference is more reflective than the sample with TiO_2 particles. From the simulations we can see that they agree, in the sense that the peak observed in the experiments is almost at the same position at 723 nm. However, we see that the simulations predict two peaks and the higher peak is very sharp, which makes the agreement somewhat less probably due to film thickness differences.

The transmission difference graph behaves very similarly with that of the first sample in the series (cs 879). In fig. 345 b we can see that there is only one peak present, contrary to the two peaks observed

in the simulations. The peak is located at 729 nm giving a maximum of 8.81 %. It is positive for the entire spectrum, indicating enhanced transmission for the sample. In the UV range the transmission reaches zero due to absorption from the glass as we will see in figure 4.3.8 where the absorption difference is shown. A minimum is reached at 725 nm where the absorption is -9.73 % and afterwards a small peak at 870 nm. The difference is negative for the most part of the graph, starting from 505 nm and remaining negative till the end, which indicates that the reference is absorbing more light than the sample. This suggests that the TiO_2 particles enhance optical transmission, which is interesting from a light management point of view.

Figure 4.3.6 depicts the absorption difference. The graph starts from its highest value at 250 nm and decreases forming a valley at 733 nm where it is minimized giving a value of -9.72 %. A local maximum is reached at 885 nm where the difference is 0.16 %. This maximum is 110 nm away towards infrared from the one predicted in the simulations. Overall, the experimental results of the absorption show a fair agreement with the simulations mainly in terms of the behavior of the graph. The positions of the valleys and peaks are somewhat shifted.

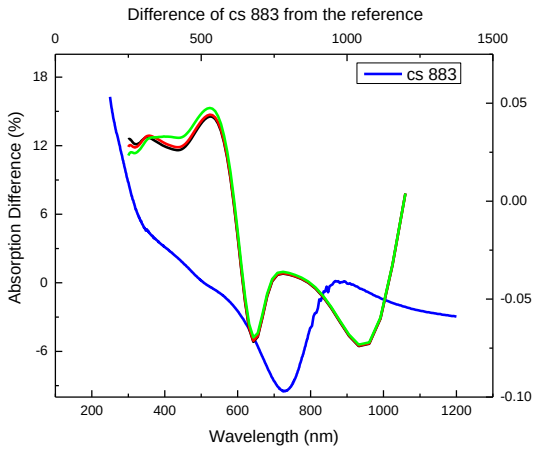

Figure 4.3.6: Absorption difference as a function of wavelength for cs 883. The difference is minimized at 725 nm. The peaks of the simulations are detected at 539 (greater) nm and 807 (smaller). The simulation minima are located at 677 nm and at 1062 nm.

The AFM image and particle distribution histogram are shown in figure 4.3.7. At a first glance we will observe that clusters are greater than 15 nm in height. Since the particles are relatively sparse, we selected a 2x2 μm area to count the particles and create the histogram. The result was a low particle density of 11.47 particles/μm^2. The height range between 20 and 27 nm is the one that the most particles are encountered. The smallest height measured is 15 nm and the largest is 38 nm.

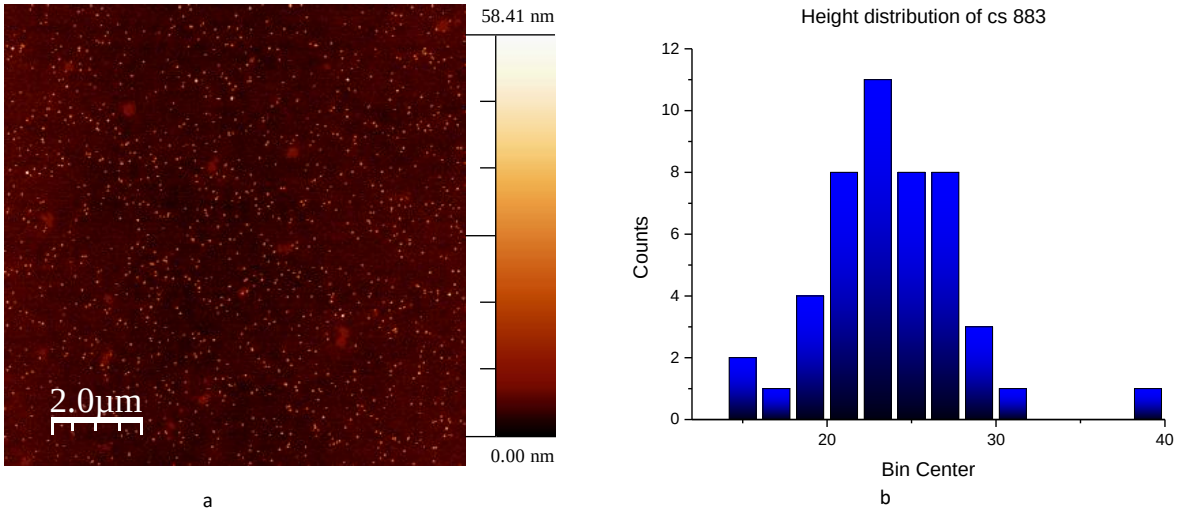

a b

Figure 4.3.7: AFM image (a) and particle height distribution (b) for cs 883. The bin size is 2 nm. The particles are mainly between 20 nm and 27 nm in height. The minimum height is 15 nm and the maximum is 38 nm, that is in the area selected for counting. The z scale shows a maximum height of 58 nm which is one particle in the entire scan.

The wavelengths corresponding to the peaks in experiments were calculated theoretically. The results are shown in table 4.5 and 4.6.

Sample	λ (nm) Exp	Si n	λ (nm) m=1	λ (nm) m=2
cs 879	717	4.01	802	401
cs 880	723	4.01	802	401
cs 880 2nd	535	4.46	892	446
cs 881	867	3.77	754	377
cs 881 2nd	532	4.46	892	446
cs 883	723	4.01	802	401
cs 884	746	4.01	802	401
cs 886(1,2)	784	3.93	786	393
cs 886(3,4,5)	803	3.86	772	386
cs 886(3.4.5) 2nd	394	4.17	834	417
cs 887	729	4.01	802	401
cs 887 2nd	465	4.49	898	449
cs 888	867	4.01	802	401

a

Sample	λ (nm) Exp	Si n	λ (nm) m=1	λ (nm) m=2
cs 879	717	4.01	502.6667	301.6
cs 880	723	4.01	594.6667	356.8
cs 880 2nd	535	4.46	594.6667	356.8
cs 881	867	4.01	534.6667	320.8
cs 883	723	4.01	534.6667	320.8
cs 884	746	4.01	594.6667	356.8
cs 886(1,2)	784	3.93	594.6667	356.8
cs 886(3,4,5)	803	3.86	502.6667	301.6
cs 886(3.4.5) 2nd	394	4.17	502.6667	301.6
cs 887	729	4.01	594.6667	356.8
cs 887 2nd	465	4.49	594.6667	356.8
cs 888	867	4.01	534.6667	320.8

b

Table 4.5: Calculated peaks for reflection using the condition for destructive a) and constructive b) interference formula for two integers m. Exp denotes the experimental peaks 2nd denotes the lower peak in the graph.

Sample	λ (nm) Exp	Si n	λ (nm) m=2	λ (nm) m=3
cs 879	886	3.77	754	377
cs 880	884	3.77	754	377
cs 880 2nd	558	4.01	802	401
cs 881	725	3.77	754	377
cs 883	729	4.01	802	401
cs 884	684	3.86	772	386
cs 886	672	4.09	818	409
cs 887	912	3.77	754	377
cs 887 2nd	558	4.36	872	436
cs 888	733	3.77	754	377

a

Sample	λ (nm) Exp	Si n	λ (nm) m=1	λ (nm) m=2
cs 879	886	3.77	534.6667	320.8
cs 880	884	3.77	594.6667	356.8
cs 880 2nd	558	4.01	534.6667	320.8
cs 881	725	3.77	534.6667	320.8
cs 883	729	4.01	524	314.4
cs 884	684	3.86	534.6667	320.8
cs 886	672	4.09	556	333.6
cs 887	912	3.77	545.3333	327.2
cs 887 2nd	558	4.36	502.6667	301.6
cs 888	733	3.77	581.3333	348.8

b

Table 4.6: Calculated peaks for transmission using the condition for destructive a) and constructive b) interference formula for two integers m in comparison with experimental peaks. 2nd denotes the lower peak in the graph.

The theoretical peaks were calculated for 2 integers m (1,2,3…) because in specific cases there is a fairly good match for either of them. The peaks that agree well with the experiments are highlighted with green. The condition for destructive interference for total reflection shown in table 4.5 a) yielded results that are overall shifted by 50 nm to 100 nm towards UV. The shift is greater for the condition of constructive interference for reflection as well as fordestructive interference for transmission, up to 300 nm for most cases with only two good matches for the second smaller experimental peaks. The best overall agreement is met for the condition of destructive interference for reflection and destructive interference for transmission, shown in tables 4.5 a) and 4.6 a) respectively.

The cross sections of the electric and magnetic field are presented in the following pictures. As before only the most important pictures were selected since there are common features in most of the images making the choice mandatory. Figures 4.3.8 a) and b) (zoom in on the particle) depict the cross section of the electric field at λ=1071 nm (on the high peak of transmission). Once again the field intensity is high above the particle and on its upper corners. The magnetic field for the same wavelength is shown in the inset figure 4.3.8c) were the zoom in on the particle shows that the intensity is maximized inside the particle and is also very high outside of it extending on the lef and right side. The intensity is also high inside the film. In figure 4.3.8d) we can see the magnetic field cross section obtained from z-normal

monitor for the 20 nm particle at 1071 nm (on the transmission high peak). The features are very interesting showing intense lateral scattering in two directions. The zoom in image (fig.4.3.8.e) shows that the field is very intense inside the particle showing clear resonance and on top of the film interference is clearly visible.

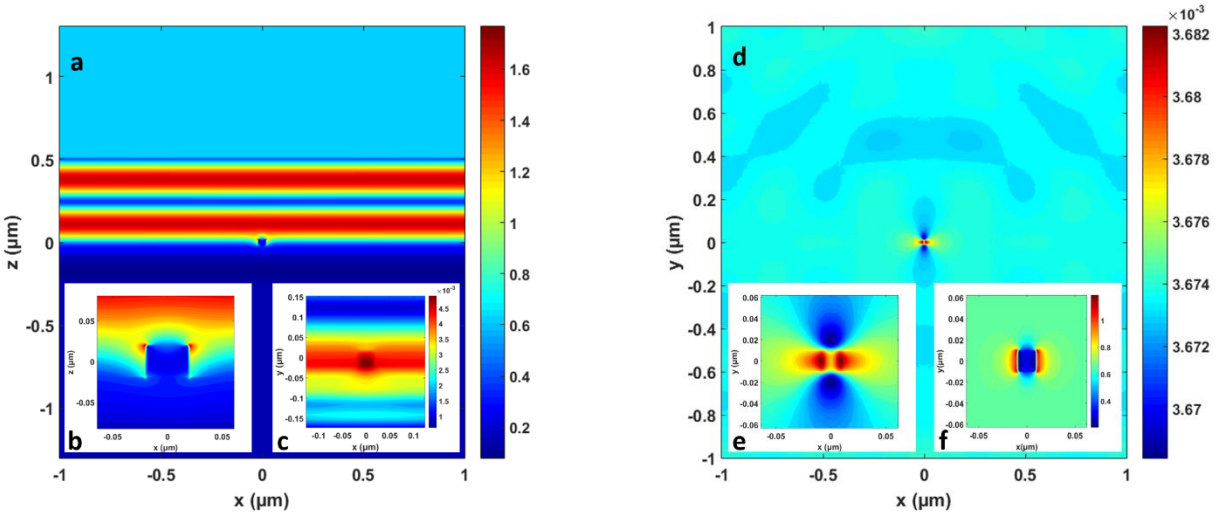

Figure 4.3.8: a) Cross section of the electric field for the 20 nm particle at 1071 nm (on the peak). The monitor is normal to the z axis. The color scale indicates the field intensity. There are visible interference patterns. b) Zoom-in showing the low intensity of the field inside the particle. c) zoom in on the same cross section for the magnetic field showing the resonance inside the particle as well lateral scattering of light at the sides. d) Magnetic field cross section for the 40 nm particle at 537 nm (on the peak) obtained from the z-axis normal monitor. e) zoom in showing intense magnetic field above the particle and lateral scattering. f) Zoom in of the cross section of the electric field from the same monitor

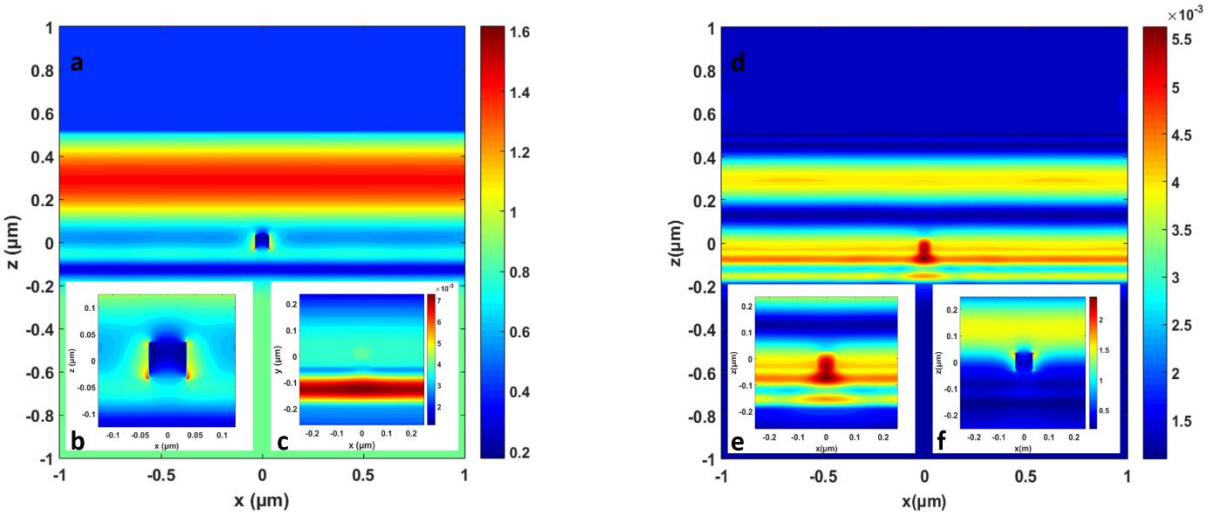

Figure 4.3.9: a) Cross section of the electric field for the 70 nm particle at 1071 nm (on the peak). The monitor is normal to the y axis. The color scale indicates the field intensity. Interference can be seen inside the film (blue stripe below the particle). b) Zoom in of the cross section of a). c) Zoom in for the magnetic field from the same monitor. The magnetic field is more intense A faint resonance can be seen inside the particle. d) Magnetic field cross section for the same particle taken from the monitor normal to the x axis at 654 nm (transmission low peak) Resonances are clearly visible inside the particle and the thin film. e) Zoom in of the previous cross section. f) Electric field cross section on the same parameters zoom in on the particle.

Figure 4.3.9a) depicts the electric field cross section at 1071 nm (on transmission high peak) with a zoom in on the particle shown in 4.3.9b) where it can be seen that the field is intense only on the lower corners of the particle. Inside the film the electric field appears more intense compared to previous images. The inset fiure 4.3.9c) shows the magnetic field from the same monitor zoomed in. Interestingly the field intensity is maximum inside the film while in the particle is lower. A faint circular feature can be detected inside the particle where the field is moderately high.

Figure 4.3.9d) shows the magnetic field obtained from the y-axis monitor. The resonances inside the film and the particle are well defined as seen in the zoom-in (4.3.9e). The inset figure 4.3.9f) shows the electric field from the same monitor zoom in on the particle where the intesity is close to zero inside. In the figures below the electric and magnetic fields for the reference are depicted for comparison with the samples. The high eletric field above the film demonstrates high reflectivity while the high magnetic field strength inside the film confirms the presence of dielectric displacement currents within the thin film.

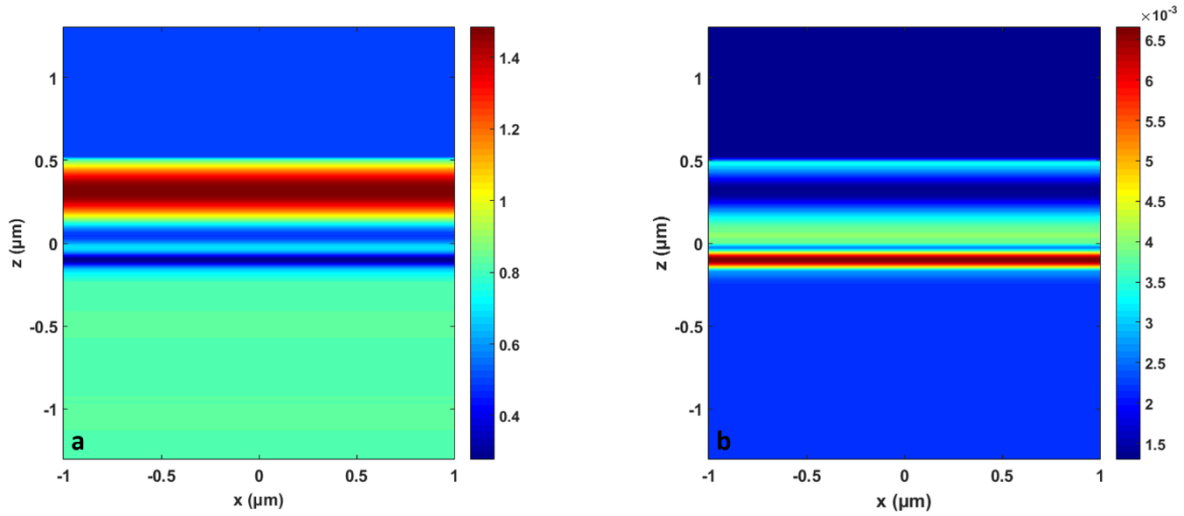

Figure 4.3.10: a) Electric field cross section for the reference at 1071 nm on the peak. b) Magnetic field cross section at 1071 nm. The monitor is normal to the y axis as in figure 4.3.27. The color scale indicates the field intensity.

General observations for the 100 nm thick film.

First of all, the spectra are more complicated by the multiple features due to the possibility of different resonance conditions. Transmission for samples 879, 880, 881, 884 and 888 exhibit peaks in the range 830nm to 890 nm. Samples 883 and 886 show peak at 670-730 nm. CS 887 peaks at 912 and 558 for high and low peak respectively, while cs 880 peaks at 884 and 560 for high and low peak respectively.

Reflection for all samples except 881 and 886(3,4,5) have peaks in the range 710-790 nm. Samples 881 and 886(3,4,5) (different set of measurements for reflection) deviate slightly exhibiting peaks at 870 nm and 803 nm respectively. The samples 880, 881, 886 and 887 exhibit additional lower peaks. Sample cs 880 and 881 at ~530 nm, cs 886(3,4,5) at ~390 nm and cs 887at 465 nm.

It appears that samples 879, 881 and 883 share some common overall features. Although all three have similar particle distributions (low density), their deviations might be related to the individual characteristics in distribution, i.e. whether there are more clusters of 20-30 nm size or more of 10 nm and below. A deviation in thin film thickness may also affect the results.

Samples 884, 886 and 887 have a very high particle density and large particles >40 nm. 886 has two sets of measurements for reflection and in the second one we can see two clear peaks. The first looks similar to the other samples and maybe there is a subtle second peak as well, not easily distinguishable. The agreement with the simulations here is good. In some cases, were the peak in the experiment appears as valley in the simulations and vice versa as mentioned earlier is possibly indicating a merging of two individual peaks. This difference in behavior is due to the fact that the film is not the same thickness in the experiment as in the simulations.

In the next figure a summary of the best graphs of all three Si film thicknesses is shown. The criteria for the choice is the agreement with the simulations in terms of plot shape and peak position and the intensity of the peak. Each row corresponds to a film thickness with increasing order from top to bottom. As the film thickness increases the resonances become more intense. The graph of total reflection for the 70 nm film exhibits an additional smaller peak which becomes more pronounced in the 160 nm film indicating that the thicker films can support more than one resonances. This also accounts for transmission where in the 160 nm film the simulations predict two peaks which appear to be merging in

the experiments as evident by the small protrusion at 520 nm which is not present in the graph of 70 nm film. Absorption exhibits valleys, which as in the case of reflection and transmission are more pronounced as the film thickness increases. Moreover, a peak is present in the graph for the 160 nm film. The agreement of simulations and experiment is overall good and the best agreement can be seen in the graphs for the 70 nm film.

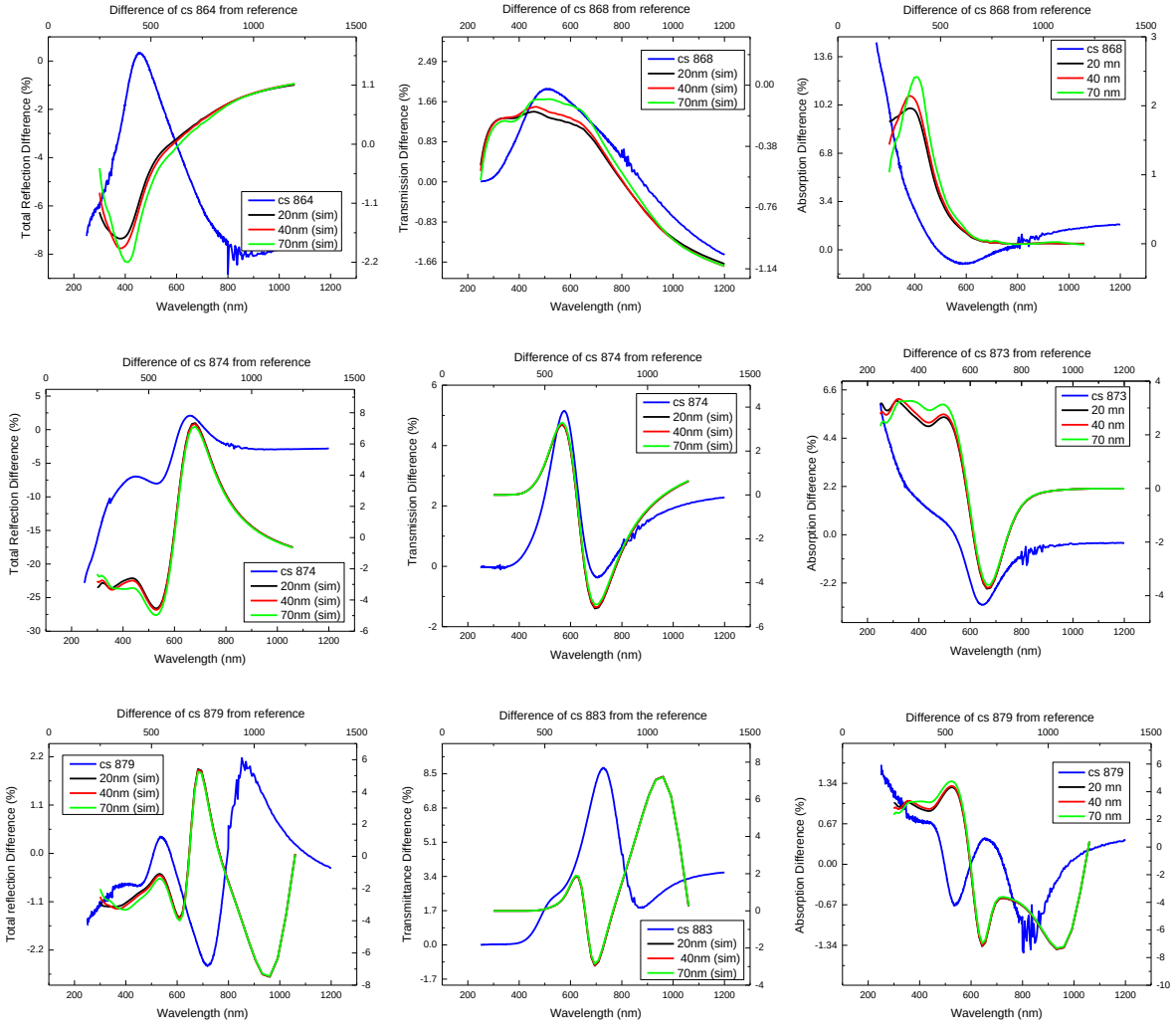

Summary of the best graphs for all three thicknesses of Si films. Each column corresponds to total reflection, transmission and absorption respectively from left to right. Each row corresponds to Si thickness in increasing order from top to bottom.

4.4 TiO_2 nanoparticles deposited on Si_3N_4 thin film

The same procedure was followed for the samples that contained TiO_2 clusters on silicon nitride (Si_3N_4) thin film, on a glass substrate. Three different film thicknesses were selected: 37 nm, 86 nm and 136 nm which is shown in the appendix due to inadequate results. These thicknesses were calculated to obtain resonances for the 300 nm 500 and 700 nm wavelengths. Two samples were made for each thickness with aggregation lengths of 20 mm and 40 mm. The results of the optical measurements are presented for each sample followed by the AFM picture and histogram of height distribution.

Si_3N_4 thickness: 37 nm

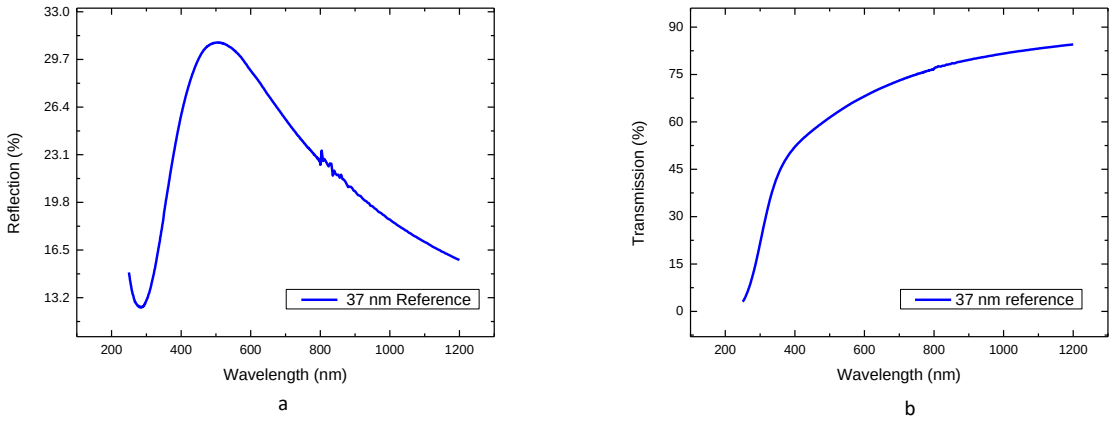

Figure 4.4.1: Total reflection a) and transmission b) optical measurements for the reference sample. The measurements are unprocessed. The wavelength ranges from 250 nm to 1200 nm.

Figure 4.4.1 depicts the unprocessed optical measurement data of total reflection and transmission for the reference sample. The maximum in total reflection is at 500 nm and the minimum at 285 nm. The graph of transmission does not show any extremes it is increasing fast from 250 nm to 400 nm and then more slowly until the end of the spectral range.

The first sample is cs 811. The aggregation length was 20 mm and the deposition time 10 minutes. The Ar gas flow was 15 sccm and oxygen (O) was additionally used with a gas flow of 1 sccm. The power was 61 W.

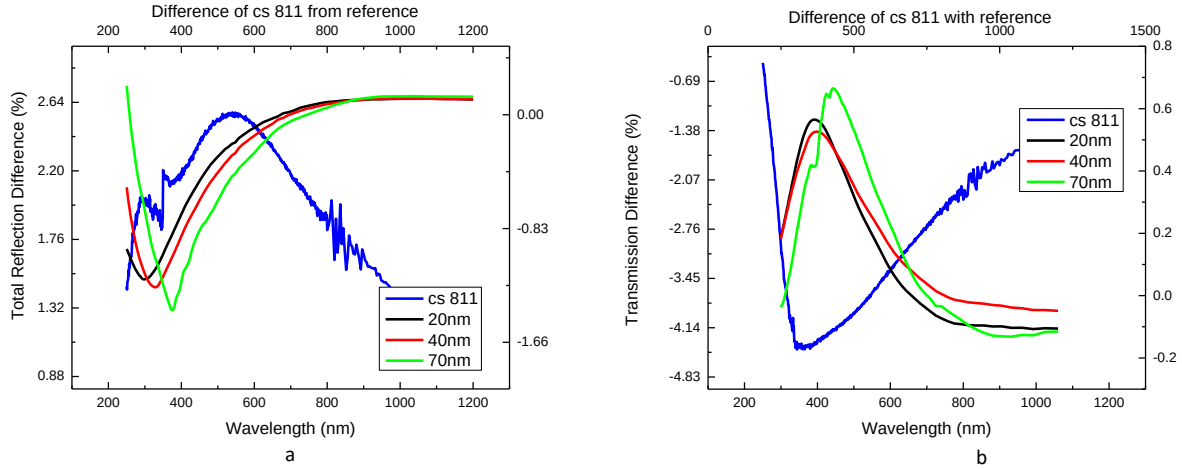

Figure 4.4.2: Total reflection a) and transmission b) difference per particle of cs 811. The blue lines represent the experiments and the green, red and the green, red and black lines the simulations for different particle sizes.

Figure 4.4.2a shows the total experimental and simulated reflection difference. The experimental graph resembles a parabola and exhibits a maximum at 558 nm where the difference is maximized giving 2.58 %. The position and shape resemble the raw total reflection of the reference sample. The FWHM is 202 nm. The difference is positive for the entire spectral range. In the simulations though we observe a different behaviour. Minima can be seen at around 300 nm , then there is smooth increase in a parabolic shape where it maximizes at 970 nm and then stabilizes for the rest of the spectrum. In transmission (fig. 4.4.2b) the values are negative for the most part of the spectral range. There is no visible peak. A valley instead is indicating a minimum at 360 nm where the difference is 0.67 %. The simulations are included and in total reflection difference where contrary ot the experiments there are peaks observed, that differ slightly in position for each particle. The peak shifts towards infrared as the particle size increases. The 20 nm particle (black line) shows maximum at 298 nm, the 40 nm particle (red line) at 326 nm and the 70 nm particle at 373 nm. It is remarkable that the agreement between experiment and simuation is much better when the experimental graph is inversed. This is likely caused by experimental error and could be corrected.

In figure 4.4.3 the absorption difference of cs 811 is shown. The peak of the graph is at 365 nm and is relatively broadened, basically consisting of the entire graph. The maximum value is 2.33 %. Contrary to what we have seen in most of the Si samples, here the difference starts from the lowest value at 250 nm and is increasing extremely fast until its maximum point.

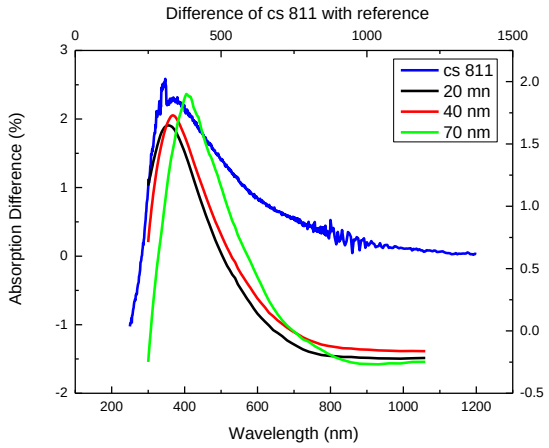

Figure 4.4.3: Absorption difference per particle of sample cs 811 with simulations. The peak is located at 365 nm where the difference is maximized giving a value of 2.33 %. The simulation peaks are located at 353 nm, 364 nm and 407 nm for the 20 nm (black), 40 nm (red) and 70 nm (green) particle respectively.

At approximately 800 nm it becomes negative again. The simulated absorption exhibits peaks that vary with particle size. The absorption for the 20 nm particle maximizes at 353 nm, for the 40 nm particle at 364 nm and for the 70 nm particle at 407 nm, making a good agreement with the experimental results.

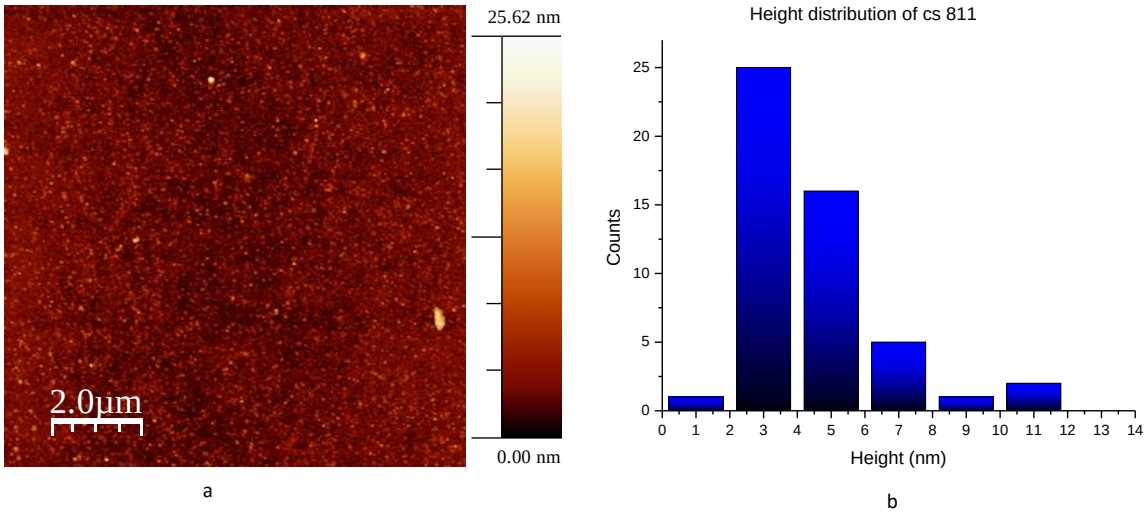

Figure 4.4.4.: AFM scan image a) and particle height distribution histogram b) for cs 811. A 1x1 µm square was selected to count the particles and create the histogram. The particles are very small going at most just above 11 nm.

The sample contains lots of clusters small in size. As we see in the histogram the particles range from 1 to 11 nm, with the most encountered height being 3 nm. The z color scale attached next to the image indicates a maximum height of 25 nm due to overly big particles present in the scan, usually not more than two or three, that are excluded from the counting. The square selected for counting was 1x1 μm. The AFM image (fig. 4.4.4a) shows a uniform layer with surface density 50 particles/μm^2.

The peaks of total reflection and transmission were calculated as before using the theoritical conditions for constructive and destructive interference. The results are presented in tables 4.7 and 4.8. The shape of the graphs indicates that there is no Fano resonance, therefore there is no standing wave in agreement with the film thickness and optical wavelength range.

Sample	λ (nm) Exp	SiN n	λ (nm) m=1
811	505	2.7125	200.72
827	516	2.7125	200.72

a

Sample	λ (nm)	SiN n	λ (nm)
	Exp		m=0
811	558	2.675	395.9
827	592	2.64	390.7

b

Table 4.7: Calculated peaks for reflection using the condition for destructive a) and constructive b) interference formula for two integers m. Exp denotes the experimental peaks 2nd denotes the lower peak in the graph. The peaks were calculated for various integers m, but only the ones that gave the closest result to the experimental are chosen.

Sample	λ (nm) Exp	SiN n	λ (nm) m=1
811	558	2.675	197.95
827	592	2.64	195.36

a

Sample	λ (nm)	SiN n	λ (nm)
	Exp		m=0
811	505	2.7125	401.45
827	516	2.7125	401.45

b

Table 4.8: Calculated peaks for transmission using the condition for destructive a) and constructive b) interference formula for two integers m. Exp denotes the experimental peaks 2nd denotes the lower peak in the graph. The peaks were calculated for various integers m, but only the ones that gave the closest result to the experimental are chosen.

It is evident that the agreement of calculated and experimental peaks is not good. The best agreement is met for the condition of constructive interference for transmission where the calculated peaks are about 100 nm away towards UV. This is the least deviation from the experiments in this series.

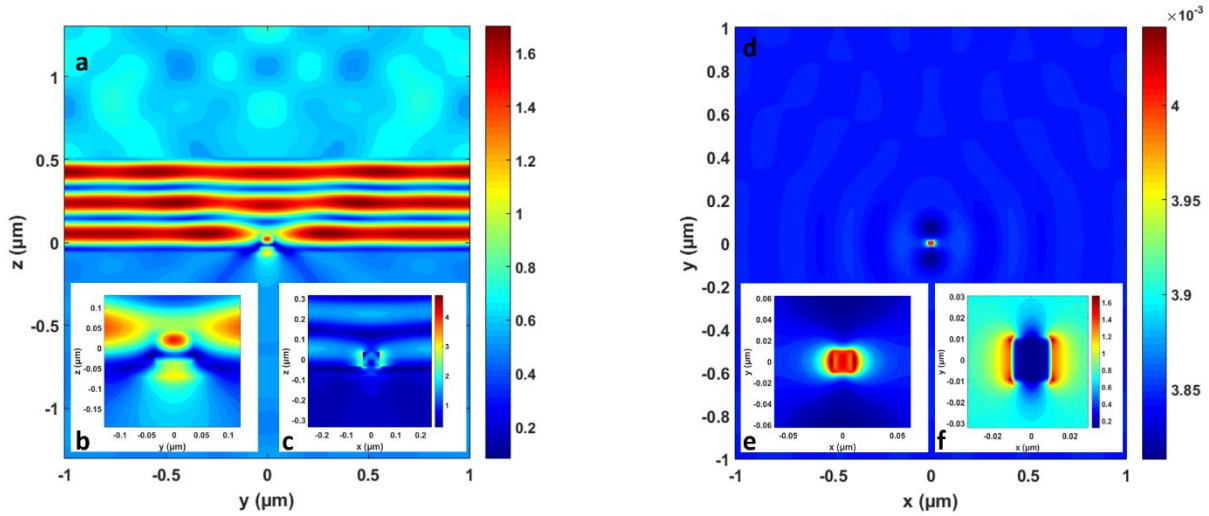

Figure 4.4.5: a) Cross section of the electric field for the 70 nm particle at 373 nm (on the valley), showing resonance inside the film and intense transmission. b) Zoom in on the same cross section were resonance inside the particle is visible and intense transmission. The monitor was normal to the x-axis. c) The cross section from the y normal monitor. d) Cross section of the magnetic field for the 20 nm particle at 298 nm, showing interference patterns. e) Zoom in on the same cross section were resonance inside the particle is visible. The monitor was normal to the z-axis. f) Cross section of the electric field from the same monitor zoomed in on the particle.

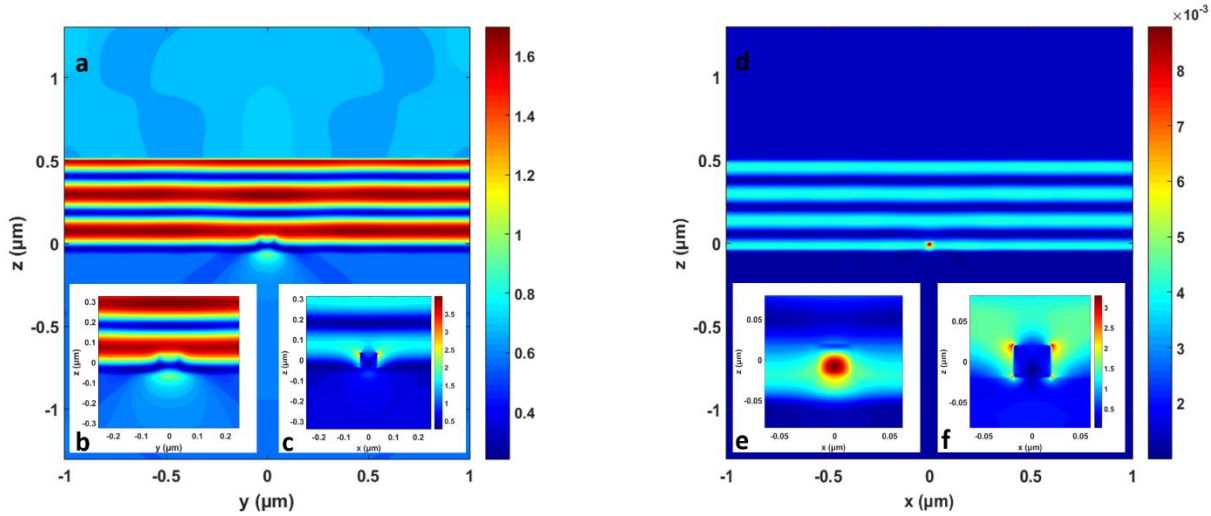

Figure 4.4.6: a) Electric field Cross section of the 70 nm particle at 443 nm with zoom in b) and zoom in of the same monitor c) Magnetic field cross sections under the same parameters. Very low intensity is observed except the upper corners of the particle d) Cross section of the magnetic field for the 40 nm particle at 326 nm (on the valley) showing resonance inside the particle and some lateral scattering. e) zoom in on the image. f) Corresponding electric field cross section zoomed in on the particle. The color scale indicates the intensity of the field.

The cross sections of the fields provide very interestion images. The electric field shown in Figure 4.4.5a) as captured from the monitor normal to the y-axis at 373 nm (on the valley) is at highest intensity in the area above the film. In the zoom in (fig.4.4.5b) we can see that the intensity is high inside the particle as well with a well defined resonance and in the area below it, which clearly indicates the redirection of the light inside the thin film as a result. Figure 4.4.5 d) depicts the z-normal cross section of magnetic field for the 20 nm paticle at 298 nm (on the peak). The interference pattern is present due to the periodicity of the simulation. The zoom in provides a better image of the interesting resonance inside the particle. Lateral scattering is also present here. The inset fig. 4.4.5 f) shows the electric field obtained from the same monitor under the same parameters. In figure 4.4.6 a) a cross section of the electric field at 443 nm (on the peak) for the 70 nm particle shows very high intensity above the film. Although there is no clear sign of interference inside the film the lighter shades below the particle indicate that it directs light into the thin film, increasing its local absorption. The inset c) shows the zoom in on the particle for the magnetic field at the same wavelength showing little to none intensity inside it. The 40 nm particle depicted in figure 4.4.6 d) is exhibiting a resonance at 326 nm (on the peak) for the magnetic. Looking at the zoom in in inset gives a clear image of the well defined resonance. A zoom in on the electric field is also provided in inset fig. 4.4.6 f).

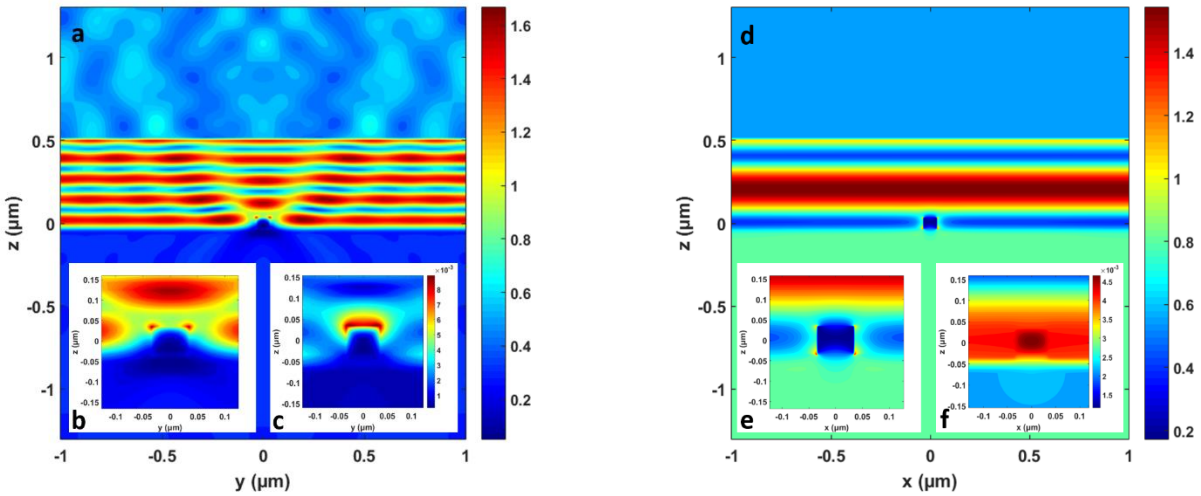

Figure 4.4.7: a) Cross section of the electric field for the 70 nm particle at 250 nm (off peak). b) zoom-in of the same image. c) Zoom in on the particle for the magnetic field under the same parameters. The monitor is normal to the x axis. d) Electric field cross section for the same particle at 800 nm (off peak). The intensity of the field is high above the particle. e) Zoom-in showing nearly zero field intensity inside the particle and higher intensity at the outside corners. f) Zoom in on the particle for the magnetic field under the same parameters.

In the above pictures there are features in the field intensity below the particle which clearly indicate the the light is directed into the film as an effect of the Mie scattering. The most intense is in fig. 4.4.5 b) where the electric field intensity is strong in the lower part of the particle. These features are far more intense in the x-axis monitor hence it was chosen to be shown in these cross-sections instead and of the typical y-axis monitor is shown in the insets.

Figure 4.4.7 a) shows the electric field cross section fo the 70 nm particle at 250 (off the peak) nm obtained from a x-axis normal monitor. The most noticeable feature is the backward scattering i.e in the direction of the light above the particle indicated by the strong field intensity. Some romboidal features above the particle are also visible. The same cross section for the magnetic field can be seen in fig. 4.4.7c) showing much less overall intensity except at the top surface of the particle. The cross section of the electric field at 800 nm for the 70 nm particle is shown in fig. 4.4.7 d) where its intensity is at maximum in the area high above the particle, while inside it (zoom in fig. 4.4.7e) is nearly zero. The magnetic field is shown with a zoom in on the particle in the inset fig. 4.4.7 f). It is showing high intensity inside the particle and in the area surrounding it.

General observations

The samples are similar in characteristics with sizes that peak from 2-6 nm. The maximum values are in the same order of magnitude for both samples. In transmission the maximum values are very close. The FWHM for both reflection and transmission is similar in both samples with small difference of 34 and 48 nm, respectively. The initial disagreement of the simulations and the experiments is due to a difference in sign. In the simulations the reference appears to get, in general, greater value in both transmission and reflection, creating a negative difference. One thing to notice is that in the experiments we did not obtain a cluster larger than 25 nm whereas in the simulations we used up to 70 nm.

Si_3N_4 thickness: 43 nm

The thickness of the silicon nitride film was increased by taking a longer sputter deposition time (23 minutes). For the manufacturing of the first sample, the duration of the cluster source deposition was 10 min. No oxygen was used so the Ar gas flow was returned to 20 sccm. The current was 56.2 W and the aggregation length 20 mm. First the unprocessed data of total reflection and transmission measurements for the reference are presented in the picture below.

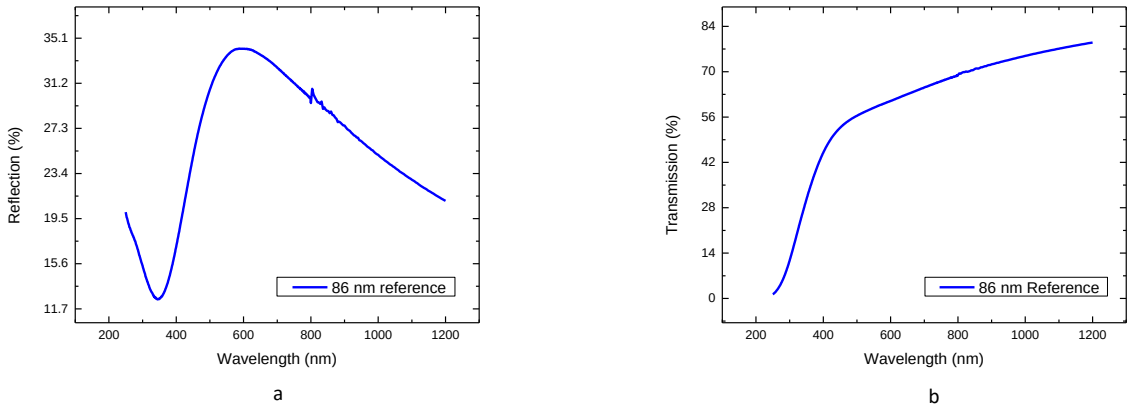

Figure 4.4.1: Total reflection a) and transmission b) optical measurements for the reference sample. The measurements are unprocessed. The wavelength ranges from 250 nm to 1200 nm.

Figure 4.4.1 depicts the raw optical data for the reference sample. 4.4.1a) shows the measurement of total reflection. It is initially decreasing reaching the lowest value at 360 nm then it is increasing until 500 nm where the maximum is located. The transmission graph as shown in 4.4.1b) is initially increasing abruptly until 430 nm where it creates a step and continues increasing until the end of the experimental spectrum.

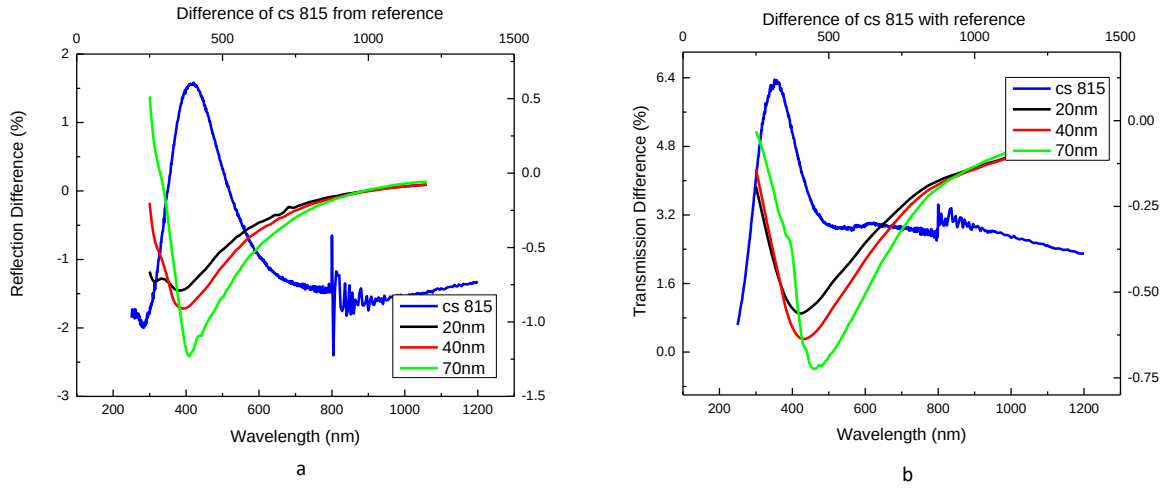

Figure 4.4.2: a) Total reflection difference. b) Transmission difference. The graphs are very similar in shape. The peak of total reflection is at 410 nm and of transmission at 352 nm. The simulations are included represented by the green, red and black lines corresponding to different particle sizes.

The total reflection and transmission difference of the sample from the reference are plotted in figure 4.4.2. The total reflection exhibits a peak at 410 nm measuring a FWHM of 172 nm. The maximum value is 0.75 %. FDTD simulations predicted a valley at 352 nm for the 20 nm particle, at 365 nm for the 40 nm particle and at 382 nm for the 70 nm particle , showing inversed behaviour with the experiment since the position of the peak is not very far away from the positions of the valleys. In the case of the 70 nm particle the difference in position is less than 30 nm. The argument tha the behaviour can be considered inversed can be furthere enhanced by the fact that the the sing of the values around the peak of experimental results is positive, while for the simulations is negative around the valley. Here there is strong dependecne on particle size.

The transmission spectrum has a similar shape and features a slightly sharper peak (FWHM 157 nm) at 352 nm giving a maximum of 6.37 %. The graph is everywhere positive as is the case with the simulations except for the larger particle (70 nm) where it is negative from 250 nm to 483 nm and from 997 nm to the end. The simulations follow the same trend with reflection predicting valleys instead of peaks with strong size dependence. The valleys are located at 400 nm, 415 nm and 450 nm for the 20, 40 and 70 nm particle respectively. The difference between the position of the peak and valleys in the spectrum is higher compared to reflection, indicating a maximum shift towards IR of 100 nm for the 70 nm particle.

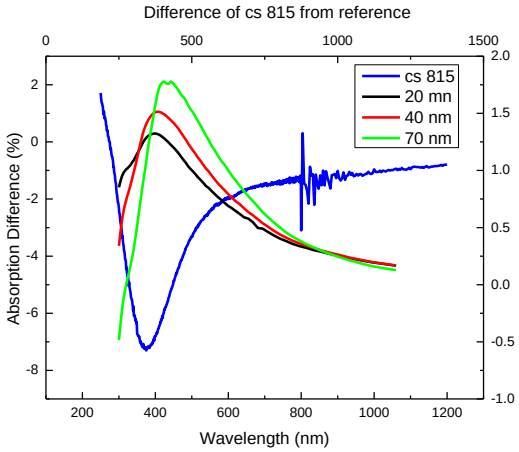

Figure 4.4.3: Absorption difference cs 815. The valley is located at 373 nm and the minimum value is $-7.25\ \%$

The absorption difference exhibits a minimum at 373 nm where the graph shows its minimum value of -7.25 % as depicted in figure 4.4.3. The graph is almost entirely negative showing greater absorption for the reference. The AFM scan shown in figure 3.2.9 indicates that the sample is low in particle density. The particles are less than 10 nm in height as we can see from the height distribution histogram, and the dominant height is just in the range between 1 nm to 3 nm. Following the trend of reflection and transmission the simulations predict peaks that are very close to the experimental valley, at 370, 360 and 415 nm for the 20, 40 and 70 nm particle respectively.

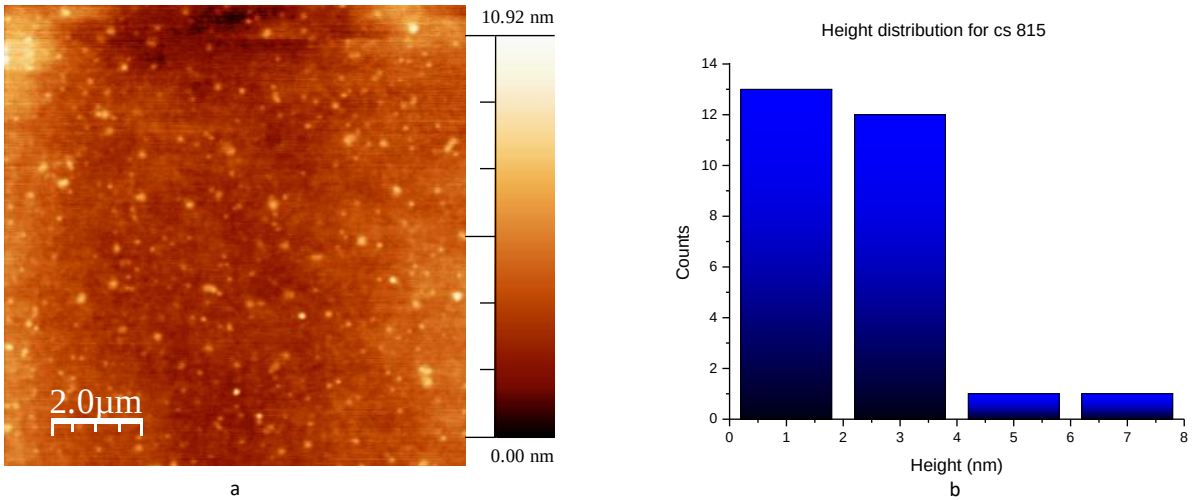

Figure 4.4.4: a) AFM image of cs 815. The particles are sparse and small. b) Height distribution histogram of the sample, showing major heights are in the range of 1 to 3 nm.

Figure 4.4.5 shows the results of the optical measurements for the second sample (cs 827) in the series. The deposition was done on a previous sample that was considered unsuccesful due to extremely low concentration of particles. The sample was made using 40 mm aggregation length and 0.181 A current. First thing to notice is the poor quality of total reflection difference as plotted in fig. 4.4.5a.

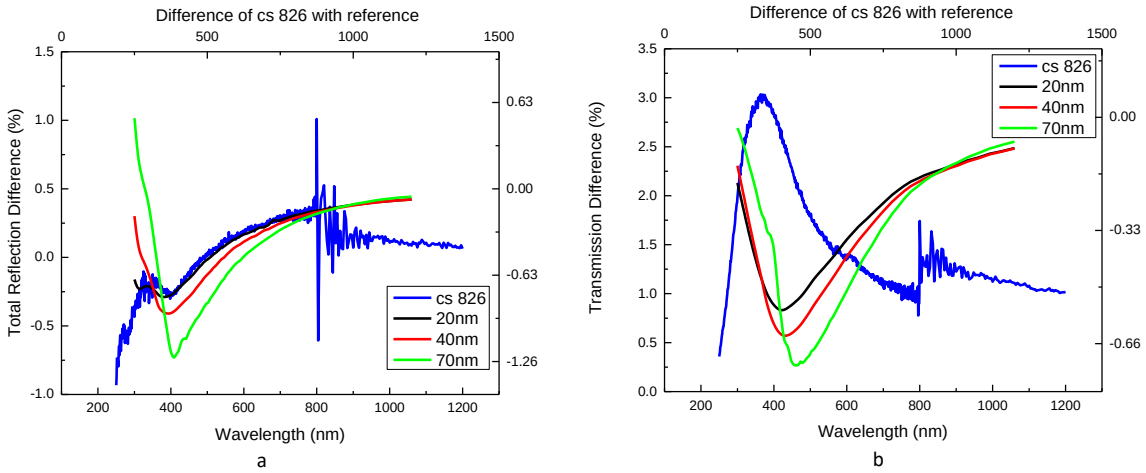

Figure 4.4.5: a) Total reflection difference. The measurement is poor as no peak is visible and there is a lot of noise in the graph. b) Transmission difference per particle with a clear peak at 368 nm.

The signal is noisy and there is no visible peak, however, it seems to agree better with the simulations compared to sample cs 815. Only a slight increase could be identified as a peak at around 300 nm but it is not clear due to oscillations. The transmission difference is shown in figure 4.4.5b and has a peak at 368 nm with a FWHM of 218 nm.

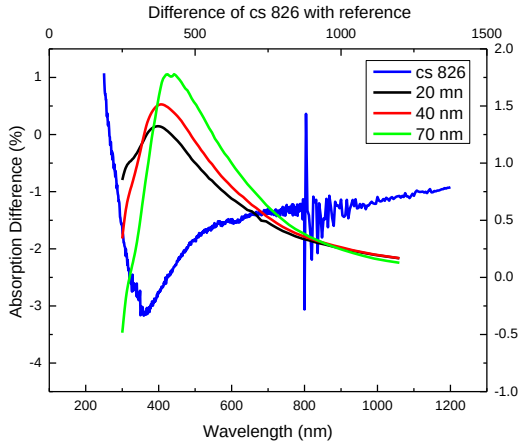

Figure 4.4.6: Absorption difference for cs 826. A minimum can be seen at 360 nm. The difference is negative for the most part of the spectrum starting at 263 nm. The minimum value is -3.15 %

Its maximum value is 1.29 % As with cs 815, transmission diference is always positive and it is exhibinting the same steep increase and overall similar behaviour with the previous sample, making a mismatch with the simulations in terms of sign.

The absorption differece is shown in figure 4.4.6. It starts from its highest value at 250 nm, and reaches a minimum of -3.15 % shortly after, at 360 nm. The graph is negative from 260 nm and remains negative for the rest of the spectrum. The valley is sharper and due to the noisy reflection it also exhibits noise for the most part. The experiments are as with cs 825 in disagreement with the simulations which appears to be a conflict in sign.

With the presentation of the AFM image and histogram we conclude this series. As shown in figure 3.2.12b the overall particle height is small, encountering heights between 1 ant 10 nm with a peak number of particles that measure 7 nm in height.

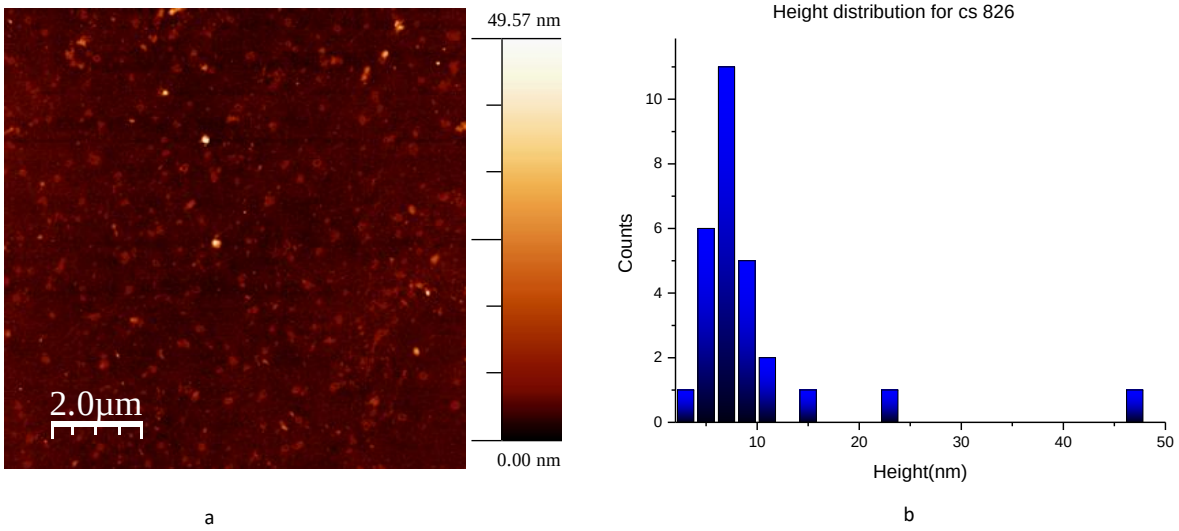

Figure 4.4.7: AFM scan image a) and particle height distribution histogram b) of cs 826. There are lots of small particles that measure at most 15 nm, and some sparse larger that reach 47 nm. A lot of the particles exhibit crater like shape.

There are however scattered particles that measure higher than 20 nm and some going up to 47 nm. Particle density is very low measuring only 7 particles/μm^2. The particle shape is particluarly interesting as we will see in fig. 4.4.7a. The deposited particles appear to be like craters. To further investigate the nature of this particles, additional AFM scans were perfomed, zooming in to examine their composition. In figure 4.4.8 we see two pictures taken when a zoom-in was applied at the sample.

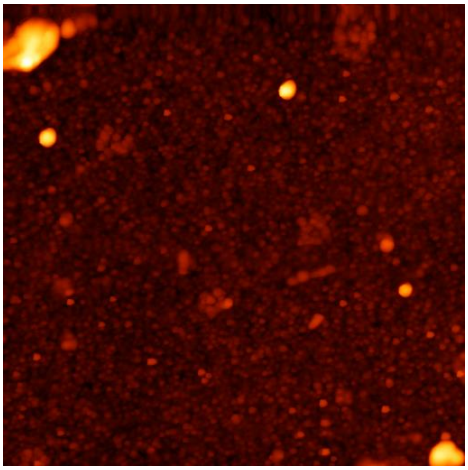

Figure 4.4.8: Zoom-in AFM scan. The craters appear to be an aggregation of small particles forming a circle around a core.

As we can see in the above image the "craters" are formed by smaller particles crouping together. A circle of particles is surrounding a core of aggregated particles. It could either mean that they impacted the surface while still in the process of aggregation, or that this formation is due to an electric charge effect.

The peaks were calculated theoretically as well and are presented in table 4.9 and 4.10. The condition for destructive interference for transmission shows the best agreement with the experimental results.

Sample	λ (nm) Exp	SiN n	λ (nm) m=1
815	410	2.75	236.5
826	-	-	-

a

Sample	λ (nm) Exp	SiN n	λ (nm) m=1
815	410	2.75	473
826	-	-	-

b

Table 4.9: Calculated peaks for reflection using the condition for destructive a) and constructive b) interference formula. Exp denotes the experimental peaks and n is the refractive index of silicon nitride. The peaks were calculated for various integers m, but only the ones that gave the closest result to the experimental are chosen.

Sample	λ (nm) Exp	SiN n	λ (nm) m=1
815	352	2.725	234.35
826	368	2.73	234.78

a

Sample	λ (nm) Exp	SiN n	λ (nm) m=1
815	352	2.725	156.2333
826	368	2.73	156.52

b

Table 4.10: Calculated peaks for transmission using the condition for destructive a) and constructive b) interference formula. Exp denotes the experimental peaks and n is the refractive index of silicon nitride. The peaks were calculated for various integers m, but only the ones that gave the closest result to the experimental are chosen.

The best agreement is met for the condition of constructive interference shown in table 4.9 b). In both samples the calculated results differ by 100-200 nm from the experiments making for a not very good agreement.

The images created by the cross sections of the electric and magnetic field for wavelengths that are on and off the peaks are demonstrated in the following page.

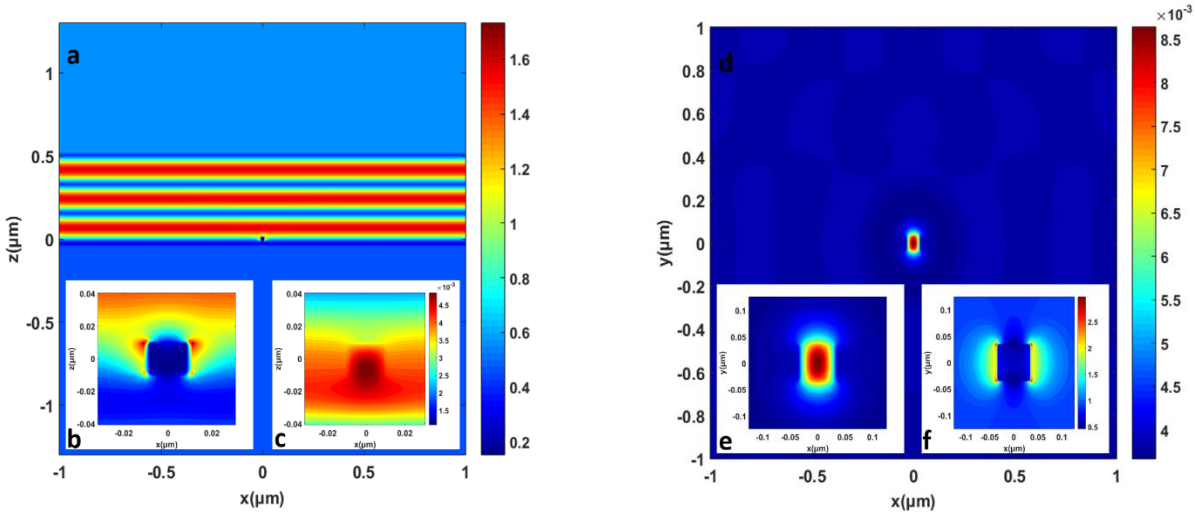

Figure 4.4.9: a) Electric field cross section for the 20 nm particle at 352 nm (on the valley). b) Zoom in on the particle showing intense field on the particle left and right upper sides. c) Zoom in of the magnetic field of the same monitor were the particle can be seen, possibly containing a resonance and interference inside the film. The monitor is normal to the y axis d) Magnetic field cross section of the 70 nm particle at 450 nm (on the peak). e) Zoom in on the same cross section. The monitor is normal to the z-axis. f) Zoom-in on the same monitor for the electric field.

In figure 4.4.9a) the electric field for the 20 nm particle exhibits greater intensity above the film and the particle. The cross section corresponds to the wavelength of 352 nm (on the reflection valley). The field is not intense inside the particle as can be seen in the zoomed-in image (4.4.9b). Figure 4.4.9c) illustrates the magnetic field for the same wavelength and monitor zoomed in on the particle, where the overall intensity is high both inside and outside of it. On the inside the intensity is at maximum. The particle can be identified by the darker shaded square. Figure 4.4.9d) depicts the magnetic field at 450 nm (on the transmission valley) for the 70 nm particle. Intereference patterns are present duw to the periodicity of the structure. In the zoom-in (4.4.9.e) the resonance inside the particle is visible/ The cross section of the electric field at 414 (on the reflection valley) nm for the 40 nm particle is shown in figure 4.4.10a). The intensity is very low inside the film and the particle while it higher above it. The inset 4.4.10b) provides a zoom in on the particle for the privious image with the lateral scatteringon the upper corners

of the particle causes high intensity of the field in these regions. A zoom in on the particle from the same monitor and wavelength for the magnetic field is shown in the inset 4.4.10c). The darker areas show that the magnetic field is maximum there. The final picture is the one obtained from the y-axis normal monitor at 450 nm (on transmission valley) for the 70 nm particle shown in figure 4.4.10d) The field is low above the particle and very intense inside it. Inside the film the magnetic field is low in intensity. A zoom in is provided in order to have a more clear image of the field inside the particle (fig. 4.4.10e). A zoom in is also provided for the electric field for the same wavlength and monitor shown in fig. 4.4.10ff) where it appears to be far less intense than the magnetic field, with only two small areas of high intensity in the upper corners of the particle.

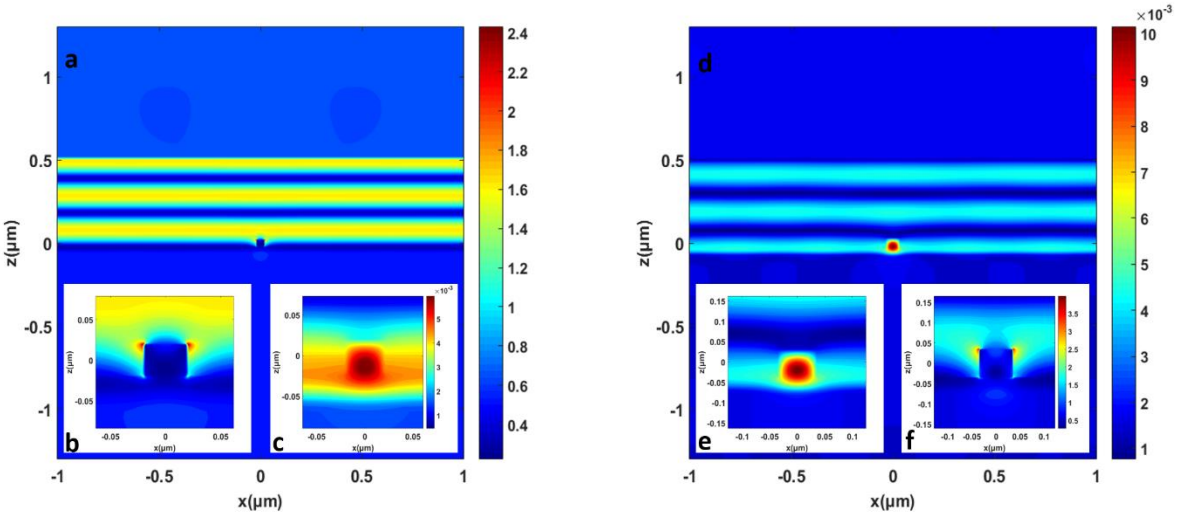

Table 4.4.10: a) Electric field cross section for the 40 nm particle at 414 nm (on reflection valley). B) Zoom in of the cross section showing more clearly the particle. c) Magnetic field zoom in on the same wavelength showing very high field intensity inside the particle and the film d) Magnetic field cross section at 450 nm (on transmission valley) for the 70 nm particle. High field intensity inside the particle is visible. e) Zoom in on the particle showing the intense field inside. f) Electric field zoom in on the same wavelength.

General observations

The particle density is low in both samples with small particle main size (<10 nm) for both samples. CS 826 has few larger particles 15, 22 and 47 nm. The max values for reflection and transmission are one and two (transmission of cs 815) orders of magnitude compared to the 37 nm film. The FWHM is also

much narrower at 172 nm for reflection of cs 815, 157 and 218 for transmission of 815 and 826 respectively. There is a clear shift of about 200 nm in transmission. The simulations show intense particle size dependence and the behavior of the graphs differs in sign compared to the experiments.

Chapter 5

Discussion

We have seen in the results that samples of different Si and Si_3N_4 film thickness exhibit peaks in reflection and transmission spectra for certain wavelengths due to interference effects. The samples frequently contain a variety of cluster sizes, so it makes it difficult to come to a safe conclusion of which size is most likely responsible for these peaks. First, a careful observation must be made on the position of the peak and its relation to the thickness of the film. In the 30 nm Si film three samples exhibit peaks or valleys in transmission at 800 nm and the three remaining at 500 nm. The 70 nm Sa-Si film had three samples in which transmission peaked at 620 nm and 680 nm, and three samples that peak at 575 nm. The thickest film (160 nm) had three samples peaking in transmission at around 720-740 nm and two samples exhibiting two peaks or valleys at about 880-910 nm and 560 nm. Regarding total reflection two samples made with 30 nm film exhibit a clear resonance at 450 nm, which indicates enhanced reflection due to constructive interference. Two other samples of this series show only weak resonances at 625nm and in one case there is no visible peak at all. In the 70 nm thick film reflection showed resonances at 660-670 nm, at 520-540 nm and at 450 nm. Finally, the samples made with the 100 nm thick film exhibited peaks at 850-870 nm, 720-740 nm, and at 530-550 nm. The consistency of the simulations with these results in combination with the fact that there was none or very small shift of the resonance for different particle sizes, leads us to the first key point conclusion that the position of the resonance in the spectrum is dependent on the film thickness.

An investigation must be done to determine what is the cause of these peaks that are observed in the measurements. First, when light is incident on the top surface of the film, part of it is reflected and part of it is transmitted. Part of the transmitted wave can be reflected at the bottom surface of the film and either emerge from the top surface where it can interfere with the reflected wave at the top or it can undergo multiple internal reflections. In the latter case, if two internally reflected coherent waves propagating in the opposite direction meet, constructive interference sets in. As a result, a standing wave

is created that resonates and is amplified. Since the films are not loss less, the resonating wave escapes and is likely able to enhance transmission which explains the peaks in the related graphs. The valleys observed are due to destructive interference between counter-propagating waves. Figure 5.1 illustrates the interaction between counter-propagating waves in the thin film that create a standing wave.

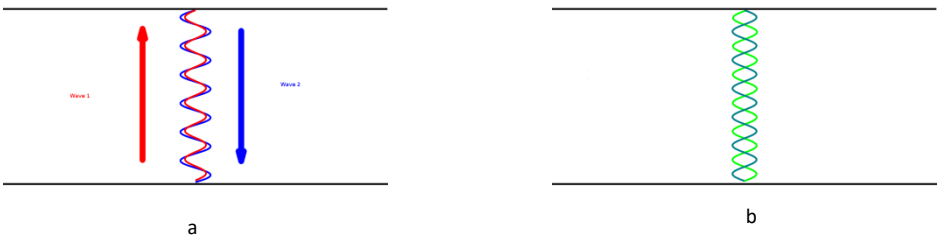

Figure 5.3: Schematic diagram of the creation of a standing wave in the thin film by two coherent contra-propagating waves. In a) the moment the waves meet is depicted. In b) the standing wave is formed.

Enhanced transmission can also occur when the transmitted parts of the multiply reflected waves interfere. If the transmitted waves are in phase they interfere constructively forming the peaks in the transmission graphs, in a similar way with the Fabry-Perot interferometer. The top and bottom surface of the film could act as the optical flats of an etalon. The Fabry–Perot interferometer obeys the interference condition for thin films. The difference is that only one optically flat part of the etalon lets the internally reflected waves to be transmitted. If the transmitted waves are out of phase, destructive interference creates valleys in the transmission function.

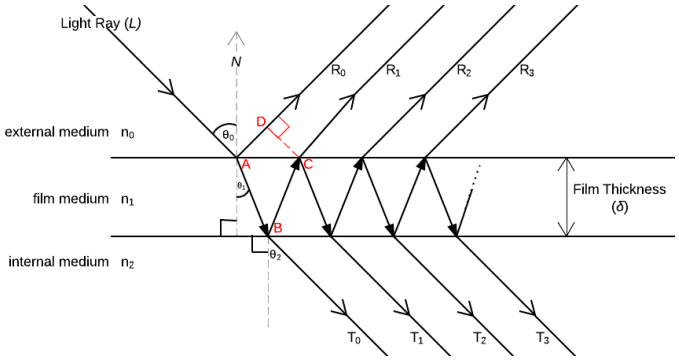

Figure 5.4: Schematic diagram of interference in a thin film. The incident beam is partially reflected and partially transmitted. The transmitted wave can be reflected at the bottom surface and emerge from the top surface interfering with the reflected part. If it undergoes total internal reflection it can subsequently get partially transmitted in both surfaces.[37]

The phase difference itself is dependent on the thickness of the thin film, the refractive index and the angle of incidence. During optical measurements the samples were illuminated at normal incidence so only the refractive index and the film thickness are affecting the light path. If the waves are in phase after the reflection, constructive interference sets in enhancing reflection and giving rise to peaks in the reflection measurements. In the case of destructive interference, the waves cancel out, eliminating reflection (anti-reflection condition) and as a result valleys appear in the reflection function. If the film thickness is a multiple of a quarter of a wavelength, then we have constructive interference. If it is half a wavelength, then destructive interference occurs. The peaks were calculated using the formulas:

$nx = m\frac{1}{2}\lambda$ (anti- reflection)

$2nx = (m + \frac{1}{2})\lambda$ (enhanced-reflection)

The particle size is not taken into account in these formulas. The reason is that according to both the experiments and the simulations, there is very little or non-existent dependence on the cluster size for the position of the peak on the spectrum. Thus the clusters do not provide a tunability of the light-trapping layer, to selected wavelengths.

Consequently, this generates the final and most important question that has to be answered. That is, how do the TiO_2 clusters cause the observed effects in the spectra. The answer is: through Mie scattering. In general, the size range of the clusters is 10 to 160 nm. In order for these clusters to act as Mie scatterers, their size needs to be equal or greater than 1/10 of the wavelength of the incident light. It is evident from the wavelengths of the observed resonances that this is indeed the case, so the clusters are able to cause Mie scattering of the incoming light. Electromagnetic waves impinging on particles which sizes lay in the Mie regime, are scattered in all directions and more strongly in the forward direction i.e. the direction of the incident beam. Therefore, when a sample is illuminated, light is scattered by the clusters in all directions but more intensely in the forward direction towards the thin film. The amount of light that is scattered in the forward direction is dependent on the size of the cluster. The larger the particle is the more forward scattering occurs. However, the scattered light is continuous over the spectrum and not size dependent. The mechanism is illustrated in figure 5.3.

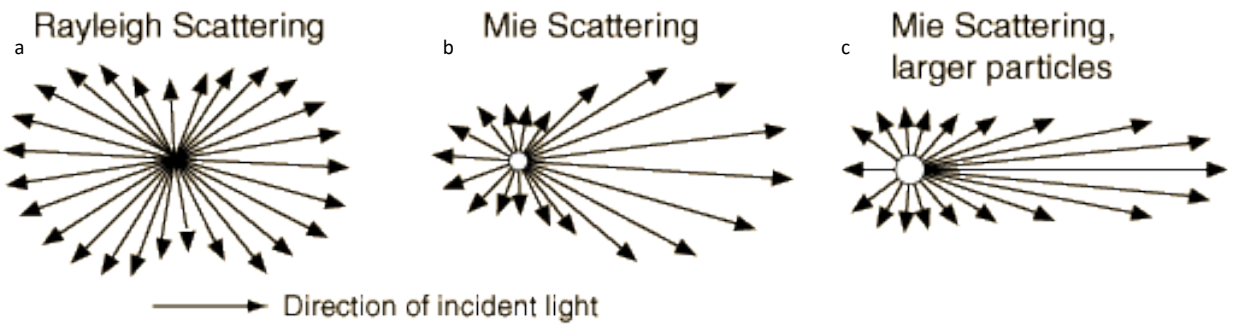

Figure 5.5: Schematic diagram of light scattering by small particles: a) Rayleigh scattering b) Mie scattering c) Mie scattering for larger particles. When light is incident on a particle with size that is equal or greater than 1/10 of the wavelength, it undergoes Mie scattering. It is scattered more strongly in the direction of incidence. With increasing size, the intensity of the forwardly scattered light also increases.[38]

It appears that the resonances are caused by a combination of phenomena, which makes the determination of their nature more complicated. The most notable characteristic of the resonances found in this work is their asymmetric line-shape. This asymmetry is typical of a Fano resonance. Fano resonances emerge when scattering by a continuum of states is coupled with scattering coming from a resonant process caused by excitation of discrete states. Figure 5.4 shows the typical line-shape derived from theory, together with one of the most representative graphs of the results. During the experiments, light scattered by the particles undergoes Mie scattering to form a continuum of states (background procedure). The majority of the Si samples were densely populated, containing a wide range of cluster sizes creating a sequence of Mie scattering processes. Since the light is scattered in the lateral direction as well, it is important to notice that successive scattering of a beam can occur by more than one cluster. The transmitted and reflected part of the scattered light interferes with the reflected and transmitted light from the bottom thin film surface, which has in resonance conditions a standing wave. This gives rise to the combination of a continuous background caused from the TiO_2 Mie scatters combined with the discrete state of constructive or destructive interference of light on the film. This gives rise to the Fano resonances, for certain wavelengths, depending on the thickness of the film.

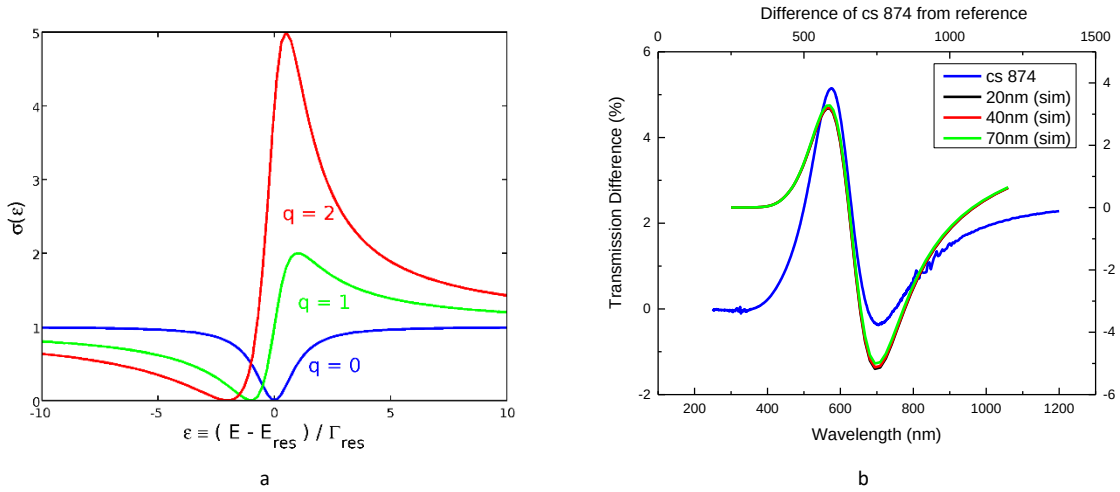

Figure 5.4: a) Scattering cross section as a function of normalized energy for different asymmetry parameters q.[35] b) Transmission difference of sample cs 874 with simulations. The line-shape of transmission here is one of the numerous encountered in the experiments, and it was chosen as the most representative of the typical asymmetry observed in a Fano resonance.

The above figure will provide further understanding on how Fano resonances appear in our system. In the graph of Figure 5.4a) the scattering cross section as a function of normalized energy is shown for three asymmetry parameters q. q is the ratio between intensity of the scattering back ground and the radiation of the discrete transition. The asymmetry parameter determines the asymmetry of the line-shape i.e. how intense peak is. As the value of q increases (more discrete transition), the Fano resonance becomes more pronounced. When its value is close to one, the resonant and non-resonant processes are equivalent and when q=0 only the resonant radiation is present. As stated in the theory section, a higher Fano parameter indicate a dominant resonant process. The prominence is evident in many of our experimental results, especially in the 70 nm and 160 nm thick films. For q=1 and q=2 the graphs exhibit a prominent peak and a valley. The peak is due to the resonant process, in our case the constructive interference of two coherent waves inside the film. The valley indicates the destructive interference of incoherent waves inside the film.

Not all the samples display the same resemblance to a Fano resonance. Although there is some degree of control over the cluster source deposition through variation of parameters, there is still significant randomness from sample to sample. Features such as cluster size and density can vary to a certain degree. In figure 5.5 graphs of total reflection and transmission that indicate less intense Fano resonance signature are shown. This is a very important observation because it further indicates the

significance of the effect that the clusters have on the sample. As it can be seen for instance in a), total reflection exhibits a broad nearly symmetrical peak.

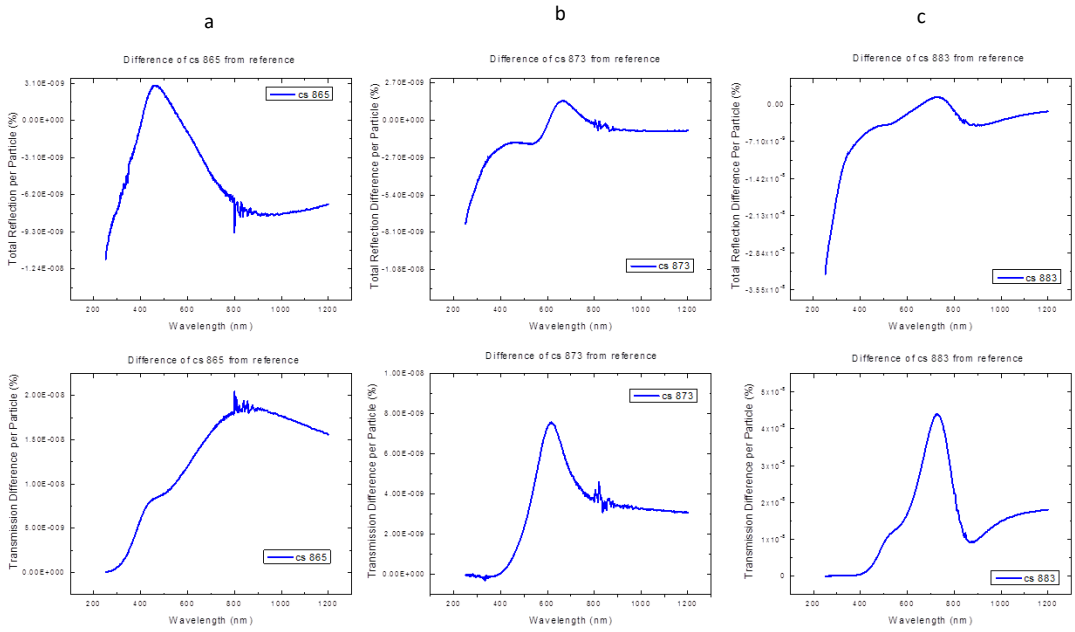

Figure 5.5: Total reflection and transmission difference for three samples that show the least resemblance to a Fano resonance. Cs 865 (a) belongs to the 30 nm thick sample series, cs 873 (b) to the 70 nm sample series and cs 883 to the 160 nm series.

To complete the argument, it is important to acknowledge that the clusters greatly affect the way light behaves upon incidence on the sample. Figure 5.6 shows two graphs of the difference of the results of one of the references, in this case the 30 nm Si film, from the same results reduced by 1%. This one percent corresponds approximately to the surface area lost to the deposited clusters. Comparing the above graphs with the ones of cs 865 demonstrated in fig. 4, one can see the clear difference between the reference and the particle containing sample. Starting with the difference in transmission, no peak is observed in the graph of the reference.

The sample on the other hand displays a peak at 800 nm. Total reflection difference graph for the reference shows a peak at 620 nm. In the sample the peak is observed at 500 nm clearly showing a shift towards UV. It is therefore evident that the TiO_2 particles are responsible for the resonances observed throughout the measurements.

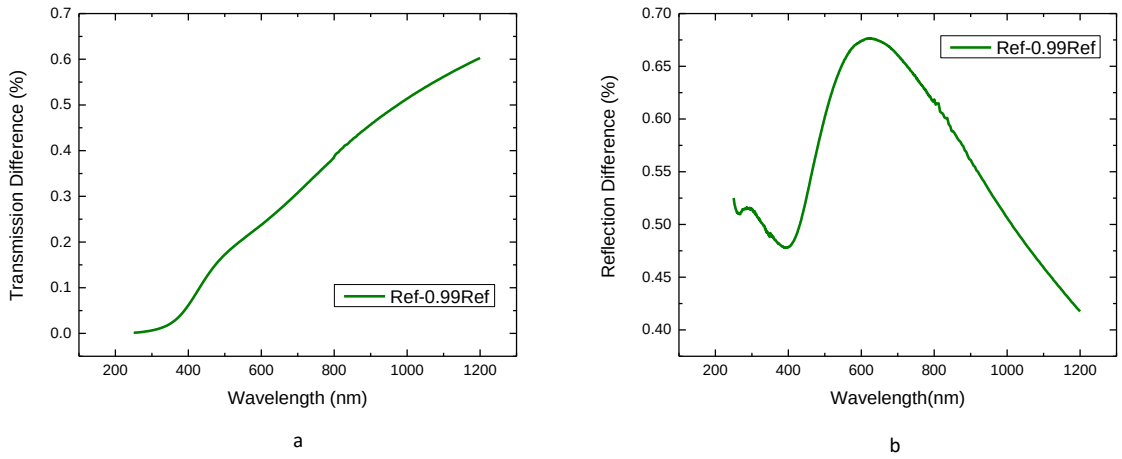

Figure 5.6: Transmission (a) and total reflection (b) difference of the reference from the 99% of reference for the 30 nm thick Si film. Transmission exhibits no visible peak while reflection exhibits a peak at a peak at 620 nm. The corresponding sample (cs 865) shows peak for reflection at 500nm and peak for transmission at 800 nm.

A final point of importance is the absorption and the peaks observed in the graphs. In order to generate more charge carriers more light needs to be absorbed so a peak in absorption indicates that the particle containing a-Si sample absorbs more than the reference. This means that when the light-trapping layer of particles is implemented on a Si solar cell it will effectively enhance photon absorption and create more charge carriers and thereby increase light

Comparison of samples with references

For each film thickness the raw optical data of the reference sample was shown. The behavior of the graphs for the reference showed clear difference from the particle containing sample. Starting with the 30 nm Si film the transmission graph of the reference does not exhibit a peak while the particle samples are showing clear peaks. The 70 nm Si film shows intense difference between reference and particle sample in total reflection graphs. The valley in the reference is not present in the sample instead two peaks are present. The difference in transmission is not so intense since the reference graphs shows a peak which means that the film itself can support a resonance as well. The resonance in the particle sample however is sharper and shifted towards UV. The fact that the thicker films can support more than one resonances, is more evident in the thickest film where we have two peaks in both transmission and

reflection graphs for the particle samples also predicted by the simulations. In transmission the two resonances appear to merge. It should be noted that there is an accuracy issue with respect to the thickness of the film so there might by a small variation within samples. Nevertheless, all these differences between reference and sample graphs serve as strong indicators of the effect of the TiO_2 nanoparticles on the incident light. The difference is also present in the SiN films especially in the 86 nm thick one. The graph of the raw data for transmission here does not exhibit a peak while in the particle sample clearly shows one.

Chapter 6

Conclusions and outlook

The effect of TiO_2 nanoparticles on top of Si and Si_3N_4 thin films, acting as Mie scatterers with the goal to excite optical modes that will lead to enhanced light absorption in thin film solar cells was investigated both experimentally and with simulations. Three different thicknesses were chosen for each film composition. The particle size ranges from 10 to >160 nm. UV-Vis Optical measurements of total reflection and transmission were performed on each sample and reference and the absorption was calculated. The results show that wavelength selective coupling of light to optical modes can occur due to Mie scattering caused by the nanoparticles. Finite difference time domain (FDTD) simulations were performed to further study the phenomenon, which showed very good overall agreement with the experiments and confirm the importance of the nanoparticles.

The majority of the graphs exhibit peaks and valleys in distinct points of the experimental spectrum. These peaks indicate resonances by constructive interference. Destructive interference occurs as well appearing as a valley in the graph. These features gave an asymmetric line shape with the asymmetry being more prominent in the thicker films. The asymmetrical line shape observed is typical of a Fano resonance and is caused by the interference of different scattering sources. The SiN film showed less agreement with the simulated results due to the smaller size of the nanoparticles (in general not exceeding 25 nm). The simulations predicted results that vary with particle size in contrast to the Si where little variation was observed. This feature of the SiN film could be attributed to the fact that Si_3N4 is more transparent than Si. We concluded that the most likely explanation is that the Mie scattering of light caused by the nanoparticles, results in strong forward scattering towards the Si and Si_3N_4 thin films. With combination Fabry-Perot standing wave resonance inside the films it created Fano resonances in the reflection and transmission graphs.

Cross sections of electric and magnetic field provide us with further evidence of the scattering processes. Constructive and destructive interference was observed inside and outside the films. The cross sections were shown for specific wavelengths at which peaks and valleys in transmission and reflection were observed.

An important observation is that sometimes in the graphs of reflection and transmission the experimental results seemed to be inverse in sign compared to the simulations, that is the peak observed in simulations would appear as a valley in experiments and vice versa. This was likely caused by the instruments detection limit for the smallest features. A slight offset between sample and reference could introduce such effects. The random arrangement and variation in size of the particles in the real sample generates more complexity over the physics involved in the process that is yet to be further explored and understood. Therefore, further research is required to provide more insight on the scattering processes taking place. Combined with the relative simplicity and efficiency of the deposition process, this may open the way to new exciting achievements.

Appendix

The results presented here belong to the samples that are very similar to the ones shown in chapter 4, since they do not provide any additional information.

The first sample is cs 865 the particle density has a similar height to the particles on 864. However, the overall particle size is substantially larger. The sample was produced by a 15 min deposition time, with a gas flow of 20 sccm, aggregation length of 40 and power 45.7 W. As before, we start with the results of the optical measurements, presented in the next three figures.

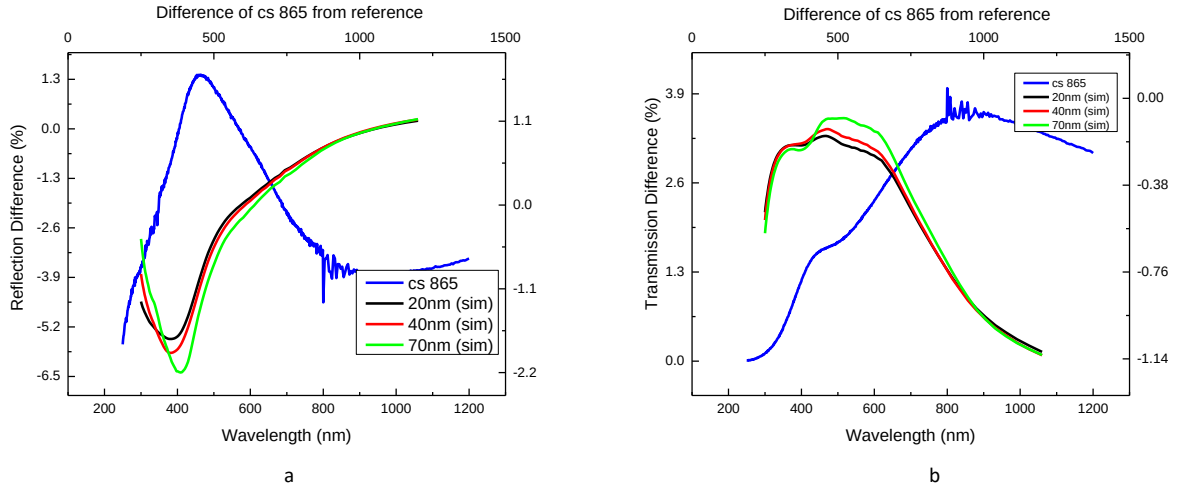

Figure 4.1.4: Total reflection a) and transmission b) difference as a function of wavelength for cs 865 with simulations. The peak in reflection is at 454 nm and in transmission is at 848 nm.

Figure 4.1.4a shows the graph of total reflection difference. A broad peak can be seen at 454 nm and the maximum difference is 2.24 %. The only positive part of the graph is in the range 404 nm to 568 nm. As was the case with cs 864 simulations did not agree initially as the valleys appeared as peaks. The transmission is also similar to cs 865, exhibiting a peak at 848 nm where the maximum difference is 3.68 %. Simulation results are different since the peaks for the different particle sizes are located around 500 nm. Both simulations and experiment are negative everywhere. Figure 4.1.5 shows the graph obtained from the calculation of absorption difference including the simulations.

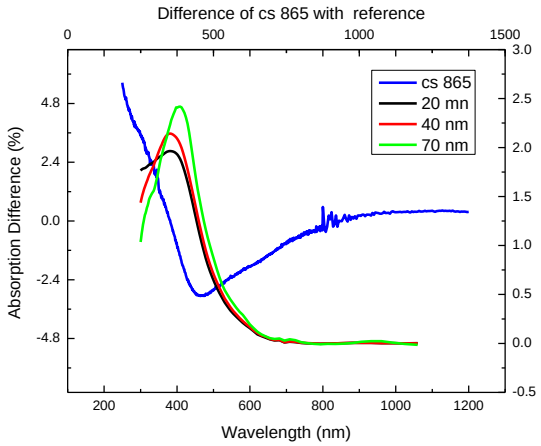

Figure 4.1.5: Absorption difference for cs 865 with simulations. The minimum value is -2.99 % at 466 nm. The peaks of the simulations are located at 359 nm for the 20 and 40 nm particles and at 383 for the 70 nm particle. The graph is mainly positive from 380 to 447 nm.

A steep decrease can be observed in the UV range. The minimum value of the difference is-2.99 %. The difference then increases slowly till the end of the spectrum.

As we will see in the AFM image (fig. 4.1.6a) and height distribution histogram, the main cluster size ranges from 30 nm to 40 nm. The distribution is uniform with a dense layer of small particles with a height around ~10-15 nm, which surround larger, >40 nm particles, which in some cases reach up to 140 nm. The z scale attached next to the AFM image is reaching 218 nm due to a single very large particle that is not included in the counting of the clusters. For the counting a square of 1x1 μm was selected. The density is 48.75 particles/μm^2 %.

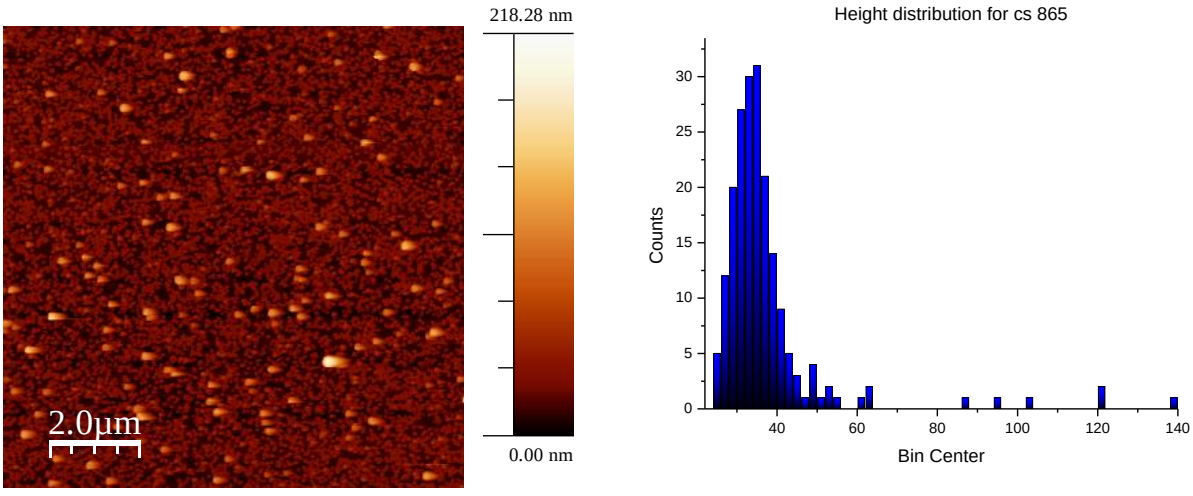

a b

Figure 4.1.6: AFM image a) and Height distribution histogram b) for cs 865. The bin size is 2 nm. The selected area is 2x2 μm. The distribution is high between 30 and 40 nm. The scan area is 10 μm^2 and the particle density is 48.75 $particles/\mu m^2$. The big clusters are over 120 nm in height.

The sample cs 867 has the highest density observed in the set. The aggregation length was 40 mm, the gas flow 20 sccm and the power was 55.6 W. The deposition time was 15 min. The results of the optical measurements are presented in figure 4.1.6

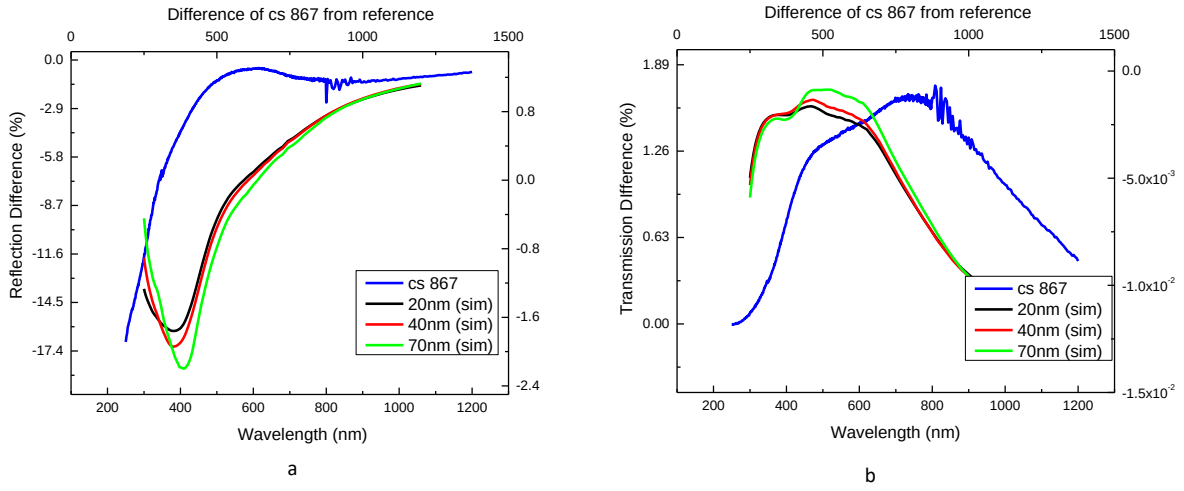

Figure 4.1.6: Total reflection a) and transmission difference b) as a function of wavelength for cs 867 including simulations. The blue lines correspond to the experimental results. Experimental results now resemble more the simulated one in both cases.

The total reflection shows a very small, barely noticeable maximum for the first reference as depicted in fig. 4.16a. Located at 565 nm, it gives a maximum of -0.38%. The FWHM is roughly estimated to be 459 nm. Now the experiments and simulations seem to be more similar despite a small shift, likely caused by a difference in particle size. The peak of transmission is at 843 nm and is broader than the previous two sample (FWHM is 827 nm). Once again the experimental peak needs to be shifted in comparison with the simulation.

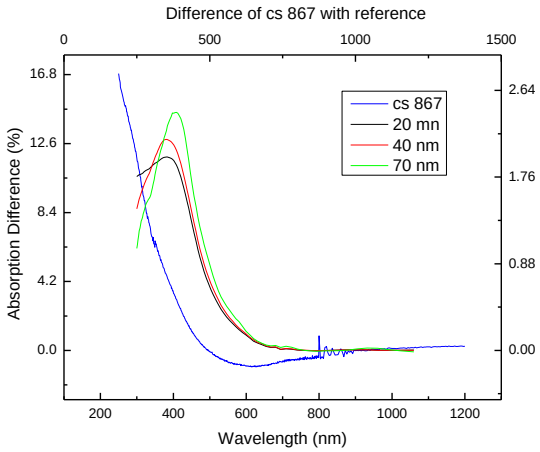

Figure 4.1.7: Absorption difference as a function of wavelength for cs 867 with simulations. The absorption is high in the UV range and decreases rapidly, reaching negative values at 488 nm. The minimum difference is at 600 nm and is -0.98 %. The peaks of the simulations are located at 359 nm for the 20 and 40 nm particles and at 383 for the 70 nm particle.

The peak appears to be a conjunction of two individual peaks. This is more visible in the simulations. The positions of the peaks differ considerably though. The peak in the simulations is at 450 to 500 nm, while the peak of the experimental measurements is at 843 nm and 734 nm for the first and second reference respectively.

The absorption difference as plotted in figure 4.1.7 is more smooth compared to cs 865 and 864. It is negative for a broader part of the wavelength range, namely from 488 nm to 903 nm and its minimum value is $-0.98\ \%$ and is located at 600 nm.

The high density of the deposited clusters creates a nice uniform distribution. There is big variety in the size ranging from 30 nm to greater than 110 nm, which includes the sizes that were used in simulations. The most frequent height is in a range of 50-70 nm as we can see in the histogram of figure 4.1.8b. As it is evident in the AFM image (fig.3.1.8a) and the histogram, the sample contains numerous large clusters, deposited in a high density of 76 particles/μm^2.

The fifth sample in the thinner Si film series is cs 871. We used an aggregation length of 60 mm, with 20 sccm gas glow, deposition time of 15 min and 53.9 W power

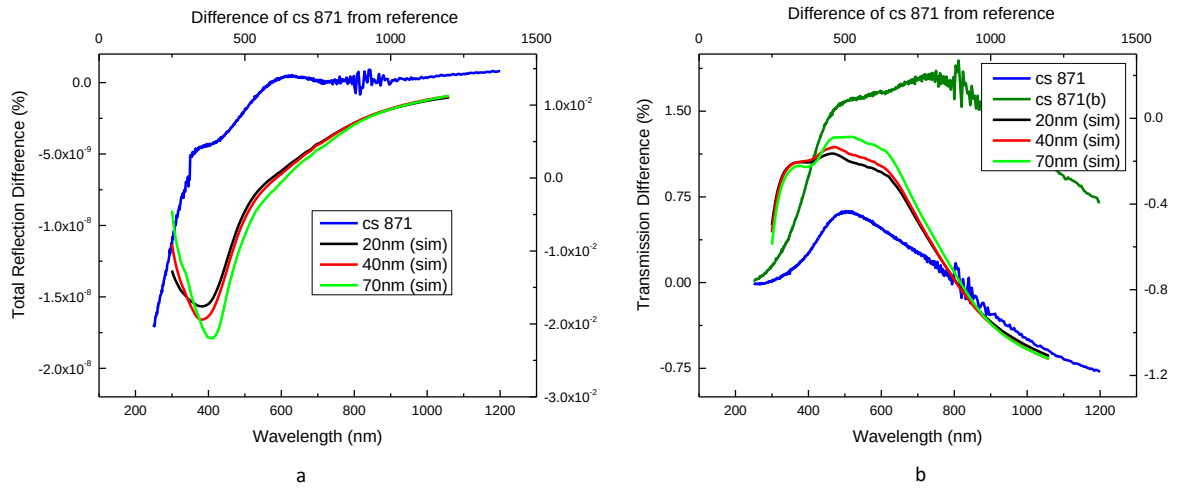

Figure 4.1.12: Total reflection a) and transmission b) difference per particle as function of wavelength for cs 871. A very small peak at 616 nm is visible in reflection. The dark green line in transmission represents the difference from the second reference Transmission peaks at 505 nm (blue) and at 738 nm (dark green).

Figure 4.1.12a depicts the total reflection difference. It appears to show a small bump at 616 nm as in the previous sample (cs 868). The maximum value for the reflection is $1.39\ \%$ and the FWHM is 333 nm. It has positive values in the interval 486-643 nm and everywhere else is negative.

For this sample, the transmission difference is plotted for both references due to significant difference from each other. Following the trend of the previous samples it exhibits a very broad peak, especially for the difference with the second reference (green line). The peak of the difference from the first reference, appears at 505 nm with a maximum value of $0.63\ \%$. In the difference of the second reference appear to be two peaks, one at 505 nm as in the blue line and one at 738 nm. The first peak at 505 nm is more consistent with the one observed in cs 868.

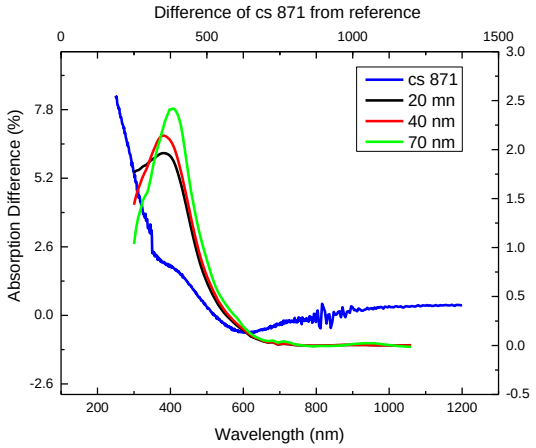

Figure 4.1.13: Absorption difference as a function of wavelength. The absorption is high at the UV and decreases rapidly at the violet range. The peaks of the simulations are located at 359 nm for the 20 and 40 nm particles and at 383 for the 70 nm particle.

The maximum value is $3.23 \cdot 10^{-9}\ \%$ and the FWHM is 512 nm. The maximum for the green line is 1.84 % and its FWHM is 702 nm. Comparing with the simulations we see strong agreement in the position of the peaks. The second peak present in the green line resembles more the simulated results since it is merged with the first one.

In figure 4.1.13 the absorption difference is plotted. It starts from the highest value and decreases slightly slower compared to the previous samples. It is positive except in the wavelengths from 508 nm to 695 nm, where at 600 nm gets the minimum value, which is $-0.72\ \%$. These results do not agree with the included simulations.

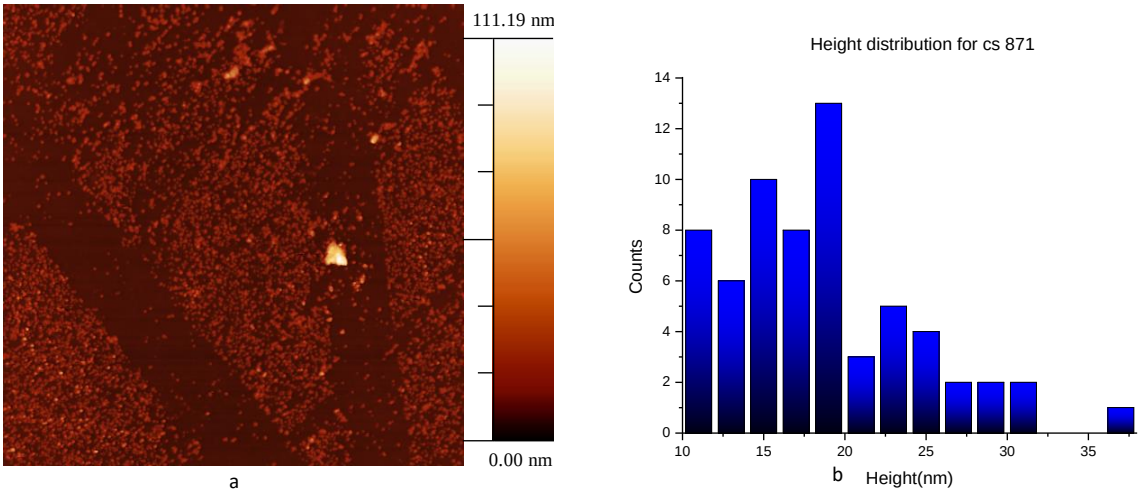

Figure 4.1.14: AFM image a) and height distribution histogram b) of cs 871. The scan area is $10\ \mu m^2$. The selected area for the particle count was $1\ \mu m^2$. The particle density is$60\ particles/\mu m^2$.

The AFM image and height distribution histogram are shown in figure 4.1.14. We can see from the image that the distribution of the particles is not entirely uniform. There are stripes of empty space, which were taken into account when counting the particles. The clusters are somewhat smaller, with the main particle size is between 15 and 20 nm ad the maximum is at 37nm. The z scale maximum point is 119 nm due to the overly big particle in the center right of the image.

Our final sample of 30 nm thick Si film, is cs 872. The aggregation length was 60 mm, the gas flow 20 sccm the deposition time was 30 minutes, and the current was slightly higher at 66.48 W. The results of the optical measurements are presented in figure 4.1.15.

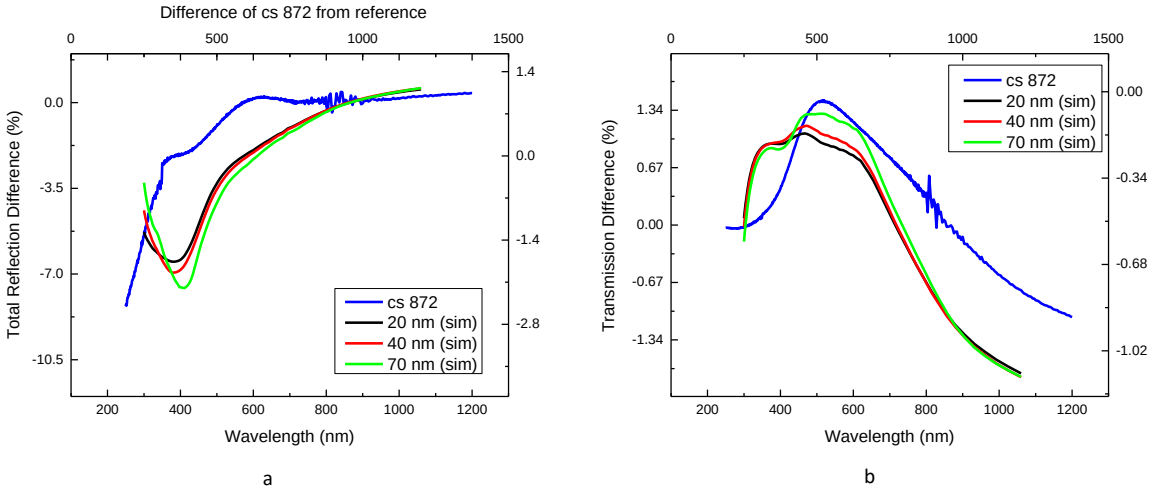

Figure 4.1.15: Total reflection a) and transmission b) difference as a function of wavelength for cs 872. The light green, red and plack lines are the results of the simulations for each particle size.

As we can see in the graph the total reflection increase upon going to larger wavelengths without a clear maximum. The transmission has broad peaks at 516 nm, with corresponding maximum value of -0.03 % The FWHM of the peak is 457 nm. The simulated transmission for the 20 nm and 40 nm particle, exhibit a peak at 450 nm. For the 70 nm particle the peak is slightly shifted at 500 nm. The graph takes positive values for the most part of the spectrum, getting negative at 947 nm. This makes for a good agreement of the experimental and simulated results.

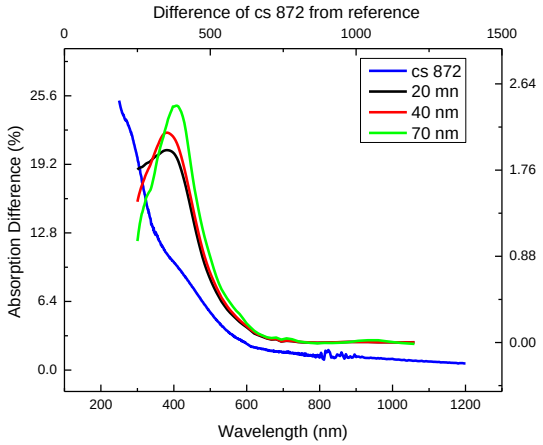

Figure 4.1.16: Absorption difference as a function of wavelength for cs 872. No peak or minimum is observed. At 600 it starts approaching zero. The peaks of the simulations are located at 359 nm for the 20 and 40 nm particles and at 383 for the 70 nm particle.

In figure 4.1.16 we see the results of absorption difference for the sample. The graph starts with a high initial difference, compared to the previous samples, starting from 25 % and decreasing fast in the UV and violet range. At 600 nm they smoothly approach zero, without reaching a distinct minimum. In terms of overall behavior, the experiment agrees fairly with the simulations except the absence of a peak.

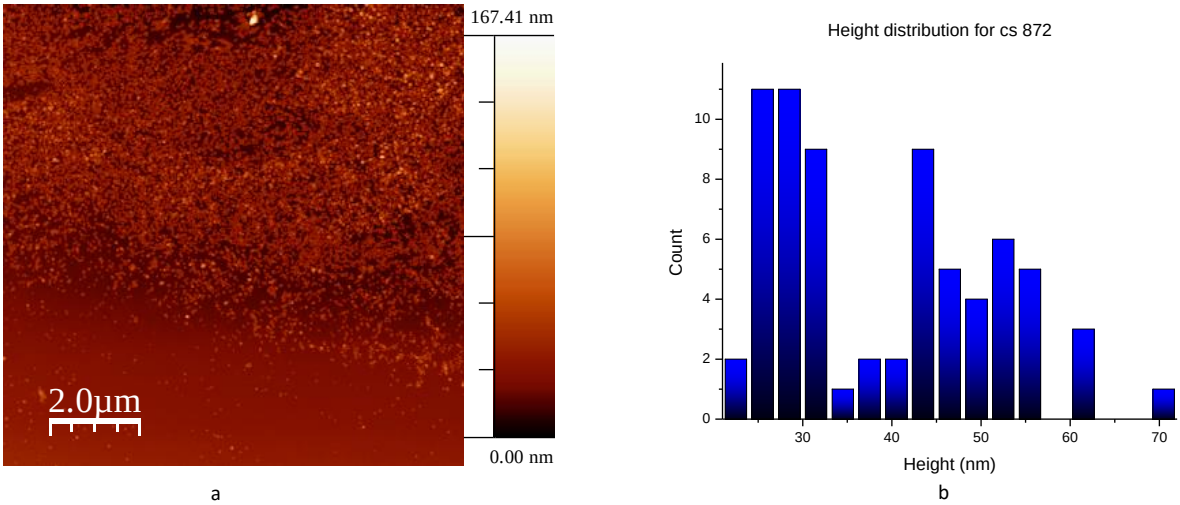

Figure 4.1.17: AFM image and height distribution histogram for cs 872. Next to the AFM image the z scale is attached. The scan area is $100\ \mu m^2$. The selected square for the counting of the particles was 1x1 µm. The bin size of the histogram is 2 nm.

The AFM image and height distribution histogram are shown in figure 4.1.17. The deposition yielded a sample with uniform layer of particles, except a part of image which is relatively empty. This area was subtracted from the overall scan area, to provide more accurate results for the particle density, which is $71\ particles/\mu m^2$. The particles are large reaching up to 70 nm in height. The distribution is more uneven compared to the previous samples, with the counts of the particles reaching maximum in the range of 15 to 30 nm, but also with a second smaller peak at 45 nm. We could say that there is a second dominant size, in the range of 45 to 55 nm.

Si thickness 70 nm

For the creation of sample cs 875 we did a cluster source deposition of 20 min. The aggregation length was 60 mm and the power was 53.5 W. The deposited particles are smaller here and far sparser, compared to the previous sample. The deposition time is the optimum for obtaining a dense layer of particles.

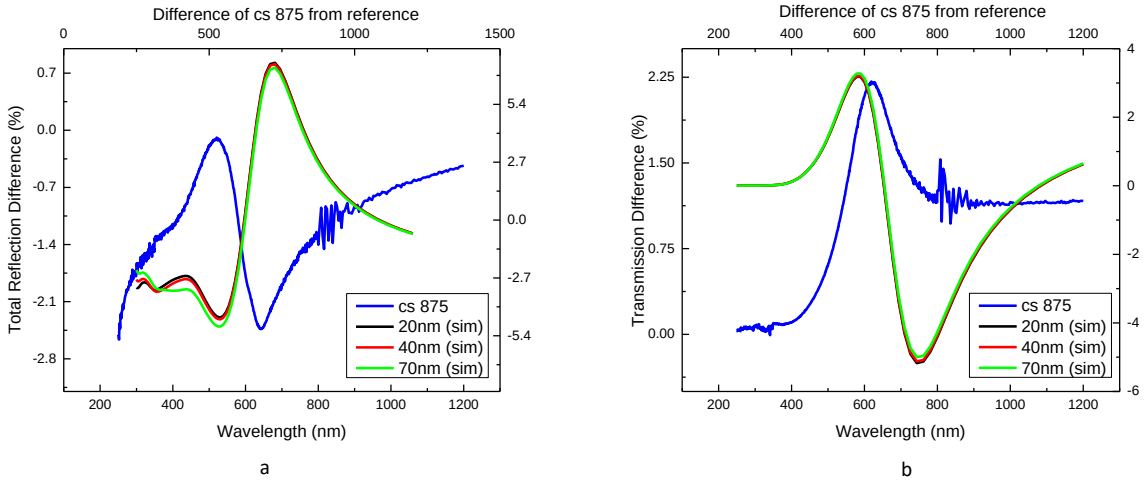

Figure 4.2.7: Total reflection a) and transmission b) difference per particle as a function of wavelength for cs 875 (blue line) with simulations (green, red and black).

Figure 4.2.7a shows the graph of total reflection difference. The measurements of the total reflection show one peak at 521 nm where the difference gets its maximum value of -0.11 %. It is narrow, measuring FWHM of 176 nm. The experiments here deviated more from the simulations since the predicted peak for the reflection is at 722 nm and the behavior of the graph is considerably different. It starts from a minimum point at 250 nm, after the peak a sharp local minimum follows at 643 nm and then the difference is increasing until the end of the spectrum. Additionally, it was entirely negative.

The transmission difference as depicted in figure 4.2.7b (blue line), has a peak 619 nm and the maximum is 3.04 %. The peak's FWHM is 216 nm. The graph is positive in the whole spectral range of the experiment and it does not exhibit a minimum after the peak. Instead, after some oscillations at 800 nm it becomes almost constant. We know that simulations predict a peak at 582 nm, which constitutes very good agreement with the experiments, except the absence of the valley.

The absorption difference was calculated and the resulting graph can be seen in figure 4.2.8. As with the previous samples, light in the UV range is highly absorbed by the glass substrate. The absorption starts decreasing fast at 450 nm and its minimum value is positioned at 600 nm. The difference is turning negative already at 470 nm, and remains negative until 619 nm. It becomes negative again at 812 nm until the end of the experimental spectral range.

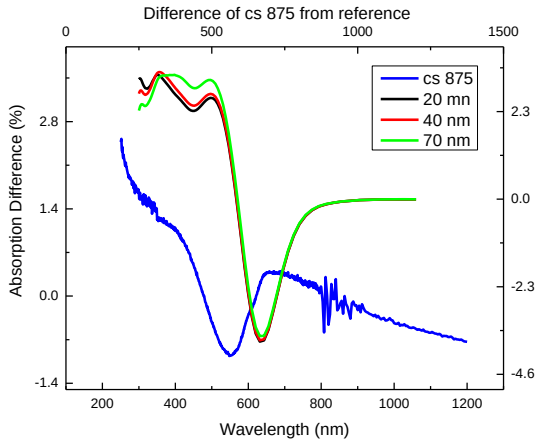

Figure 4.2.8: Absorption difference as a function of wavelength for cs 875.The absorption is mostly positive and reaches a minimum of -0.94 % at 552 nm and is negative in the ranges 475 nm to 619 nm from 812 nm to the end of the spectrum.

The minimum value for the difference from the reference is -0.94 %. The signal becomes noisy at around 800 nm. The absorption is positive for the most part of the graph, except in the ranges 475 to 619 nm and 812 nm until the end of the experimental spectrum.

As mentioned earlier, the particles are sparse and small in size. There is no particular variation in the cluster size as the height ranges from 10 to 15.5 nm for the whole histogram. The z scale of the AFM image goes up to 35.94 nm. This is because of two particles in the area that are higher than 30 nm not included in the 1x1 µm square selected for counting and height measuring. The bin size of the histogram is 2 nm. The density of the sample is 8 particles/μm^2.

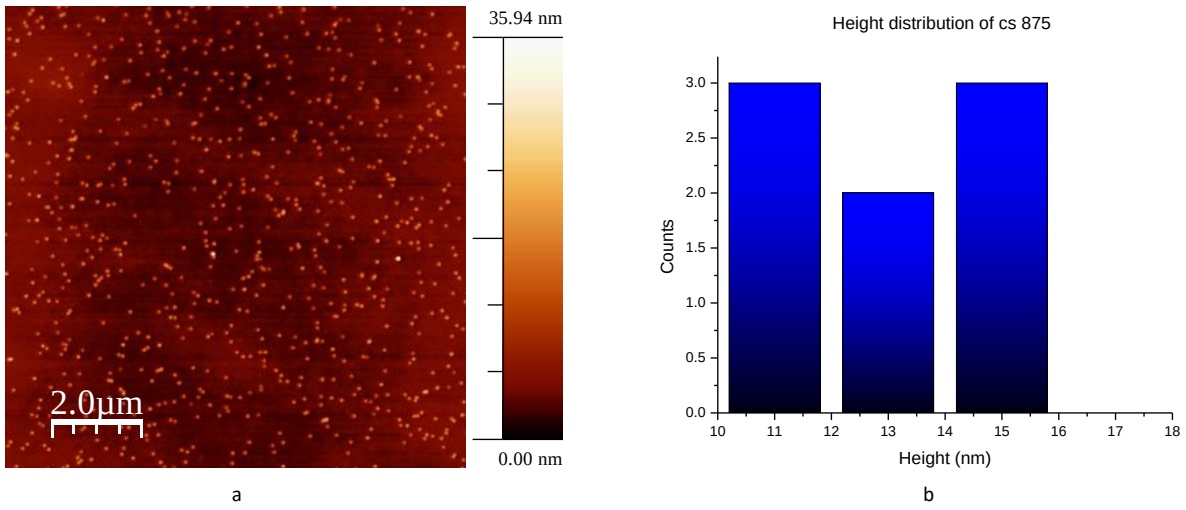

a b

Figure 4.2.9: AFM image a) and particle height distribution histogram b) of cs 875. The particles are less than 20 nm in height except two individual cases that are >35 nm judging by the z scale attached next to the image. The histogram is not very detailed, due to the scarcity of the particles.

The fourth sample in this series is cs 876. The cluster deposition was 20 minutes long and we used an aggregation length of 60 mm. The power was at 65.82 W. The results of total reflection and transmission difference are shown in figure 4.2.10. From the total reflection difference graph, we can see two distinct peaks. The highest peak is positioned at 662 nm. The peak is narrow with FWHM of 192 nm. The maximum value is $8.14\ \%$ .The graph then starts decreasing and becomes negative at 600 nm. At 410 nm the second peak is observed, corresponding to the first and second reference respectively. The smaller peak is broader and its FWHM is 445 nm. The simulations as we know exhibit a high peak at 722 nm and a lower

at 424 nm. It is obvious that the experiments are in very good agreement, as we can also see in the graph which follows the same behavior regarding both the position of the peaks and the sign of the values.

The excellent agreement of simulations with experiments is also evident in the graph of transmission difference (fig.4.2.10b). A narrow peak is present at 577 nm and it has FWHM of 134 nm. The difference gets a maximum value of 5.11 % at this point. The peak in the simulations is at 582 nm only 5 nm away from the experimental result. In total the graphs of the experiments and simulations behave in almost the same way starting from a value from or close to zero 250 nm and increasing, forming a deep at 747 nm in the simulations and at 713 nm in the experiment. In both cases the graph is negative at this point. The experimental graph is negative for the interval 667 nm to 806 nm and the simulations are negative for longer in the range 655 nm to 1079 nm, also exhibiting a more prominent valley.

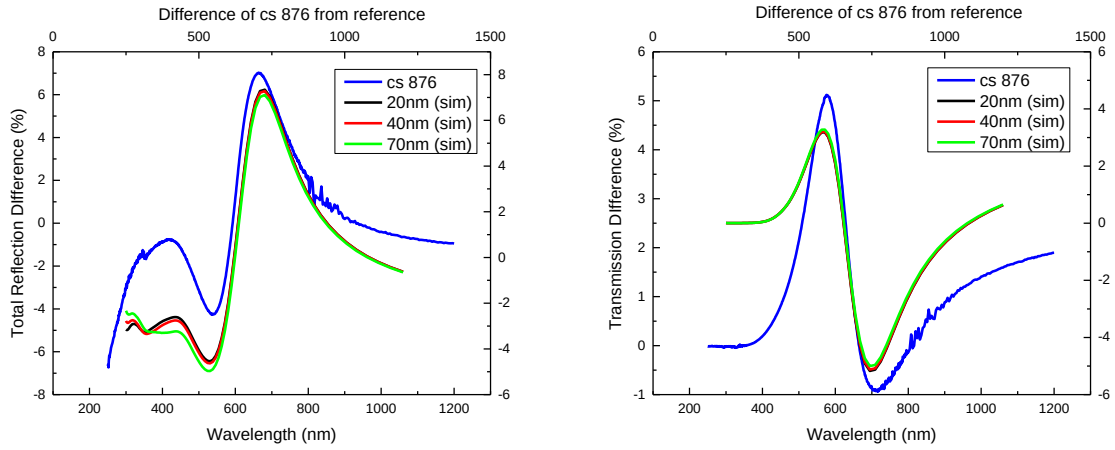

Figure 4.2.10: Total reflection a) and transmission b) difference per particle as a function of wavelength for cs 876. The experimental results are represented by the blue line. The simulations are represented by the green, red and black line. The peaks of the experiments match the simulations perfectly.

The absorption difference as we see in figure 4.2.11 follows a bit different path compared to the previous sample. The graph shows a slowing down of the decrease in absorption, which at 447 nm starts to increase forming a small peak at 510 nm where the local maximum is 1.13 %. Then it reaches a minimum at 633 nm slightly further away than usual, where its value is -7.83 %. It retains negative values for wavelengths from 603 nm to 678 nm and becomes constant at 1000 nm.

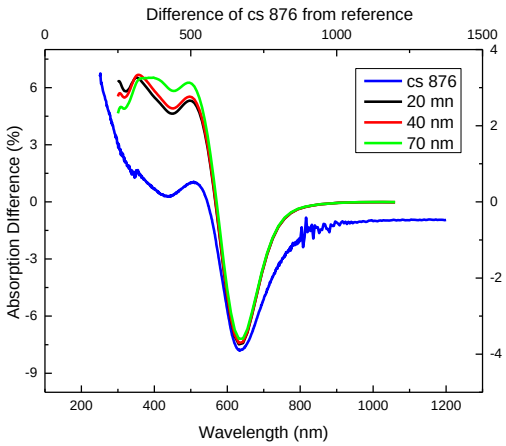

Figure 4.2.11: Absorption difference as a function of wavelength for cs 876. We can see here a small peak at 510 nm, and then a minimum at 633 nm which is slightly shifted compared to the previous samples.

In figure 4.2.12a) the AFM scan image is shown and we can see that there are plenty of clusters deposited, creating a high surface density measuring 54 particles/μm^2. Clusters are diverse in height ranging from 17 nm to 50 nm (fig.4.2.12b). The dominant height is between 17 nm and 29 nm with the most encountered height at 22 nm. The distribution was calculated by counting the clusters and measuring their height in a selected square, 1x1 µm in dimensions. As with some previous sample the z color scale maximum (91 nm) is higher than the largest cluster shown in the histogram due to individual clusters not included in the square.

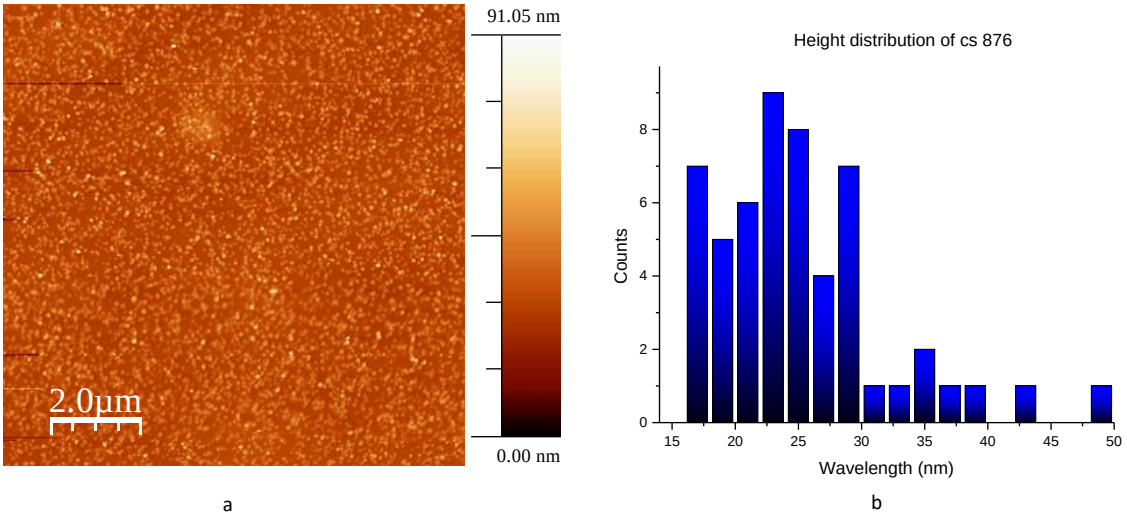

Figure 4.2.12: AFM image a) and particle height distribution histogram b) of cs 876. The particle density is high at $54\ particles/\mu m^2$. The scan area is 10x10 µm. The bin size is 2 nm. The main particle height is in the range 17 to 30 nm.

Sample cs 877 was fabricated using a 40 mm aggregation length. The cluster deposition lasted for 20 minutes, using power of 53.5 W. It is important to notice that the optical measurements yielded similar results to the ones observed in the sample cs 875 as we will see in the results plotted in figure 4.2.13.

The total reflection difference is depicted in figure 4.2.13a. We can see in the graph that it exhibits a peak at 537 nm and a valley at 666 nm, which perfectly matches the simulations. The corresponding maximum value is 3.56 %. The FWHM is 200 nm. There is no lower peak here although a small bump is slightly visible but due to noise is difficult to say safely. At 600 nm the graph starts taking negative values until 870 nm where it is slowly going up again. At 666 nm reaches the minimum value.

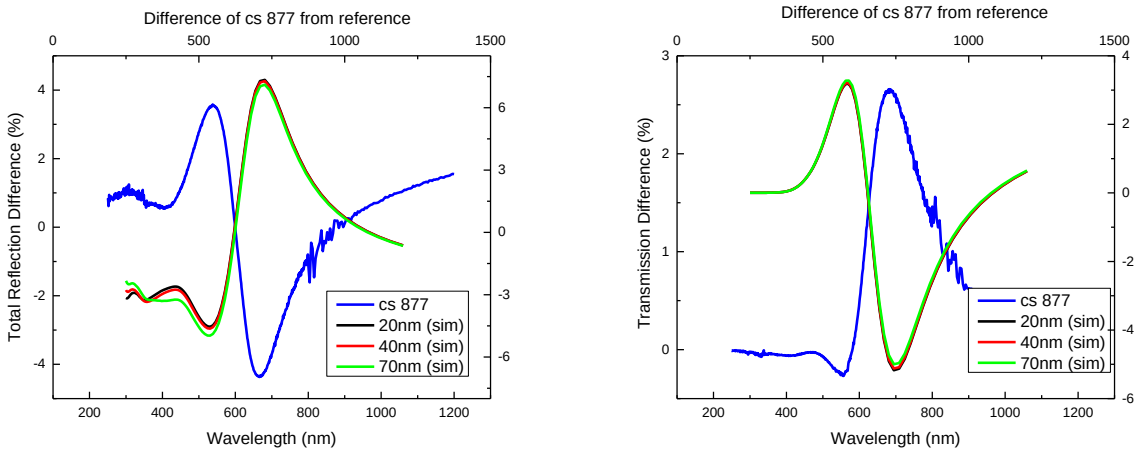

Figure 4.2.13: Total reflection a) and transmission b) difference per particle as a function of wavelength for cs 877 with simulations. The position of the peak differs from the simulations in both cases. The peak in reflection a 537 (blue line). Transmission (experimental) exhibits a peak at 566 nm.

The transmission was also different from the simulations. It is showing a very clearly defined peak at 682 nm which is nearly 100 nm away from the simulated ones. A maximum value of 2.65 % is reached at this point. The FWHM of the peak is 139 nm. The minimum observed in the simulations is also present in the experiment. It can be seen as a very small barely noticeable valley after the peak at 682 nm. The

experimental graph starts with values just above zero from 250nm until 579 and it turns negative for the rest of the spectrum.

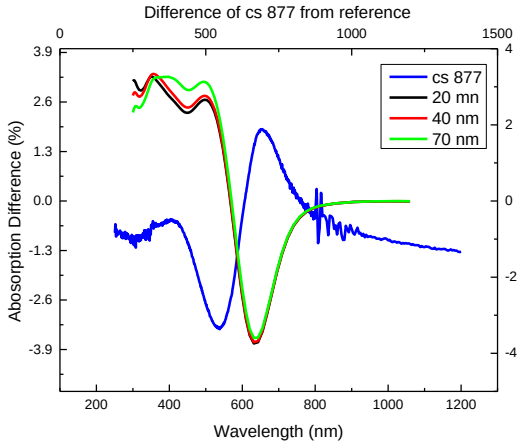

Figure 4.2.14: Absorption difference as a function of wavelength for cs 877. The t peak is located at 400 nm and 618 nm. Most part of the absorption is negative.

The results of the absorption difference are shown in figure 4.2.14. The graphs are different to what we have seen so far in this series of samples. In addition to the typical minimum that is usually observed around 600 nm which here is at 537 nm, a peak is also existent at 651 nm.

The maximum absorption difference for the reference is 1.91 %. Most of the graph is negative except near the peak in the range from 605 nm to 757 nm. The minimum difference is -3.39 %.

In figure 4.2.15a we see the AFM image with the particle height distribution histogram. Now we can see clearly see the similarity of thus sample to cs 875. The clusters are very small, with height that ranges from 6 to 16 nm. The dominant height is in the interval from 8 nm to 12 nm. The difference in behavior in these two samples compared to the rest of the set, can be explained by the fact that there are very few and small particles here. The surface density is only 2.28 particles/μm^2 calculated using a square 5x5 µm to count and measure the clusters.

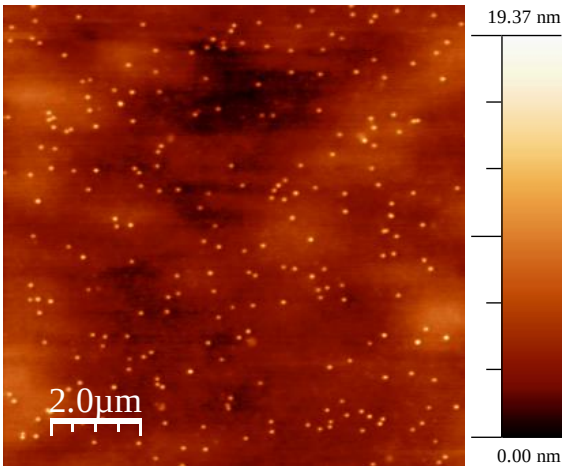

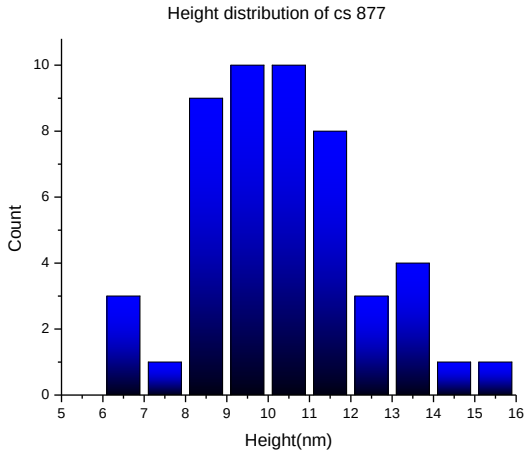

a b

Figure 4.2.15: AFM image a) and particle height distribution histogram b) of cs 877. The main particle size is in between 8 and 12 nm. The selected square for the counting of the particles was 5x5 µm. The bin size is 2 nm. The sample is very sparsely populated.

We complete this set with cs 878, which was made with a shorter deposition time of 15 min. The aggregation length was 40 mm and the power was 60 W. We start with the presentation of total reflection difference and transmission difference shown in figure 3.2.16.

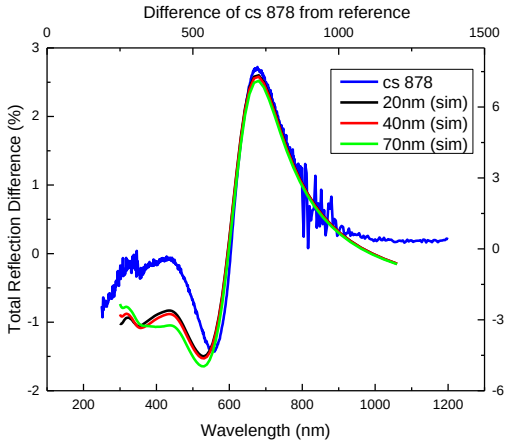

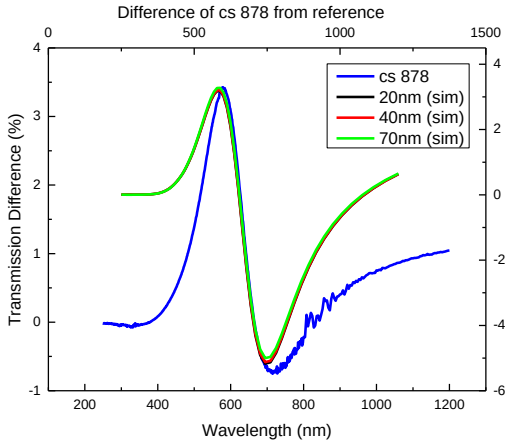

a b

Figure 4.2.16: Total reflection difference (a) and transmission difference (b) as a function of wavelength for cs 878.The experiments agree perfectly with the simulations in the total reflection, while they differ in the transmission.

The experimental results for the total reflection (fig. 4.2.16a) difference show a peak at 668 nm where the maximum value is 2.71 %. The FWHM of the peak is 166 nm. The lower peaks observed in the majority of the samples are also present here at 439 nm, although in the first reference it is not very clear.

In the graph for the transmission difference (fig 4.2.16b) we see that the results are more similar to the ones observed in samples cs 875 and 877. The peak is located at 619 nm, and its corresponding maximum value is $3.43\ \%$. The FWHM of the peak is 263 nm. The experimental graph takes positive values in the entire spectral range.

Comparing the experimental reflection results with the simulations, we can see that they are in excellent agreement. As we know the peaks of the total reflection for the simulations are at 722 nm and 424 nm for the high and low peaks respectively. The peaks of the simulations are at 582 nm. It is obvious that the positions are very close to the experiments. It is interesting though that transmission behaves in the same way as samples cs 875 and 877. Taking into consideration the behavior of total reflection, we could say that the current sample is a combination of the two trends we saw in this series. The results of the absorption difference followed by the AFM image and height distribution histogram are shown below. In figure 4.2.17 the results of the absorption difference are plotted. The difference is negative for almost the entire spectral range except a small interval in the UV which however exhibits oscillations. The shape is similar to the one followed by the majority of the samples. The highest values are in the UV range, and then the graphs smoothly decrease reaching minimum value of -3.31 % at 625 nm.

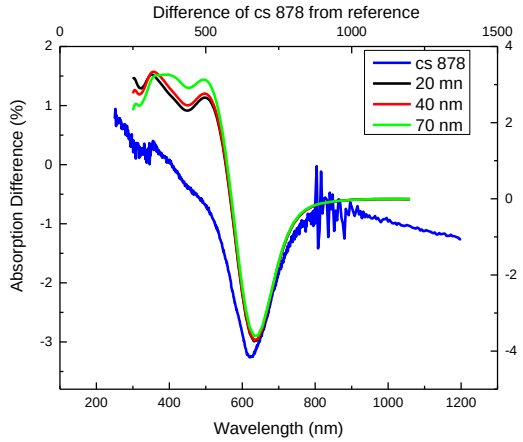

Figure 4.2.17: Absorption difference as a function of wavelength for cs 878. The deep observed is at 625 nm and the graph is negative in the whole spectral range.

The surface density of our sample is high as it is evident in figure 4.2.18a where we can see a great amount of clusters has been deposited. Its difference from the other dense samples made with the current Si film thickness, is that there are fewer large (>50 nm) particles). The distribution ranges from 5 nm to 40 nm with one column above 50 nm.

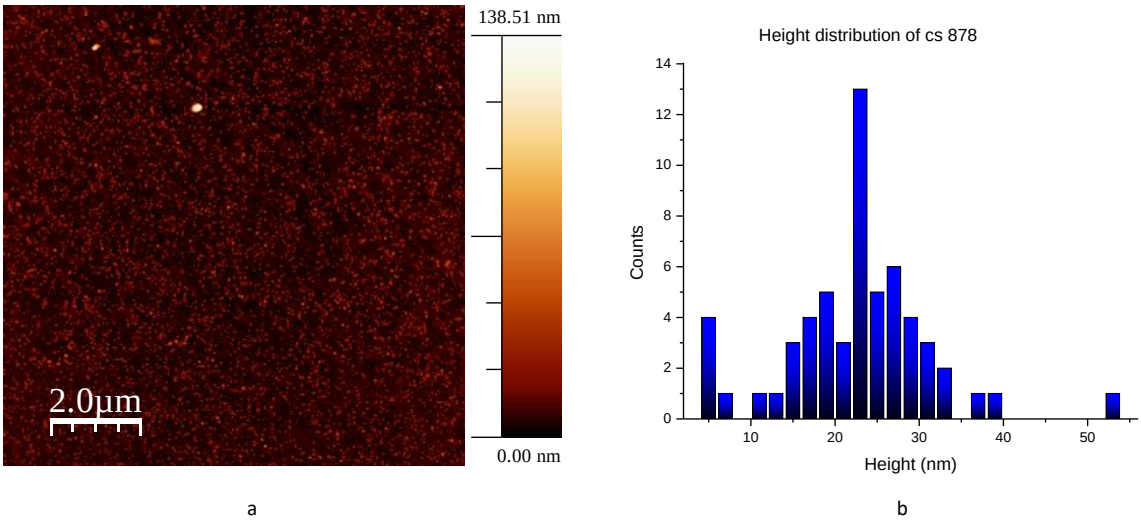

Figure 4.2.18: AFM image a) and particle height distribution histogram b) of cs 878. The surface density is $58\ particles/\mu m^2$ making a quite dense deposition. Particles of size around 22 nm are the highest in amount making them the dominant particle height. The selected square for the counting of the particles was 1x1 µm.

The distribution is slightly uneven making the determination of the dominant particle height trickier. We can consider the dominant particle heights to be ~22 nm by noticing the peak in the histogram, and 20 nm and 30 nm as these are the next highest in amount. A particle that can be seen in the upper half of the image is too large and causes the z color scale to indicate 138 nm as maximum height. The distribution was calculated for a 1x1 µm square selected to count the clusters and measure their height.

Si thickness 100 nm

The second sample made with the thickest Si film is cs 880. The aggregation length was again 40 mm and the power was 62 W. The deposition time was 30 min. The result was a sample similar to cs 879 but with very few small particles (<10 nm). The optical measurements performed with the UV-Vis spectrometer are very interesting as we will see in figure 4.3.4.

In the experiments both total reflection and transmission difference exhibit two peaks as is the case for simulations. The highest peak in total reflection can be seen at 723 nm, and the maximum value is 1.56 % .The peak is wider than in simulations, its FWHM being 195 nm. At 535 nm we can see the lower peaks where the total reflection has value is -0.5 %. The simulations predict high peaks for the three

different sizes at 733 nm, which makes the agreement with the experiment excellent. This is the case for the lower peaks as well which can be seen at 541 nm. The high peak is positive in both the experiments and the simulations. The experimental graph is positive in the range 607 nm to 789 nm while the simulated is positive for a shorter range, from 683 to 834 nm.

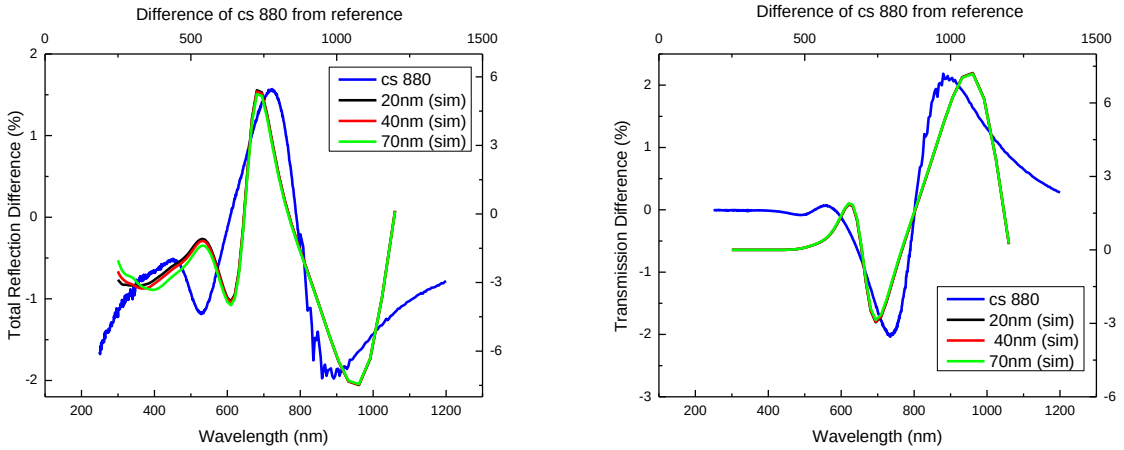

Figure 4.3.4: Total reflection (a) and transmission (b) differences a function of wavelength for cs 880 together with simulations. In both an and b the experiments match the simulations perfectly.

This very good agreement does not apply for transmission however although it is still adequate. Looking at the graph in figure 4.3.4(b), we observe two peaks. A high peak at 884 nm where the difference is 7.09 % and its FWHM is 291 nm, and a lower at 565 nm where it has a value of 0.06 %. The FWHM for the low peak is 244 nm. The two peaks are in the simulations as well but they are shifted towards infrared. The high peak can be seen at 1071 nm and the low peak at 654 nm for all three particle sizes. Experimental and simulated graphs behave similarly regarding the parts of the spectrum that they take positive or negative values.

In figure 4.3.5 we can see the graph of the absorption difference. Its local maxima are 1.19 % , and 0.74 % positioned at 525 nm and 770 nm respectively indicated by the peaks in the graph. For the most part of the spectrum the absorption difference is positive, indicating that the sample absorbs more light than the reference in general. Negative values are present in a small range of 838 nm to 960 nm. At 886 nm the graph takes the lowest value which due to the noise in the signal it is roughly estimated at-0.2 %.

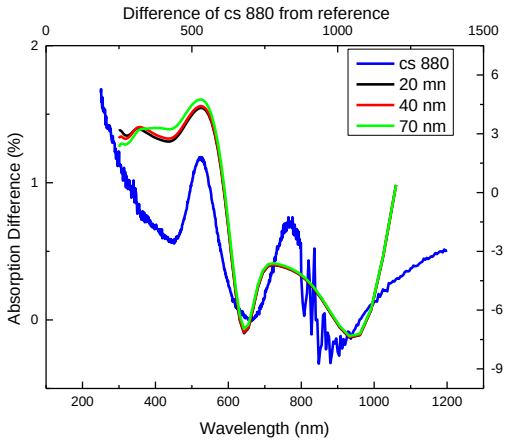

Figure 4.3.5: Absorption difference as a function of wavelength The absorption shows two peaks positioned at 525 and at 770 nm which give local maxima of 1.19 % and 0.74 % respectively.

The AFM image is shown in figure 4.3.6a. The sample contains a dense layer of large clusters that measure from 30 nm to over 120 nm, with the most encountered heights being above 50 nm and 60 nm. As expected the surface density is high measuring 50 particles/μm^2. The distribution was calculated as usual by selecting a 1x1 µm square, in which the clusters where counted and measured in height.

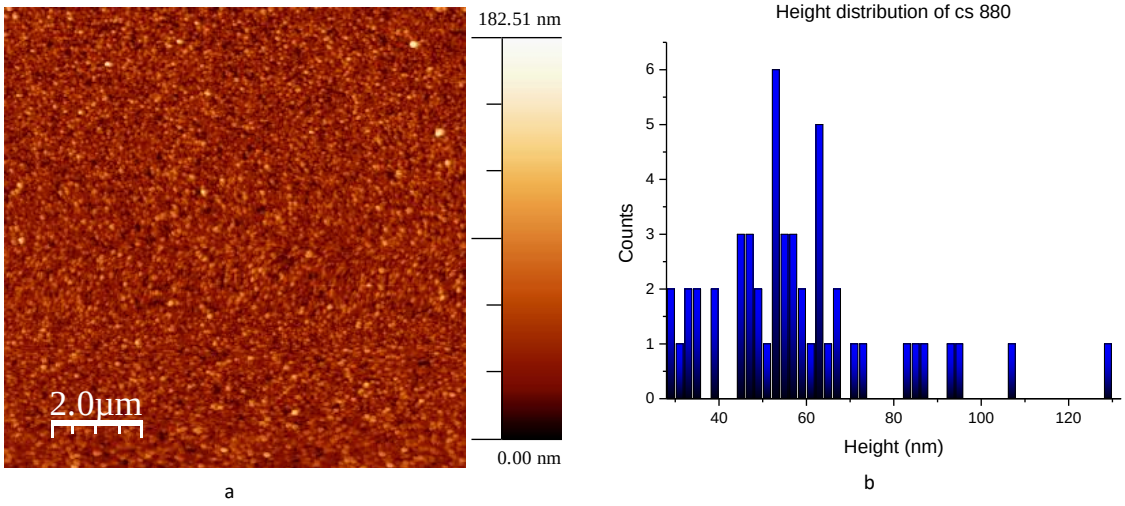

Figure 4.3.6: AFM image (a) and particle height distribution histogram (b) of cs 880. The histogram shows a dominant particle size of 30 nm to >120 nm. There are one or two particles higher up to 182 nm as seen in the z scale attached. The histogram was creating by counting the particles in a selected square of dimensions 1x1 µm.

In the histogram we can see a maximum height of 37.5 nm, while the z scale attached next to the AFM image goes up to 56 nm. This is due to the fact that there are always one or two stray particles in the scan

that measure higher than the rest. To make the particle height distribution, as before, we counted particles in a selected square of 2x2 μm.

The sample cs 884 was created using the same cluster source parameters as in cs 883 but with lower power of 52.3 W. The deposition yielded numerous particles making a dense layer visible with the naked eye. Experiments showed interesting results presented in the following picture.

As was the case in cs 883, total reflection difference has small bump that can be identified as a peak at 746 nm where its value is 0.14 %. Again the graph is entirely negative excluding a small interval between 705 nm and 762 nm where its maximum point is located. The agreement with the simulations is good regarding the position of the peak (733 nm for the simulations) and the fact that the graphs are negative for the most part in both cases, constituting a higher reflection in the reference than in the sample.

The graph of picture 4.4.8b shows us the transmission difference. In the UV range is zero and at 480 nm increasing maximizing at 684 nm giving a value of $0.96\ \%$. Then it starts decreasing becoming negative and reaches a minimum at 831 nm creating a deep valley. The minimum value is roughly estimated to be $-1.68\ \%$ due to the noise present. The FWHM of the peak is 240 nm. The experimental results are in a fairly good agreement with the simulations, showing however two peaks. The smaller peak agrees well with the experimental appearing at 660 nm. The valley is shifted by 100 nm approximately.

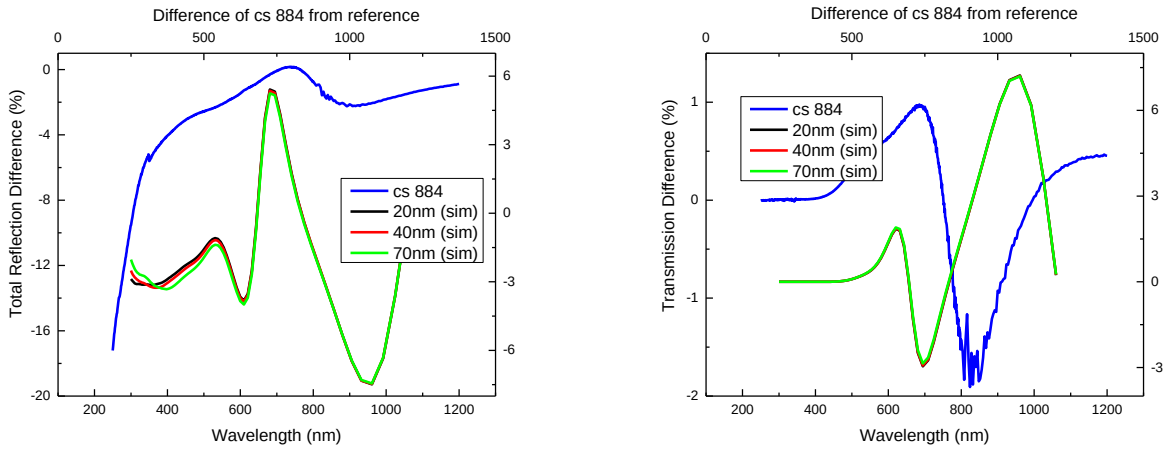

Figure 4.3.10: Total reflection (a) and transmission (b) difference for cs 884. The blue line is for the experimental results and the green, red and black for the simulations. The total reflection peaks at 747 with a not very clear peak. The peak of transmission can be seen at 684 nm.

The experimental peak however is 240 nm away from the simulated, which is located at 1071 nm. The small peak observed in simulations at 654 nm is also not present in the experimental results. Most of the experimental graph is positive as is the case in simulations, which indicates a higher percentage of transmission in the sample. Initially the results of transmission were much less agreement with simulations.

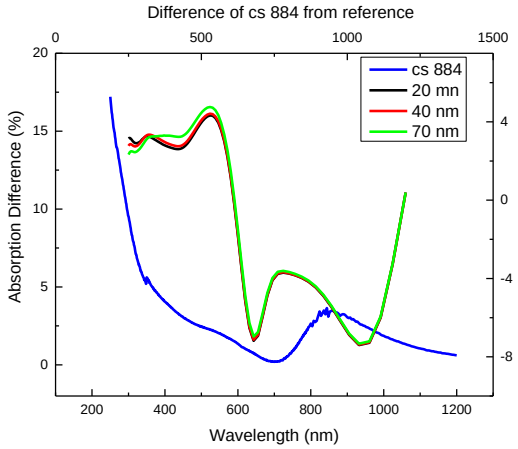

Figure 4.3.11: Absorption difference as a function of wavelength for cs 884. The graph is positive for the entire part of the experimental spectrum and shows a peak at 855 nm where a local maximum is reached with a value of 3.5 %.

Figure 4.3.11 depicts the absorption difference of sample cs 884. The absorption is positive in the entire experimental spectral range. The minimum point is observed at 700 nm where the difference is 0.1 %. A small peak follows, located at 855 nm and the graph gives a local maximum of 3.5 %. A is the case in many samples the graph starts from the highest value continuing with a steep decrease in the UV range and at 1200 nm tends to zero. The fact that the graph is positive in the entire spectral range shows that the sample absorbs more than the reference due to the presence of the nanoparticles.

Completing the information needed for this sample the scan of the AFM microscope is depicted in figure 4.3.12, and the height distribution histogram. It is evident from the image in (fig. 4.3.12a) that there are a lot of large, that is greater than 50 nm, particles here. In some cases they surpass 100 nm. The surface density is as anticipated high measuring 54 particles/μm^2. The variety in sizes combined with the high density likely results in more than one effects happening simulataneously.

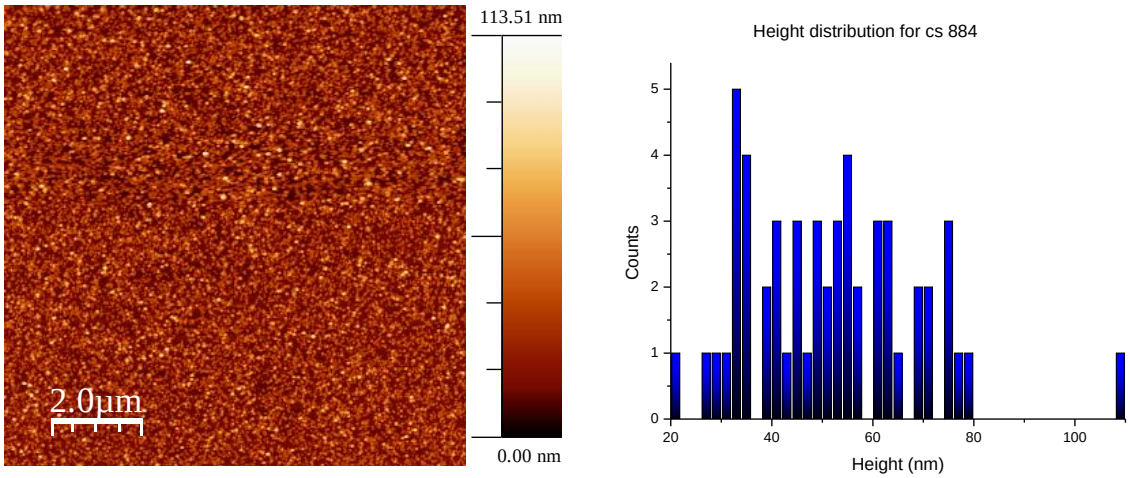

Figure 4.3.12: AFM image (a) and particle height distribution histogram (b) of cs 884. The histogram bin size is 2 nm. The histogram has many peaks making, so the main particle size would be the highest peak that is 32nm-33 nm.

The next sample is cs 886 made as a replacement for cs 882. Sample cs 882 failed to provide adequate measurements, possibly due to very low particle density. Again a 30 minutes long cluster deposition was performed, using 40 mm aggregation length and 0.163 A current. The interesting part with this sample is that it has two different graphs for total reflection.

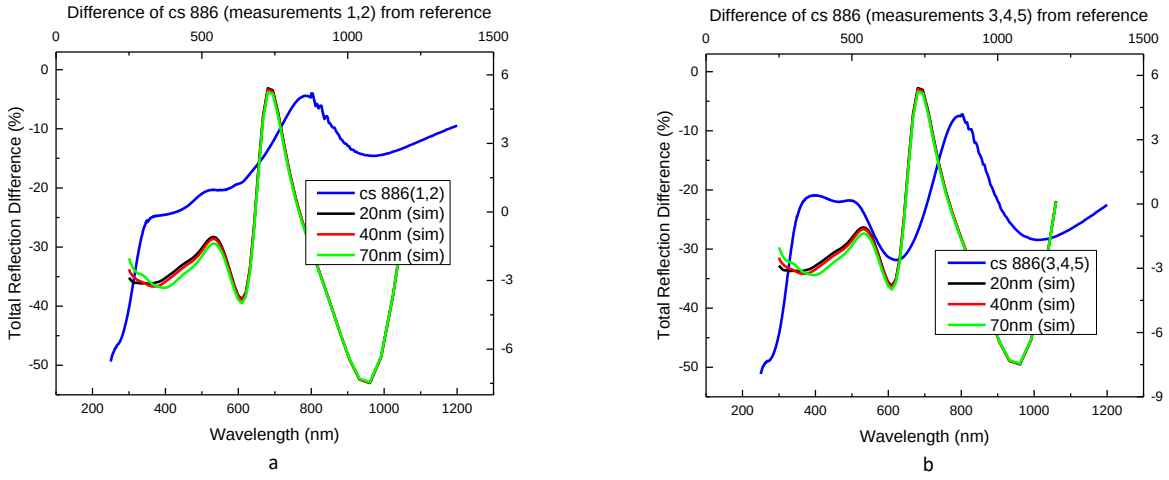

Figure 4.3.13: a) Total reflection difference for cs 886 taken from the two (1,2) first measurements, b) total reflection difference for the remaining three (3,45) measurements taken. Although the sample is the same with different positions we had slightly difference graphs.

The reason is that during the optical experiments, two different line shapes were obtained within three sample positions. So it was decided to make another extra two measurements in different positions. The two graphs are shown in figure 4.3.13.

A total of five measurements were taken for this sample, each with a different position of the sample on the beam. The graph shown in figure 4.51a is typical to the trend that seems to be followed by the samples that have high particle density.

The peak is more prominet compared to the other samples and it is located at 784 nm, only a slight shift of 50 nm towards infrared compared to the simulations. Also a very small bump is noticeable close to the position where simulations expect the low peak. The second set of measuremetns resembles a lot more the shape of the simulated reflection. The high peak is sharper with a FWHM of 337 nm, and can be seen at 803 nm. The lower peak seems to be a conjunction of two peaks. The position agrees well with the simlations beeing at 500 nm. In both cases the difference is negative everywhere i.e. the reference reflects more than the sample.

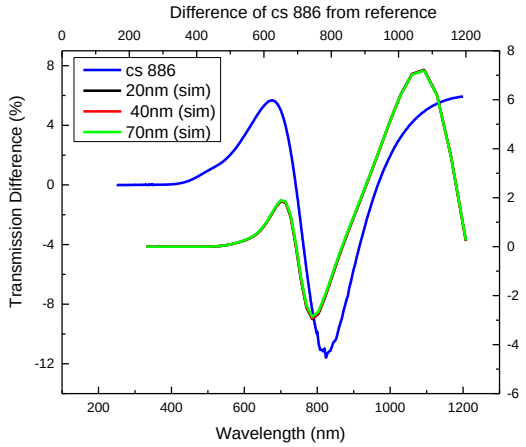

Figure 4.3.14: Transmission difference for cs 886. One clear peak is at 672 nm and a second not complete at 1200 nm where it maximizes.

Figure 4.3.14 shows the transmission difference with the simluations as always included. The peak of the experiments is positioned at 671 nm and its FWHM is 168 nm. It matches perfectly the lower peak observed in the simulations at 654 nm. At 1200 nm the graph apparently has a second peak where it reaches its maximum which is 5.6 % although it is not complete since at 1200 nm is the limit of our experimental range. Compared to the simulations this peak is shifted by 129 nm, but overall the agreement is very good taking into account the first peak ant the fact that both graphs start from zero minimize afterwards and they reach their highest point right after in positions that are relatively close.

As expected there are two graphs for the absorption difference. It can be seen clearly that the second graph (fig. 4.3.15b) has two distinct peaks while the first (4.3.15a) shows only one. In figure 3.54a the difference shows a minimum value of 7.12 % at 713 nm. A peak is present at 858 nm where the graph is locally maximized with a value of 19.32 %. In b) the minimum is located at 753 nm and gives a value of 15.18 %. Figure 4.3.15b shows that the absorption has two peaks, one at 600 nm and one at 925 nm giving local maxima of 28.65 % and 28.14 % respectively. In both cases the difference of sample from the reference is positive in the entire range, indicating greater absorption in the sample, either by the clusters or the Si film. The initial high difference in the UV range is present in both graphs

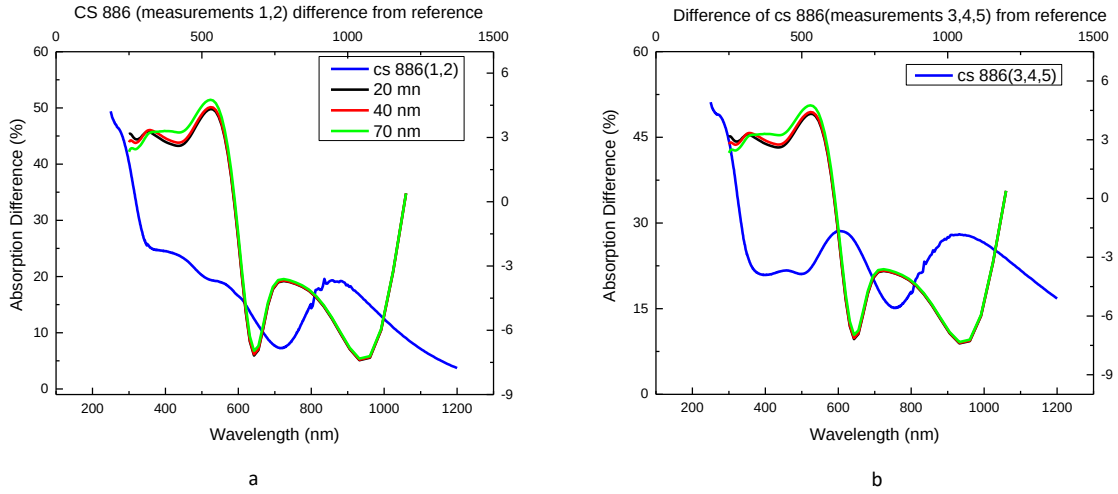

Figure 4.3.15: Absorption difference for cs 886: a) for the first two (1,2) measurements and b) for the remaining three (3,4,5). The behavior of the above graphs is significantly different compared to the rest of the samples. In a) the graph exhibits a valley at 713 nm and a peak at 862 nm. In b) peaks are present at 600 nm and 925 nm.

Figure 4.3.16a depicts the AFM image of the saple. The surface density is very high and the particles are the largest we encountered in the whole series of samples measuring up to 176 nm in height. The great height and density of the particles, increases the roughness of the of the surface making the capture of a nice clear image a challenging task, so a lot of scans were performed until we get the better one. Nevertheless the information we need can be provided.

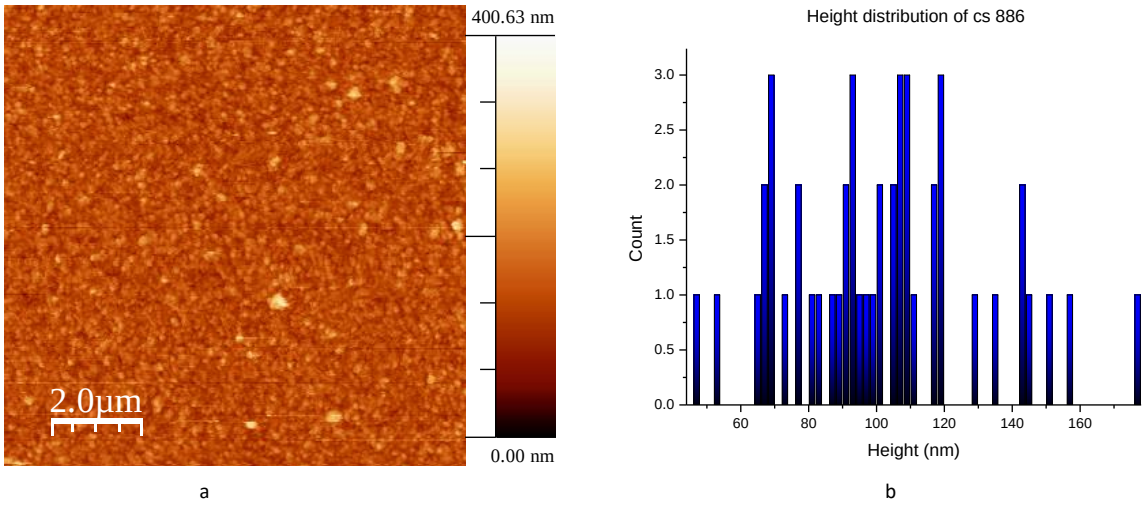

a b

Figure 4.3.16: AFM scan image (a) and height distribution histogram of cs 886. Some lines are visible and is due to the high roughness of the surface making the microscope tip bounce off. The particles are greater than 45 nm and are going up to 177 nm.

The above figure makes the current sample the different from the rest of the series. The histogram shows four major peaks of the same height, which tells us that there are four dominant particle sizes, lying in the ranges 67 nm to 69 nm, 90 nm to 93 mn, 105 nm to 109 nm, and 115 nm to 119 nm. We notice again that the z color scale attached next to the image is reaching 400 nm. This is due to the overly large stray particles appearing once or twice in a scan. To create the histogram, a square 1x1 µm in dimensions was selected and the particles were counted. This yielded a surface density $\sigma = 50\ particles/\mu m^2$.

Next sample is cs 887 and belongs to the repeated ones. The paratmeter setup for the cluster source deposition was the same as before. The particles were only slightly lower than the precious sample and the density was higher.

Figure 4.3.17 shows the resulting graphs of total reflection and transmission difference of the sample from the reference. Total reflection difference (fig. 4.3.17a) first exhibits a faint peak at 465 nm 90 nm away towards UV, from the FDTD predicted and then maximizes at 729 nm almost exactly at the same point as the simulated. Its value at this point is 2.3 % and is broader than the simulations, having a FWHM of 327 nm.

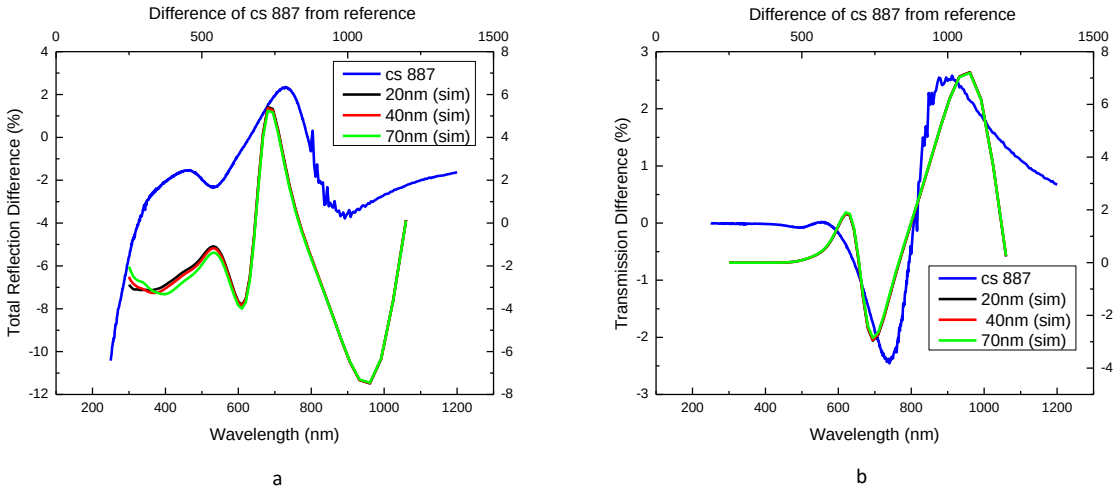

Figure 4.3.17: Total reflection a) and transmission b) difference per particle for cs 887, with simulations. The agreement with the simulations appears to be good. The reflection exhibits a high peak at 729 nm and the transmission at 912 nm.

Transmission follows the trend of the simulations beeing zero at the beginning then a very faint, barely noticeable bump follows at 558 nm. This is almost 100 nm away from the simulated low peak (654 nm). The maximum point of the graph is at 1000 nm, compared to the 1071 observed in the simulations.

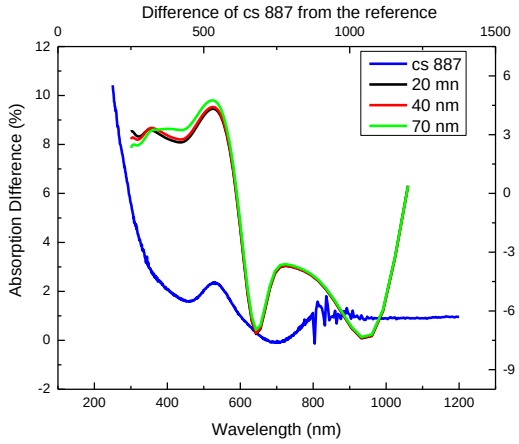

Figure 4.3.18: Absorption difference of cs 887. Absorption shows a small peak at 530 nm taking local maximum value of 2.41%, followed by a valley at 690 nm. The minimum difference is -0.13%.

Figure 4.3.18 shows the graph of the absorption difference. The sample absorbs more light than the sample except in the range 675 nm to 782 nm where the graph negative and approaches zero with a minimum value of -0.06 % at 690 nm. The small peak is positioned at 529 nm where it gets a local

maximum value, which is 2.41 %. The difference as usually starts from the highest value and exhibits steep decrease in the UV range.

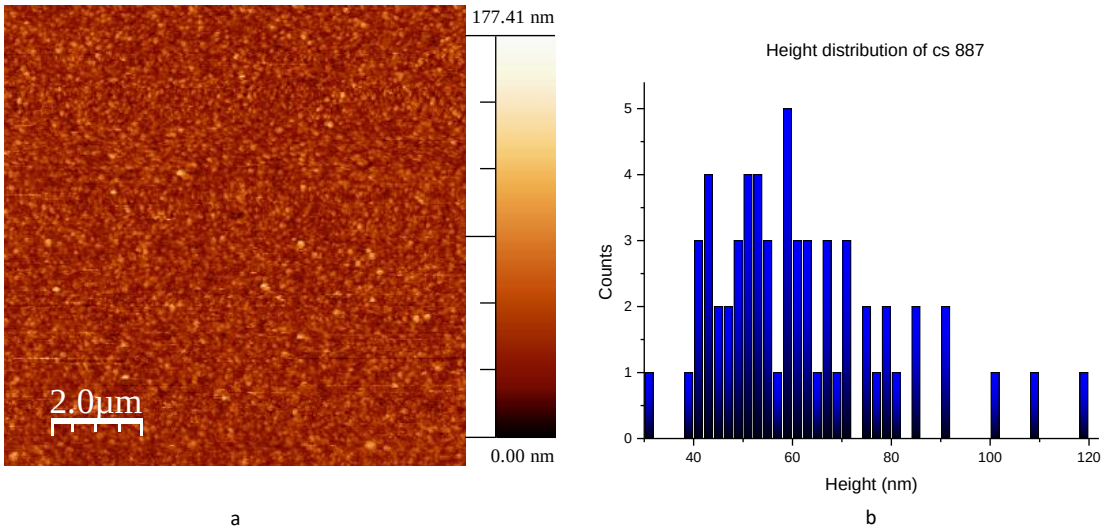

Figure 4.3.19: AFM scan a) and height distribution histogram b) for cs 887. Very dense deposition created a uniform layer of particles with a surface density of 60 particles/µm2. The scan size is 10x10 µm and the area selected for the counting was 1x1 µm.

The AFM scan image shown in figure 4.3.19 a) shows a very dense, uniform layer of particles with a surface density of $60\ particles/\mu m^2$. Looking at the histogram we can see that the particles are large in general since the overall height range is from 35 nm to 120nm and higher in some cases. The dominant heihgt is 60 nm. The counting was done by selecting a 1x1 µm square.

Sample cs 888 was created also with the same cluster source parameters. However the particles were not as large as in the previous two samples.The experimental results of the reflection and transmission difference are shown in figure 4.3.20.

At 867 nm where the peak of total reflection can be seen, we see that the difference is negative and becomes positive at 790 nm, so for this part of the spectrum the sample shows increased reflection. The maximum is observed at 867 nm and its value is 3.34 % forming a broad peak with a measured FWHM of 203 nm. The simulations agree very well with te experiment since the predicted peaks are located at 733 mn. The small step observed at 443 nm can be related to the lower peak exhibited in the simulations at 541 nm. Overall the graph behaves very similarly to the simulations forming valleys near the ones observed in the simulations making a good match. The experimental valleys are located at 529 nm and 866 nm and the corresponding simulated ones at 630 nm and 1071 nm respectively.

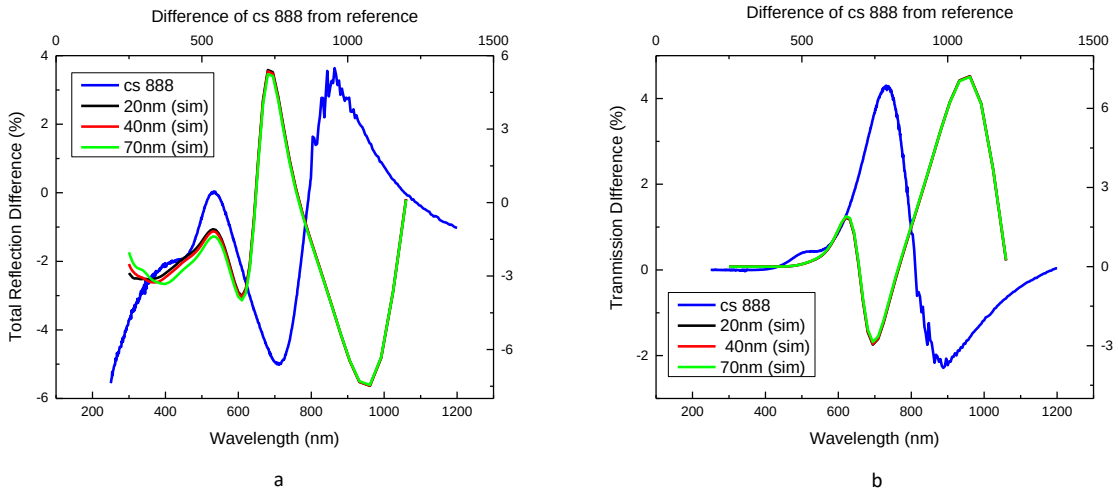

Figure 4.3.20: Total reflection a) a transmission b) difference per particle for cs 888 with simulations. The peak of the reflection can be seen at 867 nm were the reflection is 3.34 %. The transmission shows only one peak at 886 nm. The maximum value of transmission difference is 4.3 %.

The difference of transmission (fig. 4.3.20 b) shows only one clear peak, much like what was observed in samples 879 and 883. It is located at 733 nm. The difference maximizes there with a positive value of 4.3 % The FWHM of the peak is 190 nm and the fact that is positive indicates enhanced transmission due to the presence of the particles. Once again the agreement between experiments and simulations is not as good as in the reflection. The experimental peak is located 338 nm closer to UV than the simulated which is at 1071 nm. The graphs are behaving in the same way in both cases except the fact that the lower peak observed in the simulations at 654 nm is not visible in the experiment as is the case with the sampels 879, 884 and 887. However the step in the graph at 514 nm could be interpreted as the smaller simulated peak indicating a possible merging of the two peaks predicted in the simulations.

The step at 514 nm gives a local maximum giving a value of -0.47 %. The deep valley at 831 nm is where the graph gives its minimum value which is approximately -2.36 % since the noise makes diffucult the determination of the precise value.

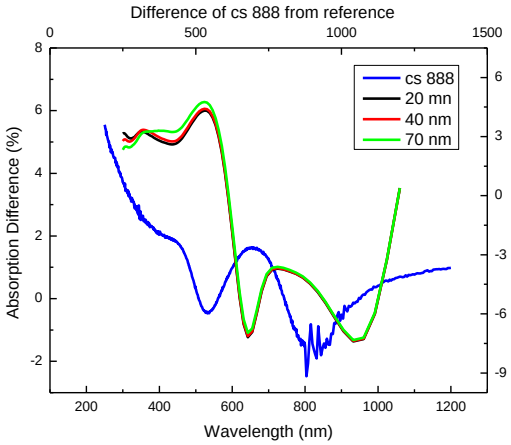

Figure 4.3.21: a) Absorption difference for cs 888. The peak is located at 655 nm giving a maximum of 0.66 %. The valleys are located at 533 nm and 831 nm.

Figure 4.3.21a shows the absorption difference. The graph is mainly positive except from the ranges 509 nm to 555 nm, and 745 nm to 937nm. It starts from a maximum value at 250 nm decreasing exponentially until 455 nm where it becomes steep. It forms a peak at 655 nm, where the difference is 0.66 %.

It can be seen in the AFM image depicted in figure 4.3.22a that the amount of particles deposited is very high. The surface density is 66 particles/μm^2. According to the histogram (fig. 3.61b) the particles large but do not reach the >120 nm heights encountered in samples cs 886 and 887. Here the dominant size lies in a range between 35 to 45 nm. Less frequent larger particles measuring up to 79 nm, are present creating a discontinuity in the histogram. The bin width is 2 nm.

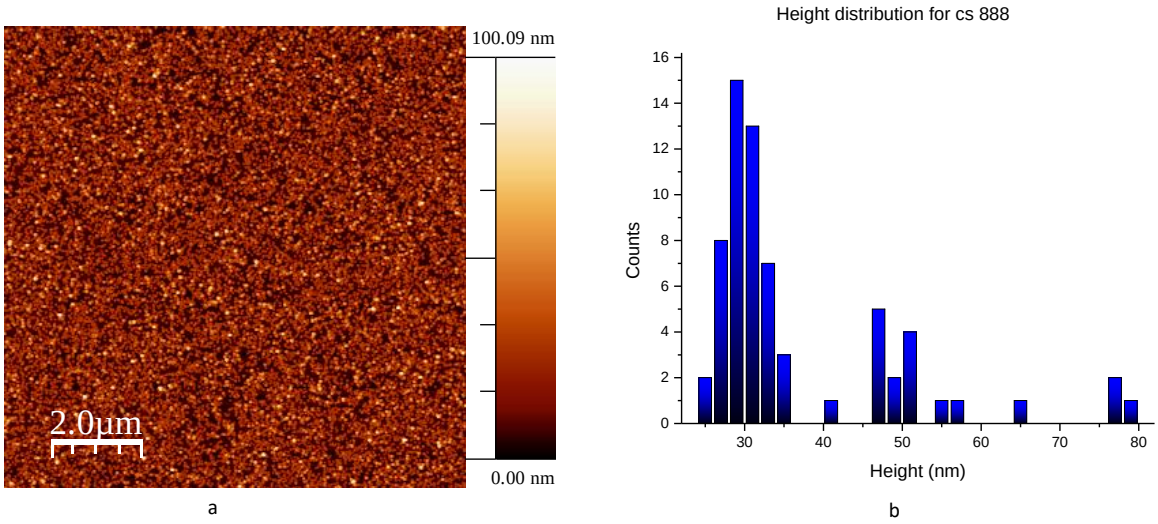

Figure 4.3.22: AFM scan image a), and height distribution histogram of cs 888. The scan size is 10x10 µm and the square selected for the counting of the parties was 1x1 µm. The main particle height ranges from 35 to 45 nm.

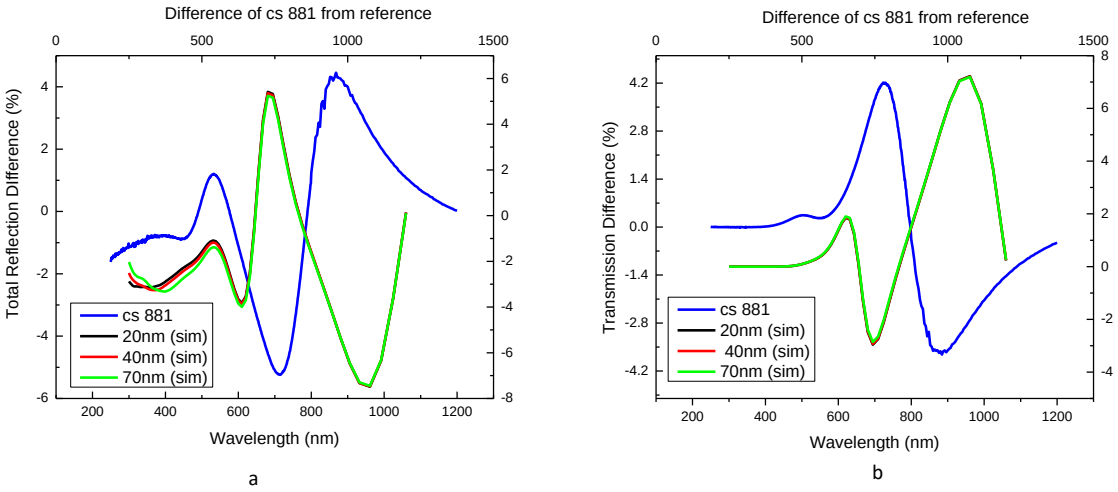

Figure 4.3.23: Total reflection a) and transmission b) difference for cs 881. The experimental results are represented by the blue line and the simulations for different particle size, by the green, red and black line. The sign of the experimental results was reversed.

Figure 4.3.23a shows the total reflection difference measured for sample cs 881. The cluster source deposition was 30 minutes long. The aggregation length was 40 mm and the current 0.163 A. At 866 nm it gets the maximum value which is 4.4 %. The FWHM is 200 nm, slightly broader compared to the simulations. The position of the peak is shifted compared with the simulations (733 nm). The lower peak is located at 541 nm which is in very good agreement with the peak predicted by simulations and gives a local maximum of 1.83 %. The FWHM of the lower peak is 215 nm. The transmission as shown in figure 4.3.23b exhibits only one peak at 725 nm, in between the two peaks depicted in the simulations. The peak's FWHM is 204 nm and the difference is 4.21 %. FDTD predicted for all different sizes peaks at 654 and 1071 nm. One quick inspection we could consider the peak as the physical counterpart of the lower peak observed at 654 nm in the calculations, since their positions in the spectrum are very close to each other. However the small step at 500 nm in the experiments could be indentified as the small peak, and could mean that in the epxeriments the peaks are shifted towards UV. Moreover the step could indicate a merginf of the two peaks. One clear first impression is that these measurements are very similar to the ones of cs 879.

The graph of absorption looks a lot like what we observed for cs 879. Exhibiting two valleys, a deep one at 529 nm where the difference is minimum (-1.51 %). and a shallower one at 827 nm. During the period where the valleys occur the graph is negative. After and between these intervals it becomes positive again and peaks at 670 nm where the maximum difference occurs and its value is 1.55 %.

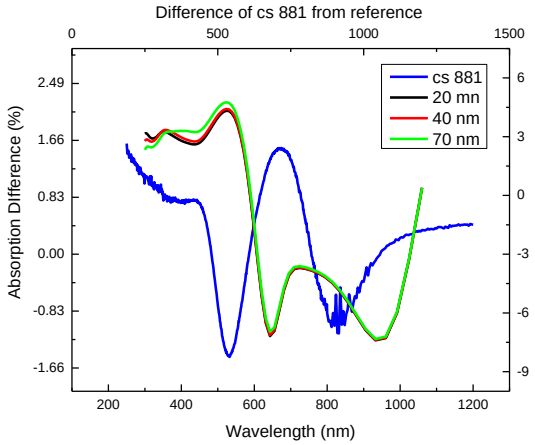

Figure 4.3.24: Absorption difference for cs 881. The peak is at 670 nm where the difference is 1.55 %. The deep valley is at 529 nm. The minimum value is -1.51 %.

We complete the investigation of this sample by examining the information about the density and height of the particles deposited. It is obvious from the AFM picture (fig 4.3.25a) that there are much fewer particles here and are small (<25 nm). The most counted particles are those that measure 21 nm. The z color scale indicates a maximum height of 48 nm that may be reached by one particle in the whole scan. The distribution of height was calculated by selectinf a 2x2 µm square in the scan, and counted the clusters one by one. The density is 16 particles/μm^2.

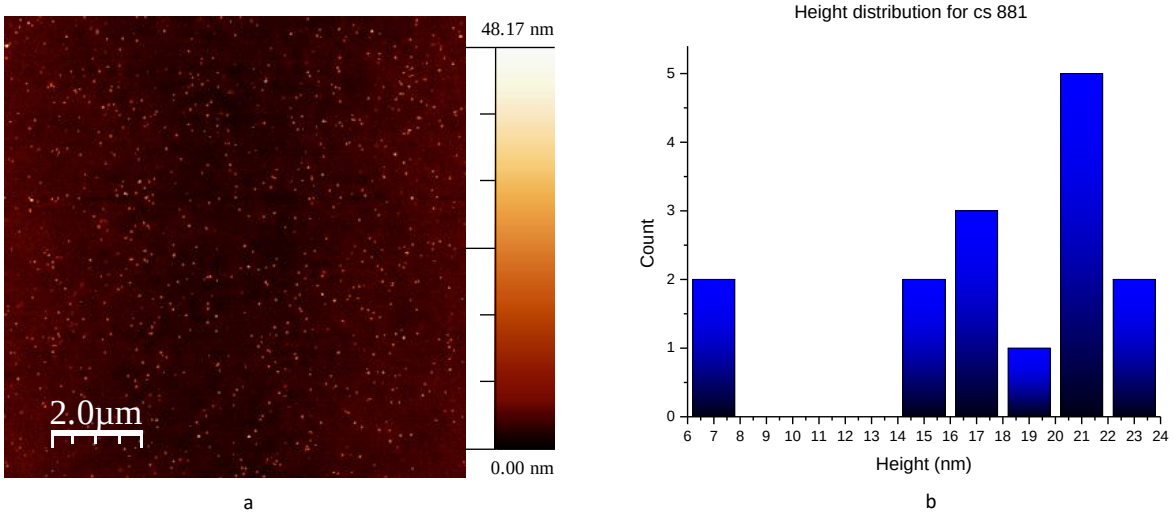

Figure 4.3.25:AFM scan image a), and height distribution histogram b) of sample cs 881. At a maximum of 24 nm the particles are small, and the density is low. To count the particles a 2x2 µm square was used. The bin width is 2 nm.

Silicon nitride films

SiN thickness 37 nm

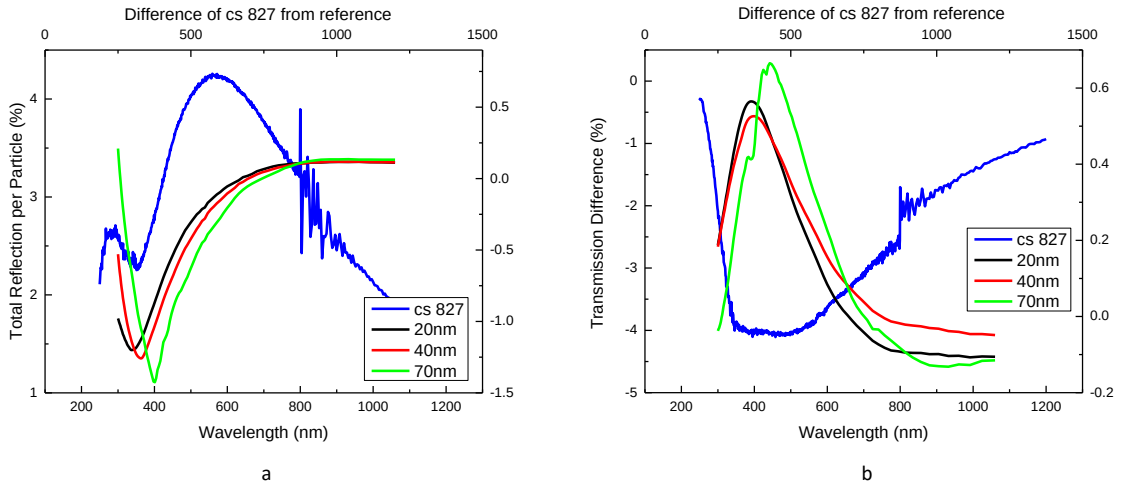

Figure 4.4.4: Total reflection a) and transmission b) difference for cs 811 with FDTD simulations. The blue line is for the experimental results and the green, red and black for the simulations. As with the precious sample total reflection is everywhere positive with a broad peak at 592 nm and transmission everywhere negative showing a valley at 400-500 nm.

Sample cs 827 is the second one of the series, and was created with the same parameters except aggregation length which was 40 mm. It is a re-deposition on a previous sample that had very low amount of particles. The optical measurements of reflection and transmission yielded very similar results with the previous sample as shown in figure 3.2.4. The peak is at 592 nm and the difference at this point measures 4.27 %. The difference is well above zero for all the experimental spectrum. The transmission difference follows the same trend as cs 811, being everywhere positive and exhibiting a peak. What is slightly different though is the shape of the pak in the graph . In contrast to cs 811 the valley is flattened and broad, being in the range 400 to 500 nm. The signal at this part of the graph is noisy so it creates some inaccuracy in the determination of the minimum value, which is -0.55 % at 486 nm.

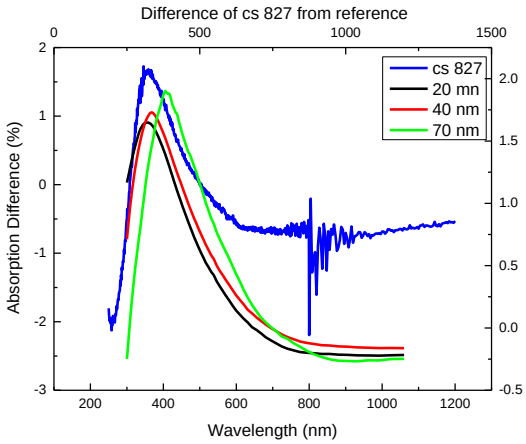

Figure 4.4.5: Absorption difference for cs 827. The graph peaks at 359 nm where the difference maximizes giving 1.7 %.

Figure 4.4.5a shows the absorption difference per paticle. It forms a sharper peak compared to the one of cs 811 and is positioned at 359 nm. The maximum value is 1.7 %. Overall it behaves the same as in the previous sample. The general similarity was anticipated, since the clusters deposited as we will see in the following pictures are once again very small.

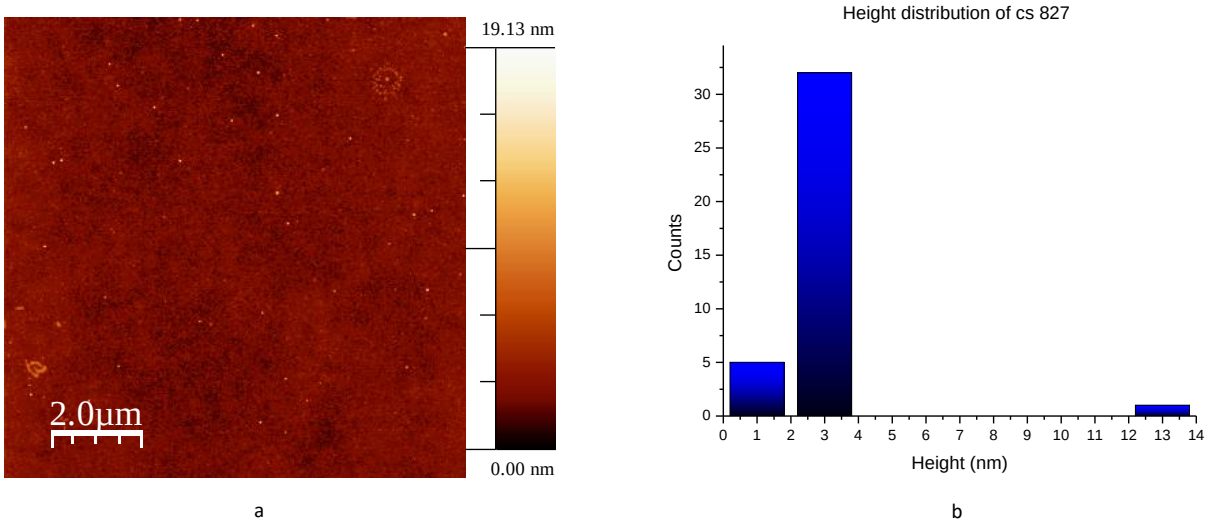

Figure 4.4.6: a) AFM scan image of c s827. b) Particle height distribution histogram. The distribution shows main height at 3 nm. The circular particles observed in the scan were observed also in later samples. The selected square was 1x1 µm. The scan size is 10x10 µm.

In figure 4.4.6a the AFM image of the sample is shown. The particle density is 36 particles/μm^2 slightly lower than cs 811. The majority of the particles measures 3 nm in height and 10 nm are surpassed in only few occasions. The sample has some interesting features, as we can observe a circular like particle near the top right corner of the image. Such features were also encountered in some of the samples of the next series.

Si_3N_4 thickness: 68 nm

Finally, the results of the two samples made with the thickest film of 68 nm are presented in this section. The depositions were 10 minutes long in both samples and the aggregation lengths used were 40 mm for cs 824 and 20 mm for cs 825.First the results of the optical measurements of reflection and transmission for the reference sample are presented. First the results of cs 824 will be presented. Oxygen was additionally used for the deposition in a gas flow of 0.8 sccm. The power was 54.5 W. Total reflection and transmission differences are plotted in figure 3.2.14.

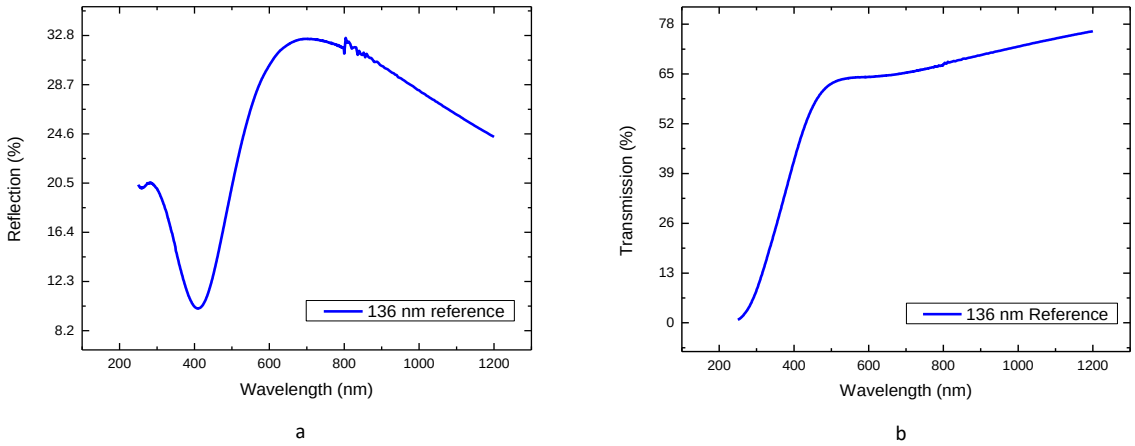

Figure 4.4.1: Total reflection a) and transmission b) optical measurements for the reference sample. The measurements are unprocessed. The wavelength ranges from 250 nm to 1200 nm.

The difference graph for total reflection is in a very good agreement with the simulations as we can clearly see in figure 4.4.16a. The experimental peak is located at 465 nm, it has FWHM 202 nm and it is where the difference is maximum giving a value of 3.34 %. In the simulations the peak is positioned at 493 nm which is an excellent match. They differ only in their shape after the peak, since in the simuations the difference starts to increase at 650 nm. There is no size relation to the position of the peak in reflection, since all three graphs are entirely overlapping. Figure 4.4.16b depicts the transmission difference . Exeprimental results (blue line) are peaking at 375 nm giving 0.16 % difference. The peak's FWHM is 137 nm. The simulation results now are quite different as we can see two peaks. The surprising factor is that now the results o the simulation show great particle dependence, mainly in the difference and not as much in the position of the peaks. The 70 nm particle has its first peak at 517 nm and the second one at

777 nm. As the size decreases the peaks shift slightly towards UV, by 44 nm at most (40 nm cluster second peak).

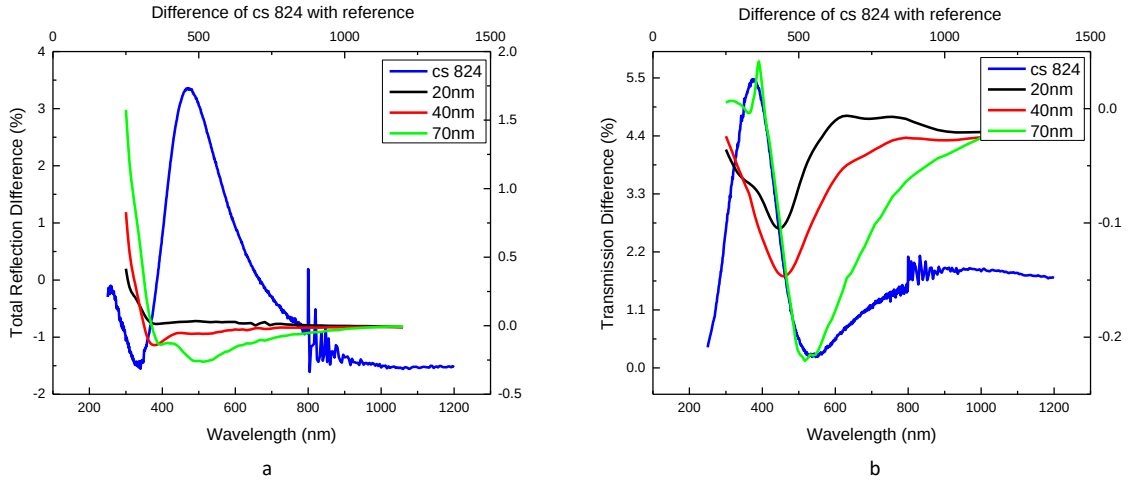

Figure 4.4.16: a) Total reflection difference per particle and b) transmission difference per particle including simulation results. Experimental total reflation agrees well with the simulations showing peak at 465 nm.

Figure 4.4.17 shows the absorption difference for the current sample. It is aslway negative and no peak is existent, instead it exhibits a valleyat 415 nm were it is minimized taking a value of 6.08 %. The AFM image and particle distribution histrogram are shown in figure 4.4.18. The particles deposited here are as with cs 826 forming crater-like structures as we can see in figure 4.4.18a. Once again the height of the clusters is very small with the main height being in the range 2-6 nm and some few measuring around 15 nm. As it can be

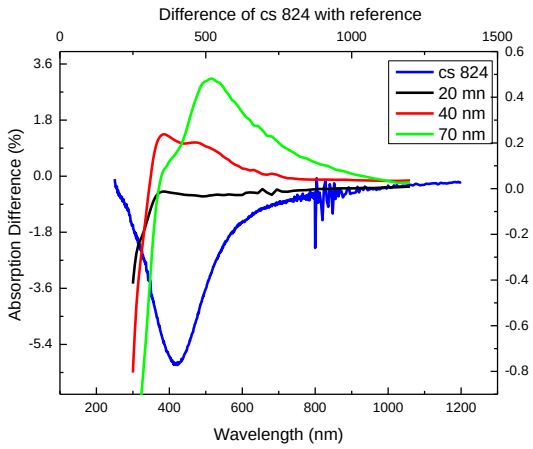

Figure 4.4.17 Absorption difference for cs 824. A valley can be seen at 415 nm similar to the results of most of the samples. The minimum is -6.08 %.

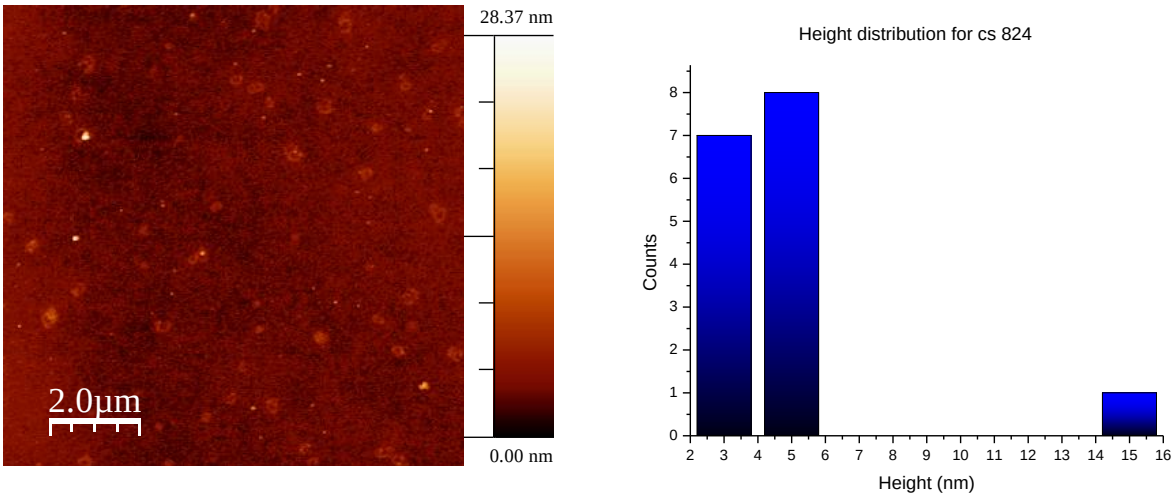

Figure 4.4.18: AFM scan image a) and height distribution histogram b) of cs 824. The main size lies in the range 2 nm – 6 nm. The z indicates 28 nm maximum height due to one bigger cluster at the upper left part of the scan.

The density is very low with only 7 particles/μm^2. The larger cluster near the upper left corner was exluded from counting. Additional scans were made zooming-in at the craters for further investigation. The two best images are shown in figure 4.4.19.

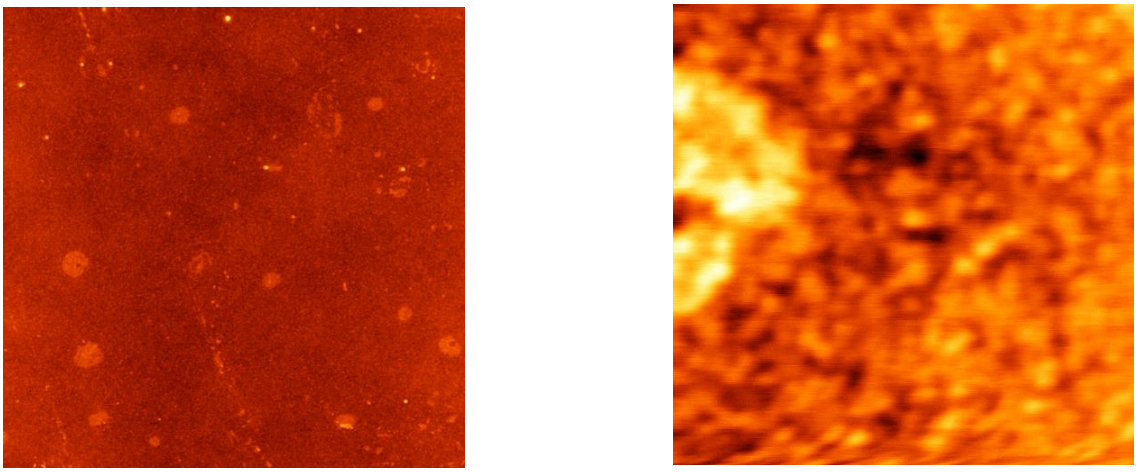

a b

Figure 4.4.19: a) Zoom-in showing several of the crater-like clusters, b) zoom-in in one of the clusters. The cluster appears only half in the images due to inaccuracy of the position of the tip.

The final sample is cs 825 and was made using 20 mm aggregation length. Only Ar gas was used at a gas flow of 20 sccm. The deposition was 10 minutes and the power 59.52 W. The results of the experiments are slightly different from the previous sample. In figure 2.3.18 the total reflection and transmission difference per paticle are plotted. The total reflection difference graph cannot provide us

with clear information due to extensive noise. The local maximum point of the graph is at 431 nm where the difference is $-1.00 \cdot 10^{-9}$ % (fig. 4.4.20a). It is difficult to distinguish peaks which appears to form at this point.

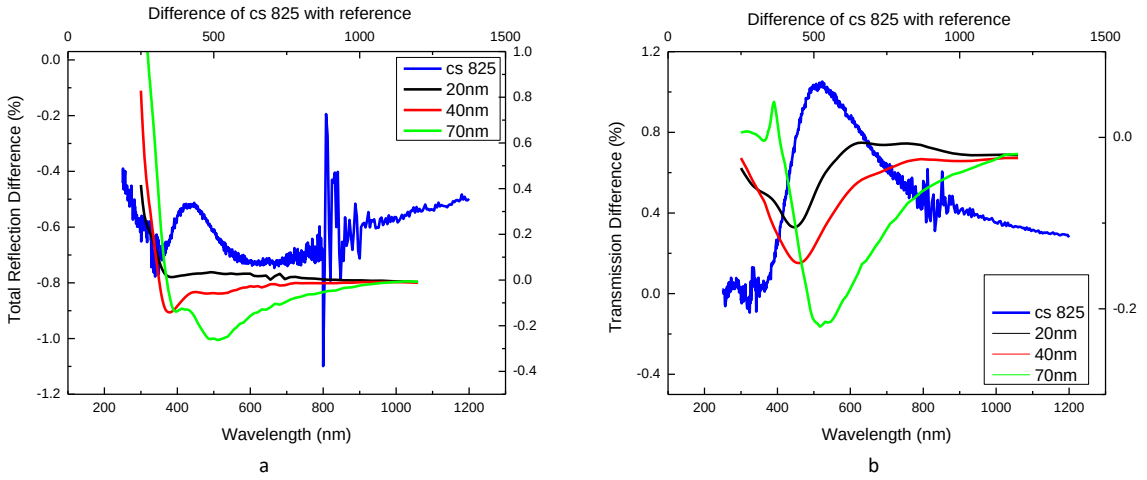

Figure 4.4.20: Total reflection a) and transmission b) difference per particle for cs 825. The simulations are included and show a fairly agreement with the experiments, especially transmission. The sign of the experimental results was reversed in both graphs.

Another slightly smaller peak, or feature that can be identified as a valley is located at 353 nm. It is obvious that the experimental results do not agree so well with the simulations in this sample regarding the behaviour of the graph. The shape of the graph could be considered similar, since it starts from high values and a minimum afterwards as observed in simulations.

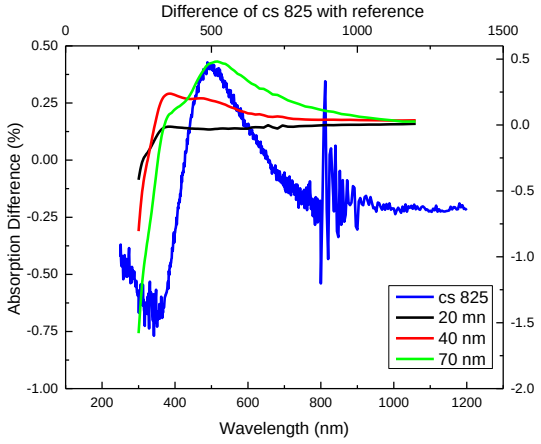

Figure 4.4.21: Absorption difference for cs 825. The peak is at 500 nm and the maximum value is 0.42 %. The graph is positive in the range 428-710 nm.

As was the case for the previous samples simulations and experiment show different as a result instead of valleys peaks appear. The transmission difference shows a peak at 517 nm and is almost entirely positive, contrary to simulations however the position of the valley for the 70 nm particle matches perfectly. The maximum value of transmission difference is 1.04 %. The absorption however is in good agreement now with the simulations, showing a peak at 500 nm with a maximum of 0.42 %, in contrast with the previous sample. It can be seen from the AFM image (fig. 4.4.22a) that the sample contains the lowest amount of clusters in all samples. There are very few clusters measuring around 20 nm and the rest as we can see in the histogram (fig 4.2.22b) are below 10 nm. The counting and height measuring was performed in a square 2x2 µm. The density is as expeced very low measuring only 1.8 particles/μm^2.

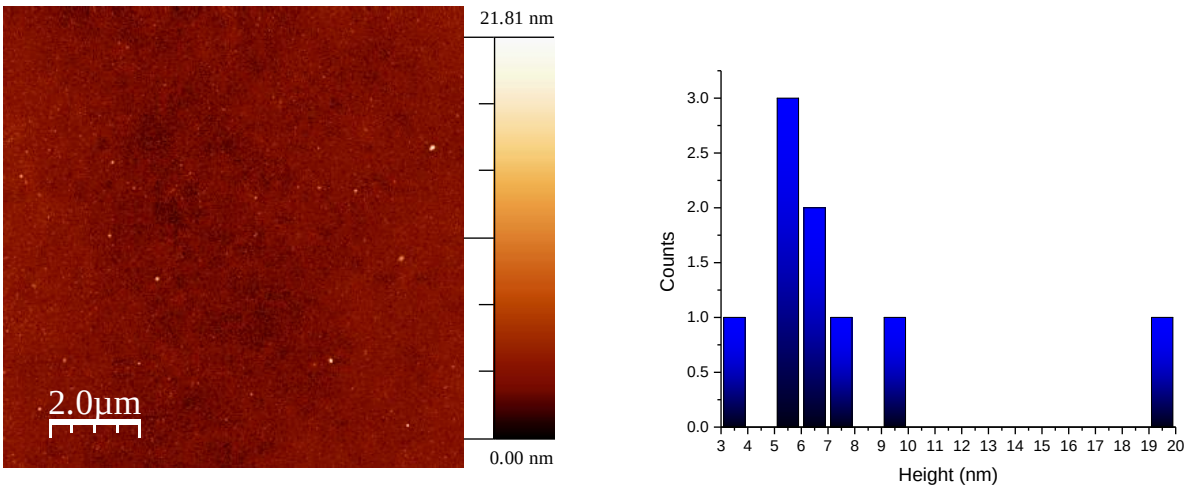

Figure 4.4.22: AFM scan a) and particle height distribution histogram for cs 826. This sample contains the lowest amount of particles in the entire project.

Tables 4.11 and 4.12 show the calculated peaks for total reflection and transmission in comparison with the experimental ones. The agreement is very good for the concition of destructive interference in transmission for both samples. The rest of the calculations deviate from 100 to 200 nm from the experiments.

Sample	λ (nm) Exp	SiN n	λ (nm) m=1
824	465	2.725	370.6
825	431	2.58	350.88

a

Sample	λ (nm) Exp	SiN n	λ (nm) m=1
824	465	2.725	247.0667
825	431	2.75	248.4267

b

Table 4.11: Calculated peaks for reflection using the condition for destructive a) and constructive b) interference formula. Exp denotes the experimental peaks and n is the refractive index of silicon nitride. The peaks were calculated for various integers m, but only the ones that gave the closest result to the experimental are chosen.

Sample	λ (nm) Exp	SiN n	λ (nm) m=1
824	375	2.73	371.28
825	353	2.725	370.6

a

Sample	λ (nm) Exp	SiN n	λ (nm) m=1
824	375	2.73	247.52
825	353	2.725	247.06

b

Table 4.12: Calculated peaks for transmission using the condition for destructive a) and constructive b) interference formula. Exp denotes the experimental peaks and n is the refractive index of silicon nitride. The peaks were calculated for various integers m, but only the ones that gave the closest result to the experimental are chosen.

The cross sections of the electric and magnetic fields are shown in the following pictures. The pictures are selected for the wavlengths were reflection transmission exhibits a valley, as well as for wavelengths far away from the valley. The rest of the wavelengths depict similar results to what we have seen so far. Figure 4.4.23a) shows the electric field cross section taken from the 20 nm particle using a y-normal monitor at 435 nm. The blue stripe is the thin film where the field intensity is very low. The zoom in (Fig. 4.23 b)provides a more clear image of the latteral scattering at the sides of the particle. The mangetic field for the same wavelength is shown in the inset fig. 4.4.23c) zoomed in on the partilce. The intensity is maximized inside the film while inside the particle is significantly lower. Figure 4.4.23d) depicts the cross section of the electric field for the reference at 435 nm.

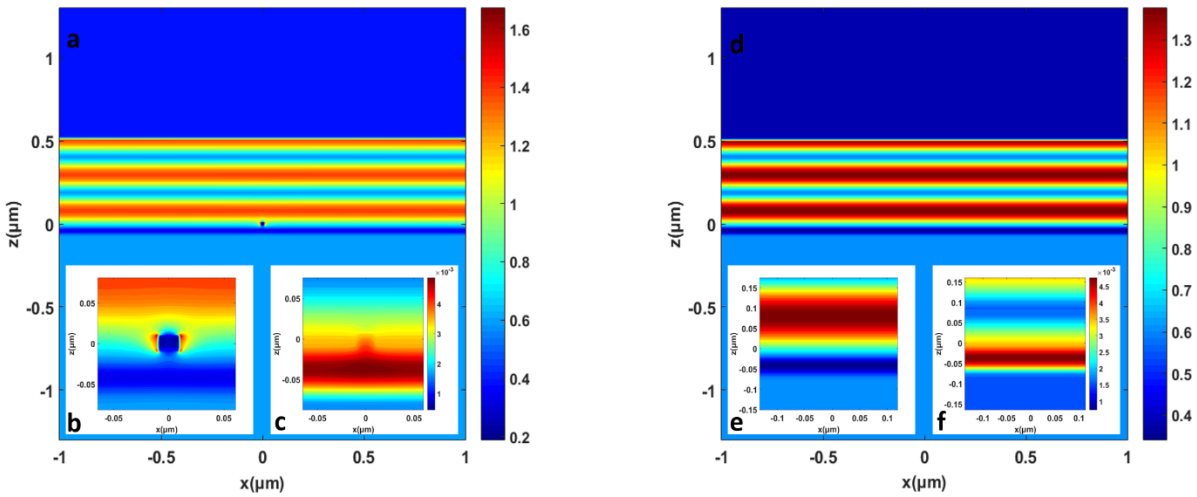

Figure 4.4.23: a) Electric field cross section at 435 nm for the 20 nm particle obtained from the y-axis normal monitor. The intensity of the field is higher above. b) zoom in where the lateral scattering by the particle can be seen. c) Magnetic field from the same monitor zoomed in on the film showing maximum intensity inside the film and the particle. d) Electric field cross section for the reference at 435 nm. This image is to indicate the effect the particle has on the sample with zoom in e). Zoom in on the magnetic field for the same parameters

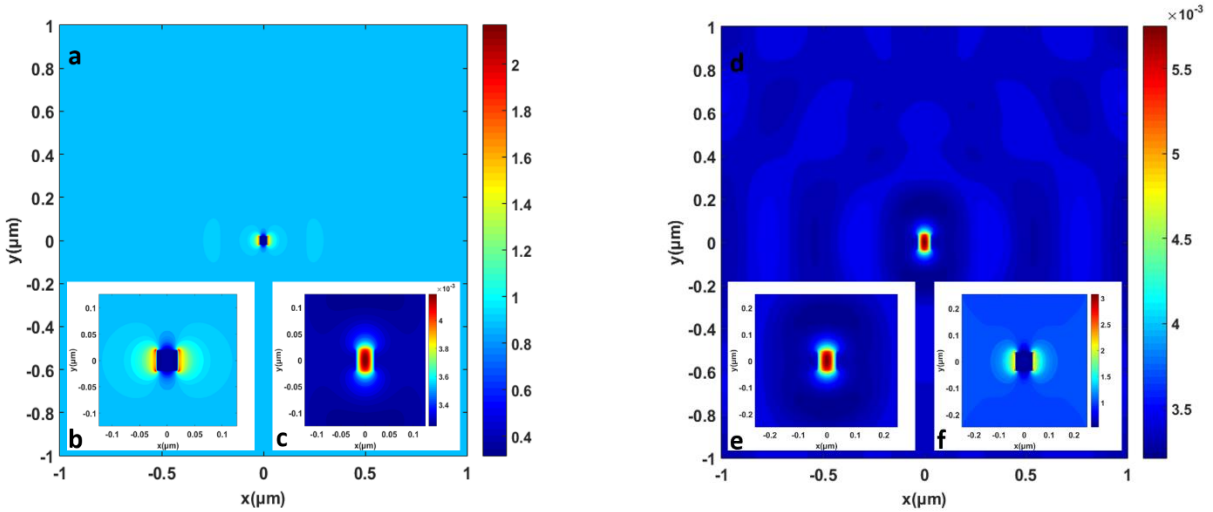

Figure 4.4.24: a) Electric field cross section for the 40 nm particle at 447 nm (on the valley) showing some interesting interference patterns. b) zoom in on the particle to show the lateral scattering. c) Magnetic field cross section for the same wavelength zoomed in showing rhomboidal shape interference patterns and resonance inside the particle. The monitor is normal to the z axis. d) Magnetic field of the 70 nm particle at 547 nm (on the valley). Very intense interference patterns are visible as well as the resonance inside the particle. e) zoom in on the particle showing the resonance. f) electric field cross section from the same monitor showing the high field intensity on the sides of the particle. The monitor is normal to the z axis. The color scale indicates the intensity of the field.

The monitor is again normal to the y axis. The very low fielnd intensity inside the film does not indicate interference. The zoom in (fig. 4.4.23 e) shows that the intensity is higher above thesurface of the film and lower inside. The magnetic field for the same wavelength is shown in the inset fig. 4.4.23 f) where the intensity is maximum inside and slightly lower at the surfaces. In comparison with the picture for the 20 nm particle we see that there is not so much difference between the two which explains the low response of the particle in reflection shown earlier in the difference graph. Figure 4.4.24 a) depicts the electric field at 447 nm (on transmission valley) with a zoom in shown in inset fig 4.4.24 b) where the increased field intensity on the edges of the particle is shown. Figure4.4.24c) shows the magnetic field zoomed in on the particle which exhibits visible resonance. In figure 4.4.24 d) the magnetic field at 517 nm is depicted where the interference patterns are very intense and unusual in shape probably due to the periodicity of the film. The typical resonance inside the particle is clearly visible as can bee seen in the zoom in (fig 4.4.24 e). The corresponding cross section for the electric field shown in the inset fig. 4.4.24 f) zoomed in on the particle where the typical increased intensity on the sides due to lateral scattering is visible.

Two more cross sections for wavelengths that are far away from the ones for which a valley is observed, are shown in fig. 4.4.25. Figure 4.4.25 a) demonstrates the electric field at 637 nm (off valley).

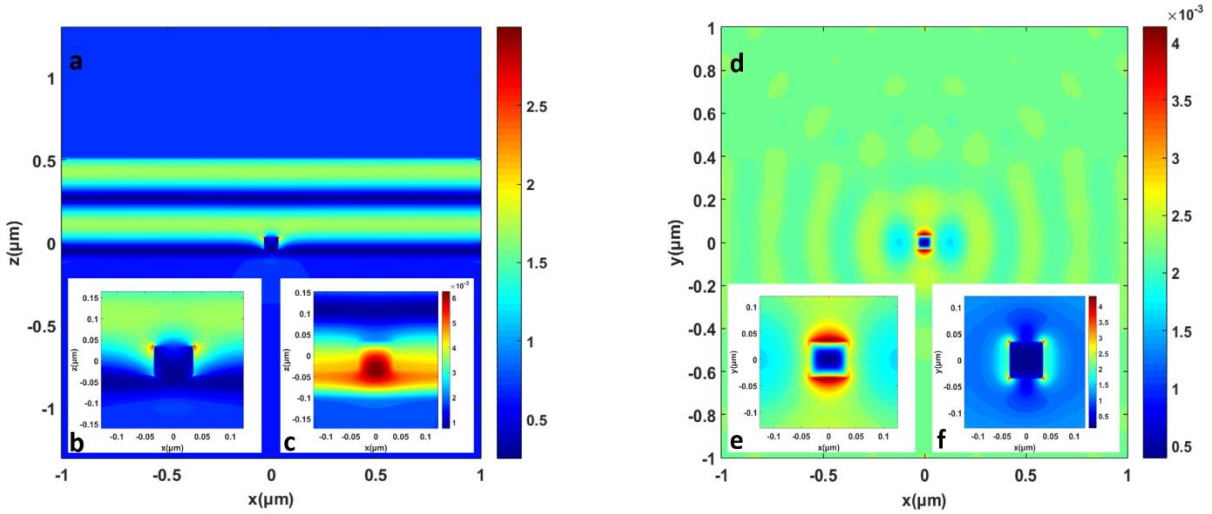

Figure 4.4.25: a) Electric field cross section for the 70 nm particle at 637 nm (off the valley) showing overall low intensity and especially inside the particle and the film. b) zoom in on the particle showing slightly more intense field on the sides and lower corners. c) Magnetic field cross section from the same monitor where the intensity is maximum inside the thin film and lower in the particle. d) Magnetic field cross section for the 70 nm particle at 256 nm (off the valley) showing circular interference patterns. e) Zoom in showing high field intensity on the perimeter of the particle and very low inside it. The monitor is normal to the z axis. f) Electric field cross section for the same wavelength. The field is almost zero inside the particle and it is higher on the sides and on the four corners.

The over all intensity is very low with the minimum being inside the film and the particle and slightly higher on their outer surfaces. The magnetic field for te same wavelength is shown in the inset fig. 4.4.25 c) zoomed in on the particle. The intensity is maximum inside the particle and lower but still high inside the film. In d) and e) (zoom in on the particle) the magnetic field at 256 nm (off valley) for the 70 nm particle as observed from the monitor normal to the z axis is indicating high absorption since the field intensity is nearly zero inside the particle and scattering on the sides of the particle on the positive and negative direction of y axis. The circular patterns are the result of intererence due to the periodic boundary conditions. The electric field at the same wavelength is shown in the inset fig. 4.4.25 f) exhibiting very low overall intensity wich is only increased at the outer corners of the particle.

General observations

For the first sample there is a further increase in the maximum values by an order of magnitude compared to the smaller thicknesses. The FWHM is broader for the reflection and narrower for the transmission

compared to the previous thickness. The reflection and transmission shifted only slightly compared to the 43 nm thickness, about 50 nm for reflection and 20 nm for transmission. Simulated total reflection shows the same results for the three different sizes indicating no size relation. For transmission this is not the case as we see intense size dependence regarding the difference value, and less intense in terms of peak position.

Bibliography

1. Keyworld energy statistics 2014. . 2014.

2. Van lare C. *Light trapping in thin-film solar cells using dielectric and metallic nanostructures.* University Of Amsterdam; 2014.

3. Thampi KR, Byrne O, Surolia PK. Renewable energy technologies and its adaptation in an urban environment. *Optoelectronic Materials and Thin Films (Omtat 2013)*. 2014;1576:3-18. doi: 10.1063/1.4861968.

4. Hosenuzzaman M, Rahim NA, Selvaraj J, Hasanuzzaman M, Malek ABMA, Nahar A. Global prospects, progress, policies, and environmental impact of solar photovoltaic power generation. *Renewable & Sustainable Energy Reviews*. 2015;41:284-297. doi: 10.1016/j.rser.2014.08.046.

5. Wang D, Su G. New strategy to promote conversion efficiency using high-index nanostructures in thin-film solar cells. *Scientific Reports*. 2014;4:7165. doi: 10.1038/srep07165.

6. Rodriguez H, Guerrero I, Koch W, et al. Handbook of photovoltaic science and enginnering. In: Luque A, Hegedus S, eds. Hoboken, NJ : Wiley,; 2003:220.

7. Brongersma ML, Cui Y, Fan S. Light management for photovoltaics using high-index nanostructures. *Nat Mater*. 2014;13(5):451-460. doi: 10.1038/NMAT3921.

8. Krc J, Smole F, Topic M. Potential of light trapping in microcrystalline silicon solar cells with textured substrates. *Prog Photovoltaics*. 2003;11(7):429-436. doi: 10.1002/pip.506.

9. Kluth O, Rech B, Houben L, et al. Texture etched ZnO : Al coated glass substrates for silicon based thin film solar cells. *Thin Solid Films*. 1999;351(1-2):247-253. doi: 10.1016/S0040-6090(99)00085-1.

10. Yu Z, Raman A, Fan S. Nanophotonic light-trapping theory for solar cells. *Appl Phys A-Mater Sci Process*. 2011;105(2):329-339. doi: 10.1007/s00339-011-6617-4.

11. Atwater HA, Polman A. Plasmonics for improved photovoltaic devices. *Nat Mater*. 2010;9(3):205-213. doi: 10.1038/NMAT2629.

12. Schuster CS, Morawiec S, Mendes MJ, et al. Plasmonic and diffractive nanostructures for light trapping-an experimental comparison. *Optica*. 2015;2(3):194-200. doi: 10.1364/OPTICA.2.000194.

13. Wang B, Leu PW. High index of refraction nanosphere coatings for light trapping in crystalline silicon thin film solar cells. *Nano Energy*. 2015;13:226-232. doi: 10.1016/j.nanoen.2014.10.040.

14. Bezares FJ, Long JP, Glembocki OJ, et al. Mie resonance-enhanced light absorption in periodic silicon nanopillar arrays. *Optics Express*. 2013;21(23):27587-27601. doi: 10.1364/OE.21.027587.

15. Spinelli P, Verschuuren MA, Polman A. Broadband omnidirectional antireflection coating based on subwavelength surface mie resonators. *Nat Commun*. 2012;3:692. doi: 10.1038/ncomms1691.

16. van Lare C, Lenzmann F, Verschuuren MA, Polman A. Dielectric scattering patterns for efficient light trapping in thin-film solar cells. *Nano letters*. 2015;15(8):4846-52. doi: 10.1021/nl5045583.

17. Gollu SR, Sharma R, Srinivas G, Kundu S, Gupta D. Incorporation of SiO2 dielectric nanoparticles for performance enhancement in P3HT:PCBM inverted organic solar cells. *Org Electron*. 2015;24:43-50. doi: 10.1016/j.orgel.2015.05.017.

18. Spinelli P, Polman A. Light trapping in thin crystalline si solar cells using surface mie scatterers. *Ieee Journal of Photovoltaics*. 2014;4(2):554-559. doi: 10.1109/JPHOTOV.2013.2292744.

19. Hong L, Rusli, Wang X, et al. Towards perfect anti-reflection and absorption for nanodome-array thin film silicon solar cell. *Pv Asia Pacific Conference 2012*. 2013;33:150-156. doi: 10.1016/j.egypro.2013.05.052.

20. Ferry VE, Verschuuren MA, van Lare MC, Schropp REI, Atwater HA, Polman A. Optimized spatial correlations for broadband light trapping nanopatterns in high efficiency ultrathin film a-si:H solar cells. *Nano Letters*. 2011;11(10):4239-4245. doi: 10.1021/nl202226r.

21. Grzela G, Hourlier D, Rivas JG. Polarization-dependent light extinction in ensembles of polydisperse vertical semiconductor nanowires: A mie scattering effective medium. *Physical Review B*. 2012;86(4):045305. doi: 10.1103/PhysRevB.86.045305.

22. Mann SA, Grote RR, Osgood RM,Jr., Schuller JA. Dielectric particle and void resonators for thin film solar cell textures. *Optics Express*. 2011;19(25):25729-25740. doi: 10.1364/OE.19.025729.

23. Spinelli P, Macco B, Verschuuren MA, Kessels WMM, Polman A. Al2O3/TiO_2 nano-pattern antireflection coating with ultralow surface recombination. *Appl Phys Lett*. 2013;102(23):233902. doi: 10.1063/1.4810970.

24. Yang L, Leung WW. A scattering layer composed of electrosprayed polydispersed-size nanocrystallite TiO_2 for high efficiency dye sensitized solar cells. *Rsc Advances*. 2013;3(48):25707-25710. doi: 10.1039/c3ra40865e.

25. Chen R, Kang C, Lin J, Lin T, Lai C. Optimal design for the diffusion plate with nanoparticles in a diffusive solar cell window by mie scattering simulation. *International Journal of Photoenergy*. 2013:481637. doi: 10.1155/2013/481637.

26. McNeil LE, French RH. Multiple scattering from rutile TiO_2 particles. *Acta Materialia*. 2000;48(18-19):4571-4576. doi: 10.1016/S1359-6454(00)00243-3.

27. Bohren C, Huffman D. Absorption and scattering by a sphere. In: *Absorption and scattering of light by small particles.* Wiley-VCH Verlag GmbH; 1998:82-129. 10.1002/9783527618156.ch4.

28. https://en.wikipedia.org/wiki/Mie_scattering.

29. Serway RA, Jewett JW. Chapter 37.5: Interference in thin films. In: *Physics for scientists and engineers with modern physics.* 9th ed. USA: Finch, M.; Hartford, C.; 2014:1144.

30. Grunwald R. Chapter 3 - thin-film optics. In: Grunwald R, ed. *Thin film micro-optics.* Amsterdam: Elsevier; 2007:39-58. http://dx.doi.org/10.1016/B978-044451746-3/50005-5.

31. Miroshnichenko AE, Flach S, Kivshar YS. Fano resonances in nanoscale structures. *Rev Mod Phys*. 2010;82(3):2257-2298. doi: 10.1103/RevModPhys.82.2257.

32. Fan P, Yu Z, Fan S, Brongersma ML. Optical fano resonance of an individual semiconductor nanostructure. *Nat Mater*. 2014;13(5):471-475. doi: 10.1038/NMAT3927.

33. Tribelsky MI, Flach S, Miroshnichenko AE, Gorbach AV, Kivshar YS. Light scattering by a finite obstacle and fano resonances. *Phys Rev Lett*. 2008;100(4):043903. doi: 10.1103/PhysRevLett.100.043903.

34. van de Groep J, Polman A. Designing dielectric resonators on substrates: Combining magnetic and electric resonances. *Optics Express*. 2013;21(22):26285.

35. http://phys.org/news/2013-05-lorentz-fano-spectral-line.html.

36. Fu Q, Sun W. Mie theory for light scattering by a spherical particle in an absorbing medium. *Appl Opt*. 2001;40(9):1354-1361. doi: 10.1364/AO.40.001354.

37. http://www.will-cavanagh.com/?portfolio=physically-based-thin-film-interference.

38. http://hyperphysics.phy-astr.gsu.edu/hbase/atmos/blusky.html.